BICONTINUOUS CUBIC LYOTROPIC LIQUID CRYSTAL MONOMERS: PLATFORM MODIFICATIONS AND DESIGN OF NEW FUNCTIONAL MOTIFS

by

Patrick Li

B.S., The University of North Carolina at Chapel Hill, Chapel Hill, NC, 2017

A thesis submitted to the
Faculty of the Graduate School of the
University of Colorado in partial fulfillment
of the requirement for the degree of
Doctor of Philosophy
Department of Chemistry
2022

Committee Members:

Douglas Gin

Wei Zhang

Oana Luca

Jihye Park

Chinedum Osuji

Abstract

Li, Patrick
(Ph.D., Chemistry; Department of Chemistry)

Bicontinuous Cubic Lyotropic Liquid Crystal Monomers: Platform Modifications and Design of New Functional Motifs

Thesis directed by Prof. Douglas L. Gin

The bicontinuous cubic (Q) lyotropic liquid crystal (LLC) phase is highly desired for molecular separation and uptake applications due to its periodic, uniform-size, 3D-interconnected nanopores. In this thesis, the perturbation, formation, and application of the Q phase and Q-phase-forming LLC monomers was explored.

At start of this thesis work, only five intrinsically cross-linkable monomer platforms were known in the literature. The first study in this thesis describes the effect of structural modification on the Q-phase window of one of these already established Q-phase monomers that was previously designed by our group. Seven homologs of this monomer were synthesized, and four of these seven homologs were found to form stable, cross-linked Q-phase networks. However, only one homolog exhibited an improved Q-phase window compared to parent monomer.

Due to the limited success of this homolog study, we were encouraged to design the sixth intrinsically cross-linkable Q-phase-forming LLC monomer. This monomer is based on a simple and novel amphiphile structural motif that does not require difficult synthetic strategies compared to previous intrinsically cross-linkable Q-phase platforms. Cross-linked Q-phase networks of this novel monomer exhibited excellent temperature and solvent stability.

Finally, the first example of a Q-phase network with functional properties beyond molecular size/charge discrimination is described. This functionalized Q-phase polymer network

was formed using a spiropyran-containing dopant monomer that that was designed to blend and cross-link with an established Q-phase-forming LLC monomer, yielding a Q-phase polymer material that retains its phase architecture and reversibly responds to changes in external aqueous solution and vapor pH. Preliminary studies also suggested that this spiropyran-containing Q-phase network material can act as a potential colorimetric sorbent or gated-response material for irreversibly binding aq. Pb^{2+} ions when triggered with UV light.

Acknowledgments

I am grateful for the expert guidance of my advisor, Professor Doug Gin. Doug was willing to take the risk of taking on a first-year graduate student who had zero chemistry research experience and personally taught me many synthetic and troubleshooting techniques. Doug's mentorship and guidance have truly molded me into the scientist that I am today.

I would also like to thank all the graduate students and postdocs past and present who were always happy to help me at a moment's notice. Dr. Greg Dwulet, Dr. Zhangxing Shi, Dr. Sarah Dischinger, Dr. Mike McGrath, Dr. Chamaal Karunaweera, and John Malecha helped me get started in the Gin and Noble labs. To Will Yi, Brianna Callahan, and Dr. Garrett Cairo of the Sammakia lab, the three of you have been incredible resources of synthetic knowledge. To Dr. Omar Q. Imran and Christopher Johnson of the Osuji Lab, I am not exaggerating when I say that most of my thesis would not exist if I didn't have the chance to collaborate with you two. To Lauren Bodkin and Keira Culley, keep fighting the good fight, I don't think I've ever had a dull conversation with you two.

I would like to acknowledge some of the undergraduate students I mentored: Marisabel Reinhardt, Kara Moore, and Sam Dyer. you three were critical for my success and I hope that I was at least half as helpful to you as you were to me.

I have had the fortune to interact with many of the faculty and staff during my time at CU. Kayla Jones and Matt Bohn always had their door open (and candy to eat) and I spent a lot of my downtime just chatting with you two. I would like to thank Professor Rich Noble for providing helpful input and knowledge towards the engineering aspects of my projects. To Professor Oana Luca, I still remember our first interaction in which I mistook you for a prospective graduate student during my visit weekend. You've been a helpful resource with networking and to graduate

students in general. Finally, to Professor Chinedum Osuji, I am incredibly grateful that you were willing to collaborate with me these past few years. For Chapters 4 and 5, you and Doug were essentially joint advisors for me, and a good portion of my success is thanks to you.

Finally, I would like to thank my friends and family. My parents for teaching me how to succeed and always encouraged me to push myself and strive to try my hardest. They always indulged me in a variety of hobbies even if they thought my hobbies were too dangerous. My sister, Jinwen, for always listening to me complain about graduate school and for providing me with photos of my nephew. To Dr. Josh Kamps, I am grateful for the time we spent snowboarding and playing video games. To Haleigh, thanks for all the laughs, conversation, and climbing adventures. To the Terr Family, thank you for providing me with a second home. You have always welcomed me with open arms and provided me with food and advice. Finally, to my partner Marlo, your support, companionship, and passion for climbing, has had the greatest impact on me during my time in graduate school.

Table of Contents

List of Tables

Chapter 1

Chapter 3

Chapter 4

List of Figures

Chapter 1

Chapter 3

Chapter 4

Chapter 5

Chapter 1: Overview of Bicontinuous Cubic Polymerizable Lyotropic Liquid Crystal Systems

1.1 Introduction to Lyotropic Liquid Crystals

Lyotropic liquid crystal (LLC) mesogens are amphiphilic molecules comprised of hydrophilic and hydrophobic domains. In the presence of different solvents, selective solvation of a LLC mesogen's hydrophilic or hydrophobic domains drives spontaneous phase-separation and self-assembly to form ordered but fluid molecular arrays with monodisperse, nanometer-scale domains (i.e., LLC phases).[1] These phase-separated, periodic domains can exhibit a variety of dimensionalities and shapes, depending on the type of LLC phase formed and on whether the phase curves around the solvent-rich hydrophobic domains (i.e., normal/Type I phases) or the solvent-poor hydrophilic domains (i.e., inverted/Type II phases).[1] LLC phases are classified by their dimensionality and symmetry: hexagonal close-packed cylindrical normal or inverted micelles form the 1D hexagonal (H) phases, stacks of planar sheets form the 2D lamellar (L) phase, and 3D-interpenetrating hydrophilic and hydrophobic domains separated by a cubic bicontinuous layer form the bicontinuous cubic (Q) phases.[1,2] Subscripts are often added after the main LLC phase label to indicate whether the specific lyotropic phase is Type I or Type II (i.e., H_I or H_{II} phase). The diversity of LLC phases combined with their ability for molecular self-assembly provides attractive opportunities for control over nanostructure, processability, as well as incorporation of a wide range of chemical functionalities.[2]

The formation of a particular LLC phase is usually composition-, temperature-, and pressure-dependent,[1] but LLC phase formation can also be controlled by altering the molecular shape or chemistry of the amphiphilic mesogen or through additives that can promote the formation of a particular nanostructure.[2,3] An ideal, symmetric phase diagram of various LLC

phases and different LLC phases typically observed in amphiphile-water mixtures is shown in Figure 1.1 below.[4] It should be noted that not all phase diagrams are symmetric in nature and not all amphiphile-water mixtures demonstrate all of the phases depicted in Figure 1.1. Furthermore, water as a solvent is not necessary to induce LLC phase formation, although it is the most common polar solvent used. Other polar solvents such as glycerol, propylene carbonate, and dimethyl formamide, have also been used to induce LLC phase formation.[5,6]

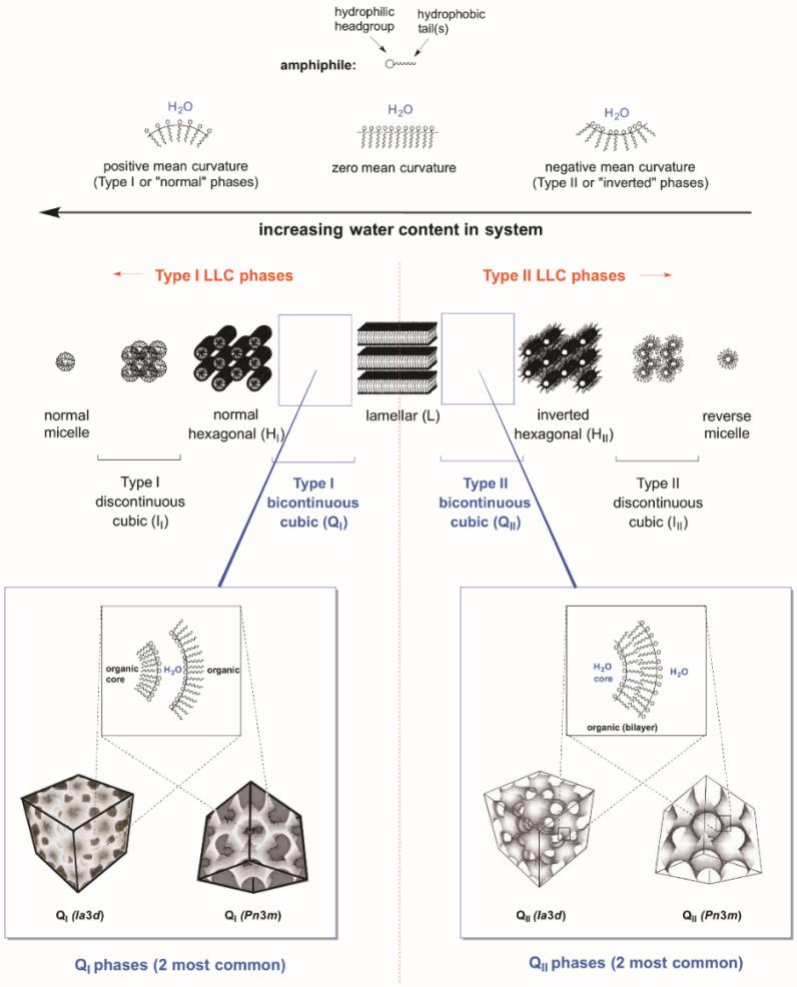

Figure 1.1 Schematic representation of common LLC phases formed by amphiphiles in water in an ideal phase progression, with an emphasis on the Q phases. Partially reproduced from Ref. 4. Copyright Nature Publishing Group, 2012.

LLC phases have many characteristics that make them ideal for advanced materials applications. First, although LLC phase formation is dependent on numerous variables as described above, those variables are often easily controlled. Second, the fluid nature of LLC phases allows for increased material processability. Third, the periodic and nanoporous architectures of LLC phases can allow for selective interactions in the hydrophilic and hydrophobic domains.[7] Significant research has been conducted towards applying the fluid nature of the LLC phase for small-molecule encapsulation for drug delivery applications.[7] Another popular application of LLC phases is nanostructure templating. Templating is the process in which the nanoporous domains of an LLC phase is saturated with polymerizable guest molecules, which are then polymerized within the LLC phase.[8] The LLC template can then be removed leaving behind a nanostructured polymer.[8] Templating LLC phases alleviates the need for niche surfactants and is tolerant to a wide variety of monomers.[2] However, because the reactive species are separate from the LLC phase, phase-separation is more likely and thus phase retention is not guaranteed.[2]

Recently, the use of LLC nanostructures for materials applications outside of templating has gained increased traction. LLC phase domains can function as nanopores allowing for potential applications including but not limited to nanofiltration, ion transport, and vapor transport.[7-11] Through synthetic design, the porous domains of LLC phases can also be given higher-order functional properties by chemically modifying the LLC mesogen with active groups (e.g., appending a stimuli-responsive functional group). However, since LLC phase formation and the resultant nanostructures are sensitive to environmental conditions and mesogen architecture, the nanostructure has to be stabilized or otherwise the desired LLC phase will be lost.

The fragile nature of LLC phases can be addressed by designing reactive amphiphiles (i.e., LLC monomers) and utilizing photo-initiated free-radical polymerization to rapidly preserve the

LLC phase as a polymer network. The "bottom-up" strategy of designing reactive amphiphiles, targeting a particular LLC phase, and polymerizing the LLC phase in situ, is sometimes referred as "synergistic templating.[2]" LLC phase retention through synergistic strategies has been achieved through the direct polymerization of mono-functional LLC phase-forming monomers or blending monofunctional monomers with a cross-linker or other reactive additives.[12-16] Synergistic LLC phase retention has also been achieved through the use of intrinsically cross-linkable LLC phase-forming monomers.[2] Substituting monofunctional amphiphiles for intrinsically cross-linkable amphiphiles can eliminate the need for additives while still yielding a cross-linked polymer network with nanostructured phase retention and improved mechanical and chemical robustness. Regardless of the method used to preserve the LLC phase nanostructure, LLC-based polymer materials have yielded advances including but not limited to: membrane applications, templated syntheses, heterogenous catalysis, molecular-size filtration, and enhanced ion transport.[9]

1.2 The Bicontinuous Cubic (Q) LLC Phase

Although numerous LLC phases are known, Q phases in particular are highly sought for molecular separation and uptake applications.[4] This is because Q phases possess overall cubic symmetry and 3D-interconnected nanopore systems, which do not require pore alignment for good transport or access, as with lower-dimensionality LLC phases.[4] Q phases are more sensitive than lower-dimensional LLC phases and require specific amphiphile structural motifs and precise amphiphile/solvent compositions in order to achieve a metastable phase.[2] Q phases are typically confirmed through the use of a combination of polarized light microscopy (PLM), and small-angle X-ray scattering (SAXS) or powder X-ray diffraction (PXRD).[1,2] Under PLM, Q phases are characterized by their black (pseudo-isotropic) optical texture (a consequence of their cubic

symmetry). Through X-ray analysis, Q phases are differentiated into three main space groups ratios, namely the primitive (*Im3m*), the double-diamond (*Pn3m*), and the gyroid lattice (*Ia3d*).[2]

Table 1.1 Characteristics of the 3 major Q LLC phase space groups

Space Group	X-ray Bragg Peak Ratios	PLM Texture
Im3m	√2: √4: √6: √8: √10…	Not birefringent
Pn3m	√2: √3: √4: √6: √8: √9…	
Ia3d	√6: √8: √14: √16: √18: √20…	

1.3 LLC Bicontinuous Cubic Based Polymers: Existing Platforms and Motifs

Despite the clear advantages of Q-phase LLC polymer networks for applications, only a limited number of Q-phase LLC monomer platforms have been reported that can be polymerized with phase retention through synergistic strategies. The design of monomers that can form Q phases has not been straightforward. Q phases are regarded as intermediate structures between L and H phases in terms of curvature and interfacial energy,[1,17] and amphiphile shape-based packing approaches do not reliably explain Q systems.[3] Although a reactive amphiphile may demonstrate the Q phase pre-polymerization, a slight change in phase structure or complete loss of the desired phase may occur post-polymerization.[2] This is a result of the significant increase in monomer molecular weight during polymerization which leads to increased thermodynamic penalties.[2] The formation of a cross-linked polymer network also tends to increase the overall density of the LLC system (i.e., free-volume decreases due to formation of new bonds during photopolymerization).[2]

LLC monomer shape motifs known to form Q phases have ranged from symmetric gemini amphiphiles,[18-21] wedge-shaped amphiphiles,[5] traditional lipid-like amphiphiles,[22] and modified

lipid-like amphiphiles (Figure 1.2).[16] Although the majority of Q phase-retaining LLC monomer systems were intrinsically cross-linkable single-monomer systems,[5,6,12,18,20,21] there are also examples of polymerized Q phases formed from cross-linkable mixtures of LLC monomers[22,23] or blends with cross-linking co-monomers or other organic additives.[12-16] These monomer systems also had a wide breadth of chemical variety when it came to the hydrophilic regions of the reactive amphiphiles as well. The hydrophilic regions ranged from uncharged,[27] ionic,[5,6,12,18,20] and zwitterionic.[13,14,21,22] The only consistent trend between these diverse monomer motifs was that their hydrophobic region contained a polymerizable group.

Structurally simpler single-head/single-tail LLC monomers have also been reported to form Q phases.[24-28] These monomer platforms featured easier syntheses and uncharged,[25] ionic,[24] and zwitterionic[28] simple surfactant platforms have been reported. However, these simple surfactant platforms were monofunctional amphiphiles (i.e., containing a single chain-addition polymerizable group per molecule), which means that in order to produce a robust cross-linked Q phase polymer network, co-monomers or other organic cross-linking additives were required to preserve the Q phase.[24,25,28]

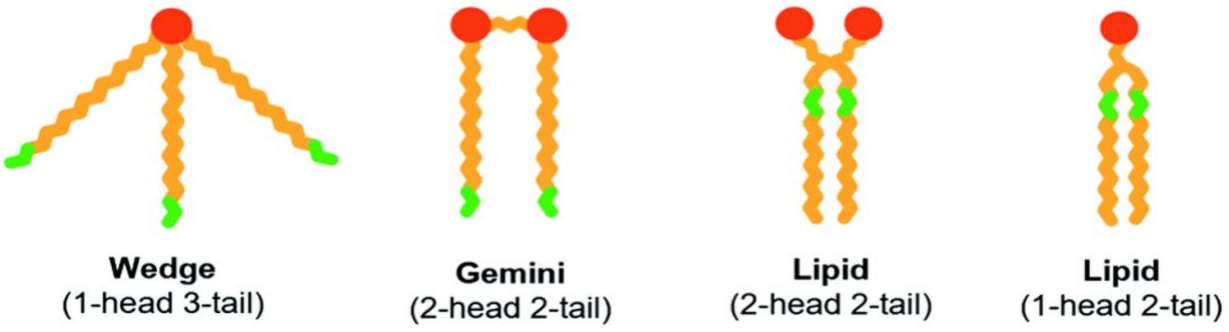

Figure 1.2 Schematic of the intrinsically cross-linkable LLC monomer motifs reported to form Q LLC phases prior to the work in this thesis (red/orange = hydrophilic headgroup, yellow = hydrophobic tail, green = polymerizable group). Partially reproduced from Ref. 29. Copyright The Royal Society of Chemistry, 2021.

It is important to note that all of the Q-phase polymer networks described up until now were formed using synergistic strategies (i.e., the reactive amphiphiles were capable of forming the Q phase and the Q phase was retained after polymerization). There are a handful of other LLC systems that can form Q-phase polymer networks through templating strategies. However, as previously mentioned, Q phase retention is not as reliable. Thus, the remainder of this thesis will focus on the study and design of intrinsically cross-linkable Q-phase-forming monomers.

1.4 Synopsis of Existing Intrinsically Cross-linkable Q-phase LLC Systems

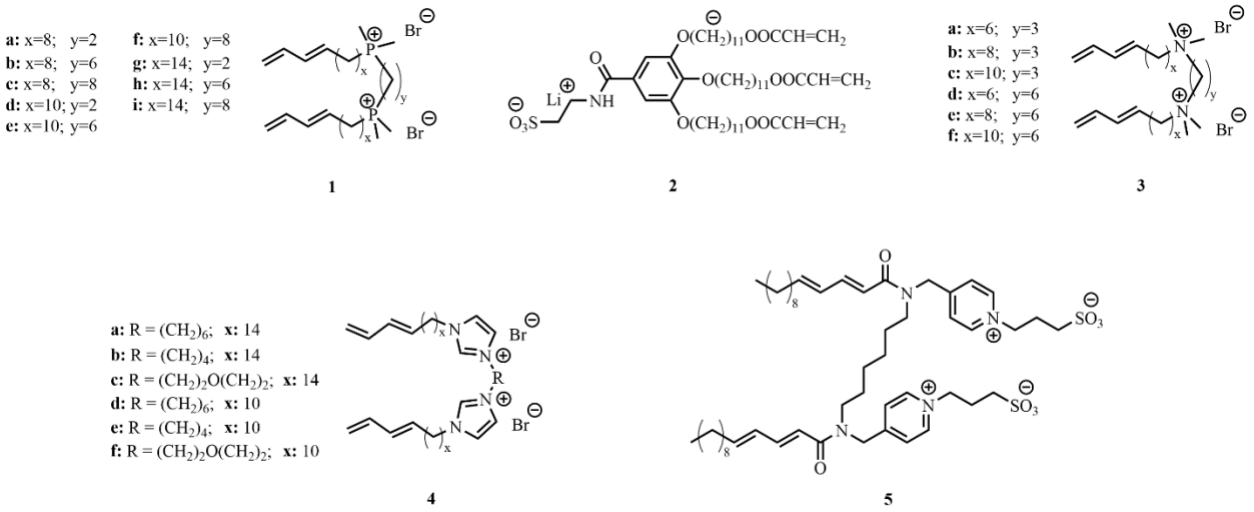

Scheme 1.1 Chemical structures of the five known intrinsically cross-linkable Q-phase-forming LLC monomer platforms prior to the work in this thesis. The publication year and reference for each system are as follows: **1**, 2003, Ref. 18; **2**, 2009, Ref. 5; **3**, 2010, Ref. 20; **4**, 2012, Ref. 6; **5**, 2019, Ref. 21.

The development of intrinsically cross-linkable Q-phase LLC monomers/platforms has been an arduous endeavor. The first example of an intrinsically cross-linkable Q-phase-forming LLC monomer (**1**) that could be polymerized with phase retention was developed in the Gin research lab in 2003.[18] Monomer platform **1** followed a gemini structural motif with an ionic

bis(phosphonium) headgroup and two aliphatic, polymerizable 1,3-diene tails.[18] Four different homologs of **1** (i.e., **1d**, **1e**, **1f**, and **1i**) formed the Q_I phase and upon polymerization, each yielded a brittle polymer film with excellent thermal stability.[18] Further studies of the bis(phosphonium) system focused on **1e** due to the fact that the Q_I phase formed at room temperature despite its narrow Q_I phase window (82–88 wt% amphiphile).[18] A LLC mixture of **1e**, butyl rubber, and water was able to be hot-pressed onto a porous support and polymerized with Q_I phase retention.[12] The resulting membrane exhibited excellent water vapor transport and good selectivity for water vapor over chloroethyl ethyl sulfide (CEES, a chemical warfare simulant).[12] A LLC mixture of **1e** and water was also to be hot-pressed onto a porous support and the pore size was determined to be ca. 0.75 nm. Furthermore, membranes of **1e** demonstrated efficient water desalination and nanofiltration capabilities comparable to commercial membranes.[19] Despite the novel Q-phase LLC monomer structure and its promising applications, the bis(phosphonium) monomer platform was difficult and costly to synthesize, and the methods utilized to create supported membranes were unsustainable and had limited mesophase processability.[12,18,19]

In an attempt to address the limitations of platform **1**, the Gin and Noble research groups developed a novel bis(ammonium) cross-linkable gemini LLC platform that also formed the Q_I-phase.[20] Homologs **3c** and **3f** formed the Q_I phase with 82.5–87.5 wt% and 85.0–87.5 wt% amphiphile respectively at temperatures >50 °C.[20] When **3c** was processed as a supported membrane, dead-end water nanofiltration studies revealed comparable ion rejection as **1e** with an increased nanopore size of 0.86 nm.[20] The bis(ammonium) platform was easier to synthesize than the bis(phosphonium) platform, however, the cost of synthesis was still high. Additionally, due to **3c**'s narrow phase window with respect to **1e** and near-identical membrane fabrication protocol, the LLC mesophase processability was further reduced.[20]

In 2012, the Gin and Noble research groups developed the bis(imidazolium) cross-linkable Q_I-forming LLC monomer system.[6] This monomer featured a costly but simple synthesis. The Q_I mesophase of **4a**/glycerol was solution-cast onto a porous support and yielded a thin-film composite (TFC) membrane with a ca. 0.96 nm pore size that exhibited high salt rejection and good water permeability.[6] Further work with **4a** revealed that the monomer could be roll-cast for simpler TFC fabrication[30] and TFC membranes of **4a** revealed good breathability with excellent rejection of chemical warfare simulants such as CEES and dimethylmethylphosphonate.[31] Monomer **4a** has become the flagship of the Gin research group over the last ten years, revealing itself to be a robust membrane material with a variety of applications for liquid or vapor phase separations. However, although **4a** does not require difficult membrane fabrication techniques, it still requires elevated temperatures to form the Q_I phase and has a relatively narrow Q_I phase window of ca. 80–85 wt% amphiphile at 65 °C.[6]

In a departure from the gemini LLC monomer motif, the Gin research group developed **2** – a wedge-shaped ionic amphiphile with three polymerizable hydrophobic acrylate tails.[5] Monomer **2** was the second known example of an intrinsically cross-linkable Q-phase-forming monomer and formed the Q_{II} phase at room temperature (partial phase diagram analysis suggested that the Q_{II} phase window ranged from ca. 5–25 wt% amphiphile in propylene carbonate).[5] Although **2** found a potential application as a new type of Li^+ ion conductor with an organic electrolyte, limited characterization was done with respect to its phase diagram and pore size.[5] Furthermore, **2**'s ability for membrane applications was never fully pursued.

Outside of the Gin group, the Ichikawa research group has found recent success with the design of an intrinsically cross-linkable gemini amphiphile (**5**) that features a novel zwitterionic headgroup coupled with two polymerizable hydrophobic tails.[13,14,21] Detailed LLC phase

characterization and pore size elucidation of **5** is yet to be performed. Instead, the Ichikawa research group focused on the development of robust polymer films of **5** for applications in proton conduction.[13,14,21] In this regard, they have demonstrated that **5** can be blended with LLC co-monomers or other organic additives to tune the resulting polymer's material properties while retaining the original phase nanostructure.[13,14]

1.5 Future Directions for Q-phase LLC Monomer Systems

Recent interest in the lyotropic Q phase has been in the development of simpler, cross-linkable Q-phase LLC monomer motifs. The use of intrinsically cross-linkable Q-phase LLC monomers reduces the need for use of template monomers, thus increasing the chances of Q-phase retention post-polymerization. Prior to the work discussed in this thesis, there were only five published examples of intrinsically cross-linkable LLC monomer systems that retain the Q phase after polymerization (Scheme 1.1). These systems have been studied extensively and have found applications including but not limited to: vapor transport,[12] ion transport,[5,21] and liquid nanofiltration.[6] Despite making impressive headway in membrane applications, the five Q-phase monomer motifs shown in Scheme 1.1 all suffer from a combination of moderate-to-difficult synthesis, high synthetic cost, narrow Q-phase windows, and limited processability prior to cross-linking. These barriers must be overcome if cross-linked Q-phase polymer materials are to become scalable and industrially relevant. Finally, the cross-linked films formed by these five monomer motifs have only been found to be capable of simple transport or molecular size discrimination. A Q-phase monomer and resulting polymer system with advanced functional properties has yet to be demonstrated.

1.6 References

1. For general reviews on LLC phases, see: (a) Tate, M. W.; Eikenberry, E. F.; Turner, D. C.; Shyamsunder, E.; Gruner, S. M. Nonbilayer phases of membrane lipids. *Chem. Phys. Lipids*, **1991**, *57*, 147–164. (b) Seddon, J. M. Structure of the inverted hexagonal (H_{II}) phase, and non-lamellar phase transitions of lipids. *Biochim. Biophys. Acta*, **1990**, *1031*, 1–69. (c) Tiddy, G. J. T. Surfactant-water liquid crystal phases. *Phys. Rep.* **1980**, *57*, 1–46.
2. For a thorough review of LLC materials as templates for advanced applications, see: Saadat, Y.; Imran, O. Q.; Osuji, C. O.; Foudazi, R. Lyotropic liquid crystals as templates for advanced materials. *J. Mater. Chem. A* **2021**, *9*, 21607–21658.
3. Israelachivili, J. N. Intermolecular and Surface Forces with Applications to Colloidal and Biological Systems. Academic: London; **1985**, 249.
4. Wiesenauer, B. R.; Gin, D. L. Nanoporous Polymer Materials Based on Self-Organized, Bicontinuous Cubic Lyotropic Liquid Crystal Assemblies and Their Applications. *Polym. J.* **2012**, *44*, 461–468.
5. Kerr, R. L.; Miller, S. A.; Shoemaker, R. K.; Elliott, B. J.; Gin, D. L. New Type of Li Ion Conductor with 3D Interconnected Nanochannels via Polymerization of a Liquid Organic Electrolyte-Filled Lyotropic Liquid-Crystal Assembly. *J. Am. Chem. Soc*. **2009**, *131*, 15972–15973.
6. Carter, B. M.; Wiesenauer, B. R.; Hatakeyama, E. S.; Barton, J. L.; Noble, R. D.; Gin, D.L. Glycerol-based Bicontinuous Cubic Lyotropic Liquid Crystal Monomer System for the Fabrication of Thin-film Membranes with Uniform Nanopores. *Chem. Mater*. **2012**, *24*, 4005–4007.

7. Gin, D. L.; Pecinovsky, C. S.; Bara, J. E.; Kerr, R. L. Functional Lyotropic Liquid Crystal Materials. *Struct. Bonding* **2007**, *128*, 181–222.
8. Gin, D. L.; Gu, W.; Pindzola, B. A.; Zhou, W. J. Polymerized Lyotropic Liquid Crystal Assemblies for Materials Applications. *Acc. Chem. Res*. **2001**, *34*, 973–980.
9. Gin, D. L.; Lu, X.; Nemade, P. R.; Pecinovsky, C. S.; Xu, Y.; Zhou, M. Recent Advances in the Design of Polymerizable Lyotropic Liquid-Crystal Assemblies for Heterogeneous Catalysis and Selective Separations. *Adv. Funct. Mater*. **2006**, *16*, 865–878.
10. Mueller, A.; O'Brien, D. F. Supramolecular Materials via Polymerization of Mesophases of Hydrated Amphiphiles. *Chem. Rev*. **2002**, *102*, 727–758.
11. Kato, T.; Yoshio, M.; Ichikawa, T.; Soberats, B.; Ohno, H.; Funahashi, M. Transport of ions and electrons in nanostructured liquid crystals. *Nat. Rev. Mater.* **2017**, *2*, 1–20.
12. Lu, X.; Nguyen, V.; Zhou, M.; Zeng, X.; Jin, J.; Elliott, B. J.; Gin, D. L. Cross-linked Bicontinuous Cubic Lyotropic Liquid Crystal-Butyl Rubber Composites: Highly Selective, Breathable Barrier Materials for Chemical Agent Protection. *Adv. Mater*. **2006**, *18*, 3294–3298.
13. Maekawa, A.; Kobayashi, T.; Ichikawa, T. Gyroid nanostructured soft membranes formed by controlling the degree of crosslinking polymerization of bicontinuous cubic liquid-crystalline monomers. *Polym. J.* **2021**, *53*, 463–470.
14. Kobayashi, T.; Li, Y.-X.; Hirota, Y.; Maekawa, A.; Nishiyama, N.; Zeng, X.-B.; Ichikawa, T. Gyroid-Nanostructured All-Solid Polymer Films Combining High H^+ Conductivity with Low H_2 Permeability. *Macromol. Rapid. Commun.* **2021**, 2100115.

15. Jennings, J.; Green, B.; Mann, T. J.; Guymon, C. A.; Mahanthappa, M. K. Nanoporous Polymer Networks Templated by Gemini Surfactant Lyotropic Liquid Crystals. *Chem. Mater.* **2018**, *30*, 185–196.
16. Takeuchi, H.; Ichikawa, T.; Yoshio, M.; Kato, T.; Ohno, H. Induction of bicontinuous cubic liquid-crystalline assemblies for polymerizable amphiphiles via tailor-made design of ionic liquids. *Chem. Commun.* **2016**, *52*, 13861–13864.
17. Fontell, K. Cubic phases in surfactant and surfactant-like lipid systems. *Colloid Polym. Sci.* **1990**, *268*, 264–285.
18. Pindzola, B. A.; Jin, J.; Gin, D. L. Cross-Linked Normal Hexagonal and Bicontinuous Cubic Assemblies via Polymerizable Gemini Amphiphiles. *J. Am. Chem. Soc.* **2003**, *125*, 2940–2949.
19. Zhou, M.; Nemade, P. R.; Lu, X.; Zeng, X.; Hatakeyama, E. S.; Noble, R. D.; Gin, D. L. New Type of Membrane Material for Water Desalination Based on a Cross-linked Bicontinuous Cubic Lyotropic Liquid Crystal Assembly. *J. Am. Chem. Soc.* **2007**, *129*, 9574–9575.
20. Hatakeyama, E. S.; Wiesenauer, B. R.; Gabriel, C. J.; Noble, R. D.; Gin, D. L. Nanoporous, bicontinuous Cubic Lyotropic Liquid Crystal Networks via Polymerizable Gemini Ammonium Surfactants. *Chem. Mater.* **2010**, *22*, 4525–4527.
21. Kobayashi, T.; Li, Y.-X.; Ono, A.; Zeng, X.-B.; Ichikawa, T. Gyroid structured aqua-sheets with sub-nanometer thickness enabling 3D fast proton relay conduction. *Chem. Sci.* **2019**, *10*, 6245–6253.
22. Lee, Y. S.; Yang, J. Z.; Sisson, T. M.; Frankel, D. A.; Gleeson, J. T.; Aksay, E.; Keller, S. L.; Gruner, S. M.; O'Brien, D. F. Polymerization of nonlamellar lipid assemblies. *J. Am. Chem. Soc.* **1995**, *117*, 5573–5578.

23. Srisiri, W.; Benedicto, A.; O'Brien, D. F. Stabilization of a bicontinuous cubic phase from polymerizable monoacylglycerol and diacylglycerol. *Langmuir* **1998**, *14*, 1921–1926.

24. McGrath, K. M.; Drummond, C. J. Polymerisation of liquid crystalline phases in binary surfactant/water systems. Part 1. Allyldodecyldimethylammonium bromide and allyldidodecylmethylammonium bromide. *Colloid Polym. Sci.* **1996**, 274, 316–333.

25. Yang, D.; O'Brien, D. F.; Marder, S. R. Polymerized bicontinuous cubic nanoparticles (cubosome) from a reactive monoacylglycerol. *J. Am. Chem. Soc.* **2002**, *124*, 13388–13389.

26. Gao, X.; Lu, F.; Liu, Y.; Sun, N.; Zheng, L. The facile construction of an anion exchange membrane with 3D interconnected ionic nano-channels. *Chem. Commun.* **2017**, *53*, 767–770.

27. Feng, X.; Imran. Q.; Zhang, Y.; Sixdenier, L.; Lu, X.; Kaufman, G.; Gabinet, U.; Kawabata, K.; Elimelech, M.; Osuji, C. O. Precise nanofiltration in a fouling-resistant self-assembled membrane with water-continuous transport pathways. *Sci. Adv.* **2019**, *5*, eaav9308.

28. Wu, H.; Xu, F.; Gao, G.; Feng, X. Highly Ordered Interconnected 1 nm Pores in Polymers Fabricated from Easily Accessible Gyroid Liquid Crystals. *Macromolecules* **2021**, *54*, 5856–5865.

29. Imran, O. Q.; Li, P.; Kim, N. K.; Gin, D. L.; Osuji, C. O. Stable cross-linked lyotropic gyroid mesophases from single-head/single-tail cross-linkable monomers. *Chem. Commun.* **2021**, *57*, 10931–10934.

30. Dischinger, S. M.; McGrath, M. J.; Bourland, K. R.; Noble, R. D.; Gin, D. L. Effect of Post-Polymerization Anion-Exchange on the Rejection of Uncharged Aqueous Solutes in Nanoporous, Ionic, Lyotropic Liquid Crystal Polymer Membranes. *J. Membr. Sci.* **2017**, *529*, 72–79.

31. Dwulet, G. E.; Dischinger, S. M.; McGrath, M. J.; Basalla, A. J.; Malecha, J. J.; Noble, R. D.; Gin, D. L. Breathable, Polydopamine-Coated Nanoporous Membranes That Selectively Reject Nerve and Blister Agent Simulant Vapors. *Ind. Eng. Chem. Res.* **2019**, *58*, 21890–21893.

Chapter 2: Overview of Ph.D. Thesis Research

2.1 Objectives

The Gin and Noble research groups were pioneers in the development of intrinsically cross-linkable, bicontinuous cubic (Q)-phase-forming lyotropic liquid crystal (LLC) monomers motifs. They were successful in developing four out of the five existing motifs reported in the literature (see Scheme 1.1 in Chapter 1) and with each new monomer generation, were able to improve to a degree the cost/ease of synthesis, processability, or Q phase window of the amphiphilic monomer system. Since the development of the gemini bis(imidazolium) LLC monomer motif (**4,** see Scheme 1.1 in Chapter 1) in 2012, the Gin and Noble research groups have reduced efforts towards the development of novel Q-phase-forming platforms. Instead, research was primarily directed towards applying monomer **4a** for a variety of membrane applications. Indeed, this monomer platform has demonstrated impressive water flux and salt rejection comparable to industrially relevant nanofiltration and reverse osmosis membranes.[1] Thin-film composite (TFC) membranes of **4a** have shown good water/(chemical warfare agent simulant) vapor selectivity compared to previously reported LLC-based membranes.[2] Despite these successes, little information was known about the tolerances of monomer **4a**. A full phase diagram of **4a** was never completed, and structure-property effects on the formation of the LLC Q phase of the bis(imidazolium) motif had yet to be explored. TFC Q_I membranes of cross-linked **4a** were also only capable of molecular size and charge discrimination – they did not incorporate additional functional properties or functional groups as other low-dimensionality LLC-based systems have been able to in the past.[3] In light of the current state of knowledge about the bis(imidazolium) platform monomer platform and intrinsically cross-linkable Q-phase-forming monomers in general, the objectives of the work presented herein are three-fold:

I. Explore the possibility of utilizing structure-property effects to tune the Q phase window of the bis(imidazolium) monomer platform to yield more processable LLC monomers than previous generations.

II. Design a novel Q-phase-forming LLC platform with reduced synthetic complexity and cost as well as the ability to incorporate added functional properties / functional groups.

III. Demonstrate the first example of a functionalized Q-phase monomer system or polymer network.

In pursuit of the first objective, seven homologs of monomer **4a** were synthesized and screened for their ability to form the Q phase. This work is presented in Chapter 3 of this thesis. It was found that although four of the seven monomer homologs demonstrated a Q phase in water or glycerol, only one of those homologs exhibited a well-ordered Q phase and wider phase window than **4a**. Chapter 3 also emphasizes that although the Q phase can be targeted with a variety of homologs, the ability to form a reliable Q phase was limited between one to four-carbon structural changes. These conclusions suggest that there is little that can be done structurally to improve the tunability or processability of the bis(imidazolium) monomer motif implying that it may be necessary to develop a new type of amphiphile for LLC-based applications.

Chapter 4 describes the development of a new, intrinsically cross-linkable, single-head/single-tail Q-phase-forming monomer motif. This monomer system features a novel structural motif that is cheaper and easier to synthesize compared to previous intrinsically cross-linkable Q-phase-forming amphiphile reported in the literature. Because this system is newly characterized, its ability to accept added functional groups while retaining the ability to form a Q-phase is unknown.

Chapter 5 capitalizes on known properties of spiropyrans as stimuli-responsive molecules and describes the development of a new spiropyran-containing monomer that, upon blending with the newly developed monomer described in Chapter 4, yields the first Q-phase polymer network material that can respond to changes in multiple external stimuli, allowing it to be used in potential gated transport or responsive/sensing uptake applications. The resulting nanoporous material exhibits reversible color and gyroid unit cell dimension/environment changes with changes in external aqueous solution and vapor pH. Furthermore, preliminary studies indicate that the same spiropyran-containing network has potential as a colorimetric indicating sorbent or gated-response material for certain types of aqueous metal ions.

2.2 References

1. Carter, B. M.; Wiesenauer, B. R.; Hatakeyama, E. S.; Barton, J. L.; Noble, R. D.; Gin, D. L. Glycerol-based Bicontinuous Cubic Lyotropic Liquid Crystal Monomer System for the Fabrication of Thin-film Membranes with Uniform Nanopores. *Chem. Mater*. **2012**, *22*, 4525–4527.
2. Dwulet, G. E.; Dischinger, S. M.; McGrath, M. J.; Basalla, A. J.; Malecha, J. J.; Noble, R. D.; Gin, D. L. Breathable, Polydopamine-Coated Nanoporous Membranes that Selectively Reject Nerve and Blister Agent Simulant Vapors. *Ind. Eng. Chem. Res.* **2019**, *58*, 21890–21893.
3. Dwulet, G. E.; Gin, D. L. Ordered nanoporous lyotropic liquid crystal polymer resin for heterogenous catalytic aerobic oxidation of alcohols. *Chem. Commun.* **2018**, 54, 12053–12056.

Chapter 3: Effects of Structural Modification of (Alkyldiene-Imidazolium Bromide)-Based Gemini Monomers on the Formation of the Lyotropic Bicontinuous Cubic Phase

(A modified version of this chapter was originally published as: Li, P.; Reinhardt, M. I.; Dyer, S. S.; Moore, K. E.; Imran, O. Q.; Gin, D. L. "Effects of structural modification of (alkyldiene-imidazolium bromide)-based gemini monomers on the formation of the lyotropic bicontinuous cubic phase." *Soft Matter* **2021**, *17*, 9259–9263.)

3.1 Abstract

Seven homologs of an amphiphile gemini monomer were synthesized and screened for the ability to form a bicontinuous cubic (Q) lyotropic liquid crystal phase. Four of these homologs form a Q phase with glycerol or water that can be cross-linked with retention of the nanoporous structure, with one exhibiting a well-ordered Q phase with a wider phase window than the parent monomer.

3.2 Introduction

Lyotropic liquid crystal (LLC) mesogens are amphiphilic molecules (i.e., surfactants) that self-assemble in the presence of aqueous or polar liquids to form ordered, phase-separated structures with monodisperse, nanometer-scale, hydrophilic channels (i.e., LLC phases).[1] These hydrophilic channels can have different dimensionalities and shapes, depending on the type of LLC phase formed (i.e., 1D hexagonal (H) phases, 2D lamellar (L) phases, 3D-interconnected bicontinuous cubic (Q) phases) and on whether the phase curves around the hydrophobic domains (i.e., normal/Type I) or the hydrophilic domains (inverted/Type II).[1] By using reactive

amphiphiles (i.e., LLC monomers), LLC phases can be cross-linked in situ to preserve the phase microstructure to form stable, ordered polymer networks with hydrophilic nanopores.[2] These materials have been used for templated nanocomposite synthesis,[2] heterogeneous catalysis,[2] molecular size separations,[2] and enhanced ion transport.[3]

Q phases are particularly attractive for many materials applications compared to other LLC phases because their periodic, 3D-interconnected pores do not need to be aligned for good transport and have a low probability of being blocked during membrane applications.[4] The formation of a particular LLC phase is usually composition-, temperature-, and pressure-dependent,[1] but LLC phase formation can also be influenced by altering the shape or packing structure of the amphiphile.[5] However, the design of LLC monomers that form Q phases and control of their phase behavior have not been straightforward, historically. This is because Q phases are considered intermediate structures between the L and H phases in terms of curvature and interfacial energy, [1,6] and amphiphile shape-based packing approaches to LLC phase formation do not explain Q systems.[5] Indeed, LLC monomer shape motifs known to form Q phases have ranged from symmetric gemini amphiphiles,[7-10] wedge-shaped amphiphiles,[11] and even simple one-head/one-tail amphiphiles.[14-16]

Several years ago, our group developed an (alkyldiene-imidazolium bromide)-based gemini (i.e., bridged two-head/two-tail) LLC monomer (**4a**) (Figure 3.1) that forms a Type I bicontinuous cubic (Q_I) phase with water or glycerol.[16] Monomer **4a** is modular and economical to synthesize compared to past Q-phase LLC monomers developed in our group.[17] It can also be processed into thin-film composite (TFC) membranes that perform molecular-size-based water nanofiltration and desalination[17] as well as selective vapor separations.[18] However, despite the

versatility of monomer **4a**, it has limitations in terms of utility due to its very narrow Q_I-phase window with respect to temperature and system composition.[17]

It has been empirically shown that the nature of the hydrophilic headgroups, the length of the linker between the headgroups, the length and type of hydrophobic tails, and the position of the bridge linker unit relative to the ionic headgroups can affect Q phase formation/stability and nanopore size for ionic gemini LLC mesogens in general.[1,8-10,19-21] However, only very preliminary studies have been conducted on the effect of structural variations on the formation of the Q_I phase for the (alkyldiene-imidazolium bromide) gemini LLC monomer platform. Specifically, only a very small number of homologs were initially synthesized in order to identify an initial suitable Q_I-phase candidate (i.e., monomer **4a** for polymerization and membrane studies.[19] Qualitative analysis revealed that the few homologs initially synthesized had the potential to adopt a Q phase.[17] However, the suspected Q phases were never confirmed, and structure-property trends for the effects of headgroup spacer length and polymerizable diene tail length on the Q_I phase formation have not been elucidated for this gemini monomer platform.[17]

Herein, we present the synthesis and LLC phase characterization of a series of seven homologs of (alkyldiene-imidazolium bromide) gemini monomer **4a** that span headgroup alkyl spacer lengths from four to nine carbons and polymerizable diene tails with a total length of either 14 or 18 carbons (Figure 3.1). Five of these homologs are new compounds; the other two have been synthesized previously and showed a possible, unconfirmed Q phase but have not been fully characterized in terms of LLC phase behavior.[17] Their ability to form Q phases in glycerol and water was characterized using a combination of polarized light microscopy (PLM) and powder X-ray diffraction (PXRD) analysis to generate partial phase diagrams up to a temperature of 95 °C. It was found that four of these seven homologs formed a. phase when blended with either glycerol

or water at elevated temperatures. Of the four homologs that formed a Q phase, three were centered around headgroup alkyl spacers in the five- and six-carbon range, regardless of the two polymerizable tail lengths explored. The remaining homolog formed a weakly-ordered Q phase and had a nine-carbon headgroup spacer and an 18-carbon diene tail. Two of these four homologs had exhibited a wider Q-phase window than **4a** in terms of temperature and composition range, but only one had a broader Q phase with a degree of order comparable to that of **4a**. Additionally, the formed Q phases of these homologs could be radically photo-cross-linked with retention of the phase microstructure to form free-standing, transparent bulk films.

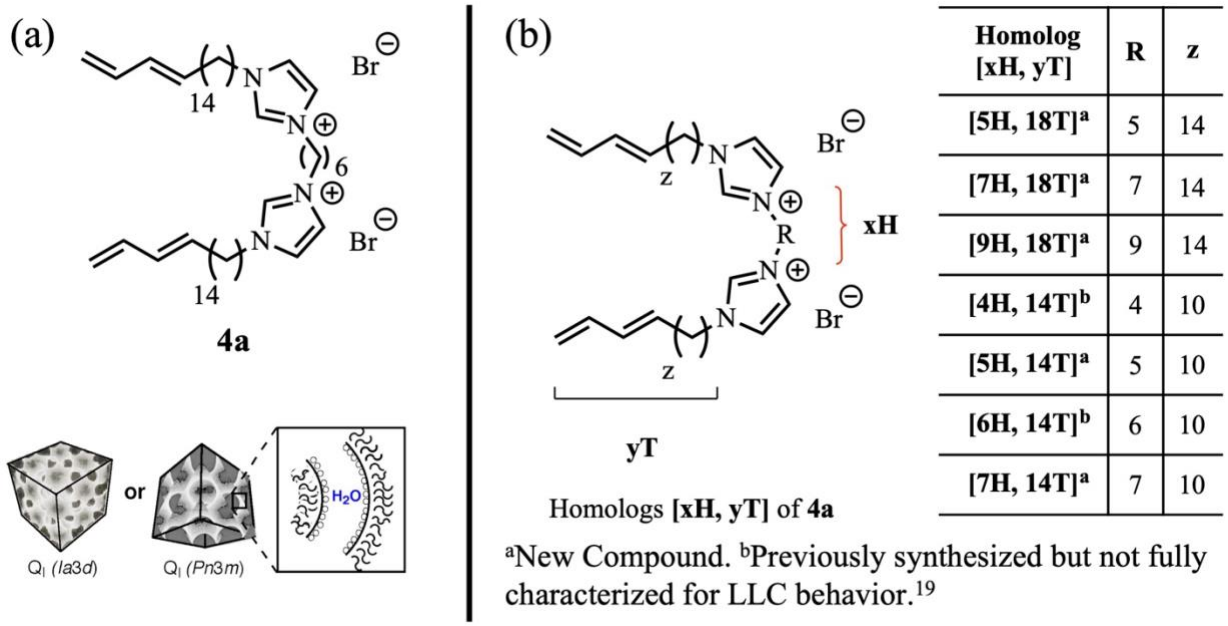

Homolog [xH, yT]	R	z
[5H, 18T][a]	5	14
[7H, 18T][a]	7	14
[9H, 18T][a]	9	14
[4H, 14T][b]	4	10
[5H, 14T][a]	5	10
[6H, 14T][b]	6	10
[7H, 14T][a]	7	10

Homologs **[xH, yT]** of **4a**

[a]New Compound. [b]Previously synthesized but not fully characterized for LLC behavior.[19]

Figure 3.1 (a) Structure of monomer **4a** and schematic representation of the Q_I phase that it forms. (Partially reproduced from Ref. 9. Copyright American Chemical Society, 2007.) (b) Structures of the homologs of **4a** prepared and studied in this work.

3.3 Results and Discussion

For simplicity of correlating structure with name, the seven monomer homologs shown in Figure 3.1b are labeled as **[xH, yT]**, where **x** refers to the total number of carbons in the headgroup spacer unit and **y** refers to the total number of carbons in the diene tails. These homologs were synthesized via S_N2 chemistry by reacting 2.3 equivalents of the appropriate-length bromoalkyl-1,3-diene[22,23] with 1.0 equivalent of the desired alkyl-bridged bis(imidazole)[24-26] in CH_3CN at 75 °C. After purification, the structure and purity of these homologs were verified by ^1H NMR, ^{13}C NMR, FT-IR, and elemental analyses (see Section 3.6.2 for full details). Because our main motivation in this work was to probe structure-property effects on Q-phase formation for this gemini monomer platform, we chose headgroup alkyl spacer lengths centered about the original six-carbon headgroup spacer of **4a**. 14- and 18-Carbon diene tail units were chosen for this detailed homolog study because these two polymerizable tails are the most readily synthesized from economical and available starting materials of the ω-bromoalkyl-1,3-diene tail systems reported in literature.[22,23]

The LLC phase behavior of these homologs was elucidated in the following manner: First, qualitative PLM-based penetration scan screening was performed in each homolog mixed with glycerol and separately water to determine which showed potential Q phase formation.[1c] This rapid LLC phase screening technique involved placing a sample between a microscope slide and cover slip and adding solvent to the edge of the cover slip to create a concentration gradient. The sample was then heated from 25 to 95 °C, and the optical textures observed were used to identify potential LLC phases formed. Specifically, a dark, isotropic band between two birefringent LLC phases indicated a potential Q phase.[1] Partial phase diagrams were then elucidated via PLM analysis of mixtures containing either glycerol or water, with a focus on quantitatively identifying

any Q phase regions. In this procedure, candidates that showed evidence of a potential Q phase by penetration scan screening were blended with glycerol or water to create a systematic series of compositions ranging from 5 to 95 wt% monomer. Each composition was then analyzed via variable-temperature PLM from 25 to 95 °C, using changes in PLM optical texture with temperature as phase transition points in order to plot the boundaries between different phases (see Section 3.5.4 for full details). The general LLC phase behavior of the homologs was elucidated using this procedure. It should be noted that homolog **[7H, 14T]** was not investigated further because it is a liquid at ambient temperature and thus not a viable candidate for forming ambient- or elevated-temperature LLC phases.

Quantitative identification of suspected Q phases (and other LLC phases) was done by room-temperature PXRD analysis of radically cross-linked bulk films of compositions located in the middle of each phase region (as identified by PLM), and/or by variable-temperature PXRD (VT-PXRD) analysis of unpolymerized LLC mixtures that were near the middle of the target phase region. In particular, Q phases can be identified by the presence of a black PLM optical texture and PXRD *d*-spacings with a ratio of $1/\sqrt{6}$: $1/\sqrt{8}$… (see the Supporting Information).[1,4] (However, the Q phase space group could not be determined due to the limited number of observable PXRD peaks). Cross-linked films of LLC mixtures (typical thickness: ca. 180 μm) were prepared by hand-mixing and centrifuging the appropriate amount of monomer and solvent with 1 wt% 2-hydroxy-2-methylpropriophenone (HMP, a radical photo-initiator) and irradiating the mixtures under 365 nm UV light for 1 h with heating if necessary (see Section 3.6.4 for full details). PXRD of cross-linked samples allowed for convenient quantitative confirmation of LLC phases at room temperature and avoided the potential risks of perturbing LLC phase formation through solvent evaporation or ambient water uptake. PXRD of cross-linked compositions also revealed if

particular LLC phases of a homolog could be retained after photopolymerization. VT-PXRD analysis of unpolymerized LLC mixtures for phase identification was used to check other non-Q-phase boundaries, or when PXRD analysis of a cross-linked composition point within a suspected Q-phase region was not informative enough to draw conclusions on the phase. To help confirm the structure of the Q phase formed by **[5H, 18T]** (i.e., our most promising homolog from PLM and PXRD analysis), a polymerized bulk film was sent to collaborators for more-detailed SAXS analysis, which is outside of our routine PXRD capabilities (see the Supporting Information).

Table 3.1 Summary of Q-phase behavior of monomer **4a** homologs as determined by PLM and PXRD analysis of mixtures to elucidate (partial phase diagrams).

Homolog [xH, yT]	Glycerol	Water
[5H, 18T][a]	*Q phase*	No Q phase (I phase only)
[7H, 18T][a]	No Q phase	No Q phase (I phase only)
[9H, 18T][a]	*Weakly ordered Q phase*	No Q phase
[4H, 14T][b]	No Q phase	No Q phase
[5H, 14T][a]	No Q phase	*Weakly ordered Q phase*
[6H, 14T][b]	No Q phase	*Weakly ordered Q phase*
[7H, 14T][a]	No Q phase	No Q phase

Table 3.1 summarizes the Q-phase formation behavior of the homologs of monomer **4a** evaluated by the aforementioned techniques. When potential Q-phase-forming homologs were mixed with glycerol, only homologs **[5H, 18T]** and **[9H, 18T]** demonstrated the ability to form a Q phase with glycerol only but not water. Relative to parent monomer **4a**, both **[5H, 18T]** and **[9H, 18T]** resulted in Q phases with wider phase windows in terms of temperature and lyotropic composition (Figure 3.2). However, only **[5H, 18T]** exhibited both a wider Q-phase window and comparable Q-phase order compared to monomer **4a** (see Figures 3.2 and 3.3). These trends for glycerol mixtures suggest that longer polymerizable diene tails coupled with headgroups with shorter alkyl spacers may favor a wider Q-phase window. To our surprise, **[7H, 18T]** did not

demonstrate the ability to form a Q phase with glycerol, despite having an alkyl headgroup spacer intermediate in length between **4a** and **[9H, 18T]**. It should be noted that a homolog of **4a** with a four-carbon alkyl headgroup spacer and 18-carbon diene tails (i.e., **[4H, 18T]**) was previously synthesized by our group; however, it also did not exhibit a potential Q phase in glycerol during initial screening.[17]

When the potential Q-phase-forming homologs were mixed with water, only homologs **[5H, 14T]** and **[6H, 14T]** demonstrated the ability to form a Q phase via PLM and PXRD analysis. Despite the fact that both **[5H, 14T]** and **[6H, 14T]** were able to form a Q phase with water, PXRD analysis revealed that the Q phase order was weaker than the Q phases of **4a** and **[5H, 18T]**. Homolog **[4H, 14T]** demonstrated the potential to form a Q phase via initial PLM penetration scan screening (see Figure 3.13); however, during phase diagram elucidation via PLM and PXRD, no data indicating a pure Q phase were observed. From Table 3.1 and the behavior of parent monomer **4a**, it appears that polymerizable diene tail length has the greatest overall impact on the ability of the (alkyldiene-imidazolium bromide) gemini monomer platform to form a Q phase in glycerol or water, with the most well-ordered Q phases centered about homologs with five- and six-carbon headgroup spacer lengths. No attempts were made to explore longer alkyl headgroup spacers because based on the observed trends, we believed that the Q phase would either not form or only less-ordered Q-phases than that of **[9H, 18T]** would form.

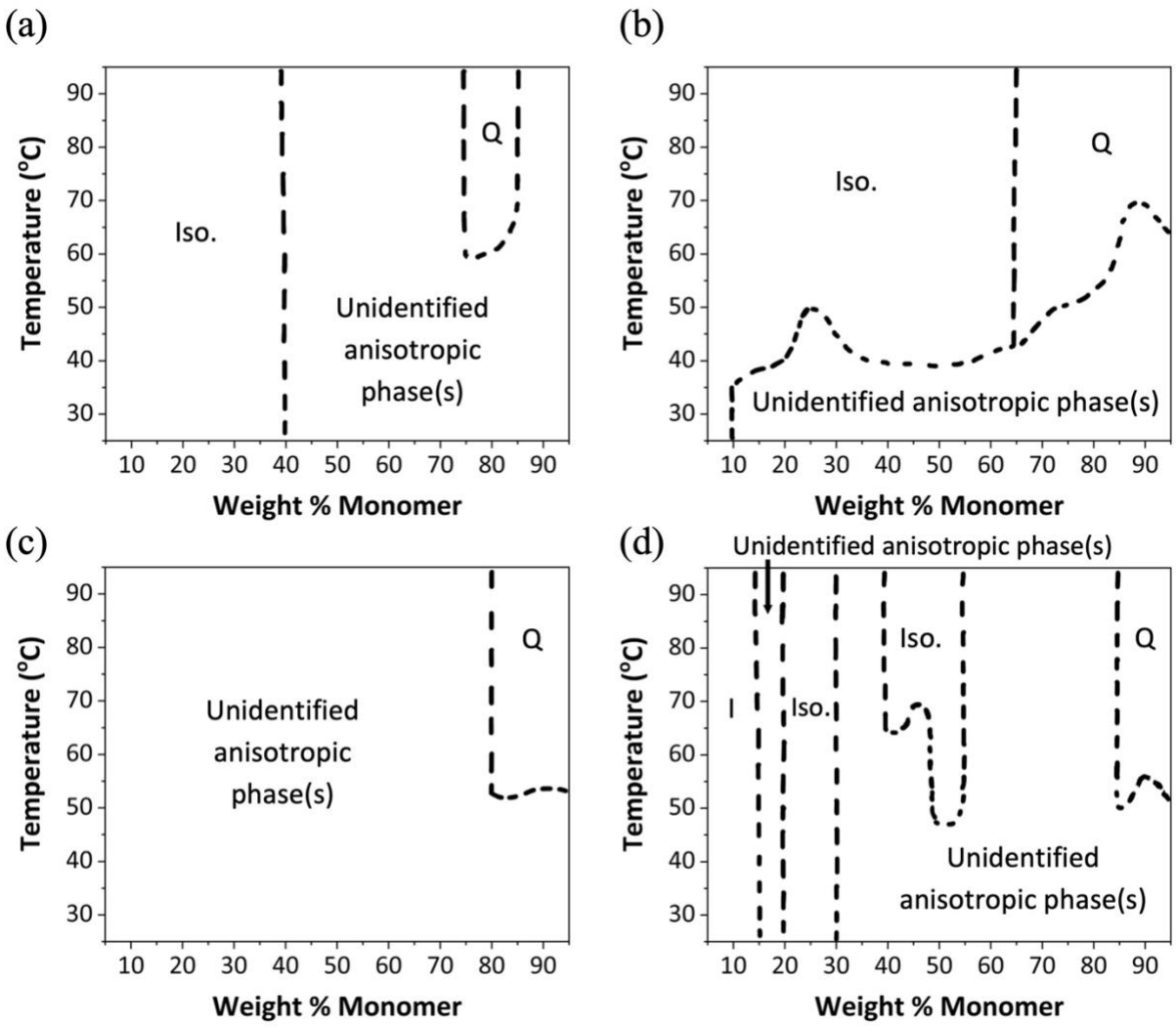

Figure 3.2 Partial phase diagrams of the four Q-phase-forming homologs: (a) **[5H, 18T]** with glycerol; (b) **[9H, 18T]** with glycerol; (c) **[5H, 14T]** with water; (d) **[6H, 14T]** with water. I = discontinuous cubic phase; Iso. = amorphous isotropic phase (i.e., no order by PXRD); Q = bicontinuous cubic phase. Heterogenous regions omitted. Note: Phase diagrams mapped out at Boulder, CO (altitude = 5,328 ft, ambient pressure = ca. 623 torr); they may be slightly different at other altitudes.

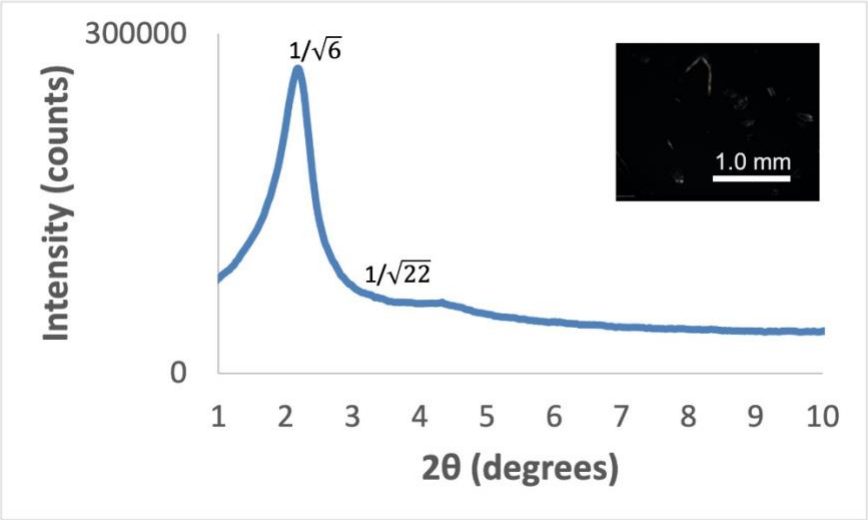

Figure 3.3 PXRD profile of a bulk cross-linked Q-phase film prepared from a mixture of **[5H, 18T]**/glycerol/HMP (79:20:1 (w/w/w)). Inset: PLM optical texture (50x).

During the process of quantitively determining the LLC phase boundaries, it was found that some aqueous LLC mixtures of **[5H, 18T]** and **[7H, 18T]** containing relatively low weight percentages of monomer (i.e., ca. ≤50 wt%) also displayed some physical traits of the Q phase (i.e., black PLM optical texture, relatively viscous). However, for original LLC monomer **4a**, the Q_I phase forms at very high weight percentages of monomer (≥85 wt%) relative to solvent.[17] The fact that some PXRD order was observed for these low-amphiphile-content aqueous mixtures of **[5H, 18T]** and **[7H, 18T]** indicated that a different type of an ordered, isotropic phase other than Q_I was likely present. We attributed optically isotropic, ordered phases to be a discontinuous cubic micellar (I) phase (i.e., a cubic-packed array of spherical micelles) based on correlation of the observed PLM and PXRD data with literature information on such I phases (see the Supporting Information for PXRD analysis).[27,28]

It should be noted that the Q phases identified for **[5H, 18T]**, **[9H, 18T]**, **[5H, 14T]**, and **[6H, 14T]** are most likely a Q_I phase, based on the LLC phase behavior of parent monomer **4a** and

the structural similarity of these homologs to **4a**. To unequivocally confirm a Q_I or Q_{II} phase, an L phase needs to be present in the phase diagram as a central reference point so that phases on the solvent-excessive side of the L phase can be assigned as Type I (normal) and ones on the solvent-deficient side can be assigned as Type II (inverted).[1] Unfortunately, none of the homologs investigated in this study that form a Q phase exhibited an identifiable L phase for this determination.

3.4 Conclusions

In summary, seven (alkyldiene-imidazolium bromide)-based gemini monomer homologs were synthesized, and their ability to form the Q phase in glycerol and in water was explored. Although four of these monomers demonstrated the ability to form a Q phase, only homolog **[5H, 18T]** displayed a wider Q-phase window than the original monomer **4a** while maintaining comparable Q-phase order. For this gemini imidazolium monomer platform, it appears that Q-phase formation is favored for homologs that have five- and six-carbon headgroup alkyl spacers, regardless of whether the diene tail is 14 or 18 carbons long. Additionally, well-ordered Q phases only appear to form for homologs with those headgroup spacer lengths if they also have the 18-carbon polymerizable diene tail and are blended with glycerol. Given that **[5H, 18T]** forms a Q phase with wider temperature and composition tolerances than monomer **4a** and retains its phase structure after cross-linking, we are interested in testing TFC Q membranes of this new homolog. The next stage of this research is to determine if **[5H, 18T]** membranes have a different nanopore size or different separation performance compared to membranes made with monomer **4a**.

3.5 Supporting Information

3.5.1 Instruments and Materials

NMR spectra were obtained using a Bruker Avance-III 300 NMR spectrometer (300 MHz for ^{1}H, 75 MHz for ^{13}C). Chemical shifts are reported in parts per million relative to the solvent residual signal ($CDCl_3$, δ_H = 7.26 ppm, δ_C = 77.16 ppm; DMSO-d_6, δ_H = 2.50 ppm, δ_C = 39.52 ppm). IR spectra (neat) were recorded using a Thermo Scientific Nicolet 6700 FT-IR equipped with a Pike MIRacle^{TM} single-reflection horizontal attenuated total reflectance accessory. Lyotropic liquid-crystalline (LLC) mixtures were homogenized, as needed, using an IEC Centra-CL2 centrifuge. Elemental analysis was performed by Galbraith Laboratories, Inc. Powder X-ray diffraction (PXRD) was the primary quantitative phase identification method used: PXRD spectra were obtained using an Inel CPS 120 diffraction system at the University of Colorado Boulder using a monochromated Cu K_α radiation source. This apparatus was equipped with a rotating flat, circular aluminum sample pan and a custom-built programmable sample heating stage for variable-temperature PXRD (VT-PXRD) of powder or spreadable samples using a conventional powder diffraction geometry. In addition, the PXRD instrument was equipped with a custom-made, sandwich-type, aluminum film holder with an open central window that allowed X-ray diffraction analysis of film samples by positioning the open face of the sample film directly in the path of the X-ray beam, between the beam source and the detector (i.e., through-film transmission mode). For both flat-pan PXRD or through-film configurations, all PXRD spectra were calibrated against a silver behenate diffraction standard (d_{100} = 58.4 Å) loaded in the same sample configuration and using the appropriate diffraction geometry as described for each method.[29] In the case of the through-film transmission configuration, the silver behenate powder was sandwiched between Mylar sheets before placing in the film holder apparatus. To help confirm/verify the Q phase

information provided by PXRD, small-angle X-ray scattering (SAXS) was performed on a single sample previously analyzed by PXRD by collaborators at the University of Pennsylvania as a special one-time, non-routine request. SAXS spectra were measured using a Xenocs Xeuss 2.0 system in the Dual Source and Environmental X-ray Scattering (DEXS) facility at the University of Pennsylvania. A GeniX3D Cu source with a wavelength of $\lambda = 1.54$ Å was used, with a typical sample-to-detector distance of 37.5 cm, providing a range of accessible scattering vectors (q) from 0.016 to 1.4 $Å^{-1}$. Silver behenate was used as a standard for calibrating the SAXS sample-to-detector distance, and film samples were packed between Kapton windows. Foxtrot software was used for azimuthal integration of scattering patterns into 1-D plots of scattering intensity (I) vs. q, where $q = 4\pi\sin(\theta)/\lambda$ and the scattering angle is 2θ. Variable-temperature polarized light microscopy (PLM) studies were performed using a Leica DMRXP polarizing light microscope equipped with a Q-Imaging MicroPublisher 3.3 RTV digital camera, a Linkam LTS 350 thermal stage, and a Linkam CI 94 temperature controller. Automatic temperature profiles and image captures were performed using Linkam Linksys32 software. Radical photopolymerizations were conducted using a Spectroline XX-15A 365 nm UV lamp (8.5 mW/cm^2 at the sample surface). UV light fluxes at the sample surface were measured using a Spectroline DCR-100X digital radiometer equipped with a DIX-365 UV-A sensor.

Chromium(VI) oxide, pyridine, *tert*-butyllithium (1.6 M in pentane), hydrogen bromide (48 wt. % in H_2O), borane-tetrahydrofuran complex solution (1.0 M in THF), sodium hydride (60 wt. % dispersion in mineral oil), imidazole, *ω*-pentadecalactone (98%), 2-hydroxy-2-methylpropiophenone (HMP, 97%), sulfuric acid, 1,4-dibromobutane (99%), 1,6-dibromohexane (96%), triethanolamine (98%), and Florisil® (<200 mesh) were purchased from the Sigma-Aldrich Chemical Co. and used as received unless otherwise specified. 11-Bromo-1-undecanol (97%),

1,5-dibromopentane (98%), 1,7-dibromoheptane (98%), 1,9-dibromononane (97%), *N,N,N',N',*-tetramethylethylenediamine (98%), allyltrimethylsilane (98%), and 2-isopropoxy-4,4,5,5-tetramethyl-1,3,2-dioxaborolane (98%) were purchased from TCI America and used as received unless otherwise specified. Aluminum oxide (neutral, act. I, 50-200 μm) and silica gel (normal-phase, 200 x 400 mesh) were purchased from Sorbent Technologies. Glycerol (ACS Reagent) was purchased from Mallinckrodt and used as received. Sodium hydroxide, sodium chloride, magnesium sulfate, Celite™ 545, and hydrochloric acid (all ACS Reagents) were purchased from Fisher Scientific and used as received. All reaction solvents were obtained from the Sigma-Aldrich Chemical Co. and were purified/dehydrated via vacuum distillation and then de-gassed by repeated freeze-pump-thaw cycles and stored under Ar. All chemical syntheses were carried out under a dry Ar atmosphere using standard Schlenk line techniques unless otherwise noted.

3.5.2 New LLC monomer synthesis and characterization

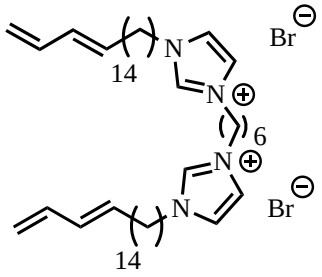

4a

Figure 3.4 Structure of gemini LLC monomer **4a**.

The seven homologs of Q_I-phase-forming monomer **4a** (Figure 3.4),[17] were prepared as shown in Figure 3.5 below. Detailed synthesis and structural characterization information on each of these new monomers are listed below. The newly synthesized homologs are hygroscopic, ionic

organic compounds that are difficult to dry completely and usually do not combust well. However, their obtained elemental analysis values are within the accepted ±0.4% tolerance range for C, H, and N to be considered pure when the presence of associated water molecules is accounted for (as for prior monomer **1**).[8] To help verify the purities of the new homologs, example ^{1}H and ^{13}C NMR spectra of some of the final monomers have also been included at the end of the Supporting Information to show the lack of impurities other than associated water.

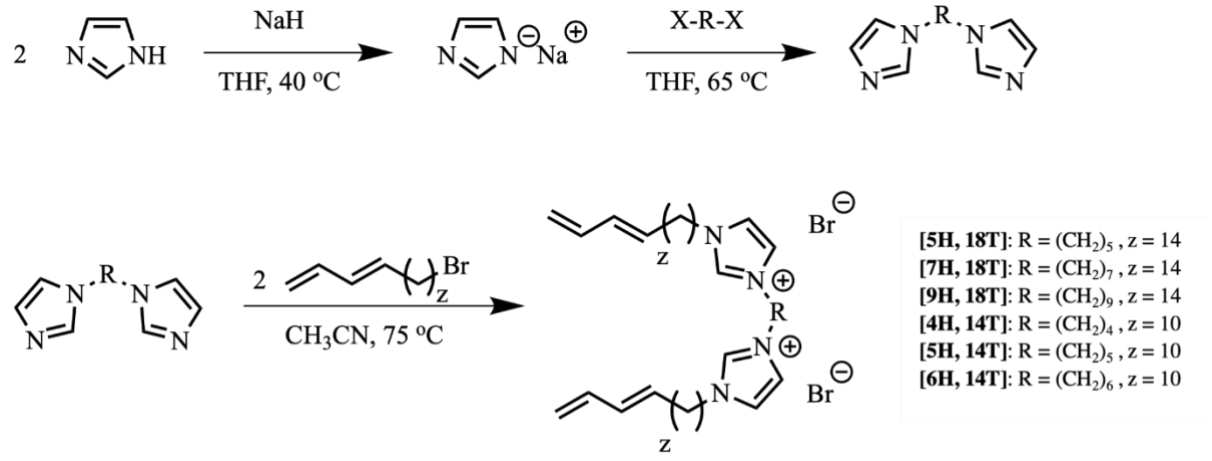

Figure 3.5 General synthetic scheme for the seven monomer **4a** homologs that were tested for Q-phase formation in the presence of glycerol and water.

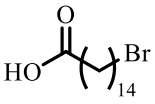

15-Bromopentadecanoic acid.[23] ω-Pentadecalactone (50.00 g, 0.2080 mol, 1.000 equiv.) was stirred in 48 wt. % aq. HBr (295.2 mL, 2.610 mol, 12.55 equiv.) in a 500-mL round-bottom flask equipped with a stir bar and reflux condenser. Conc. H_2SO_4 (33.26 mL, 0.6240 mol, 3.000 equiv.) was added dropwise to minimize exothermic activity, liquefying the solid lactone. The solution was heated to 120 °C and stirred for 84 h. The solution was cooled to room temperature and then

decanted, leaving a black solid disc behind in the round-bottom flask. The disc was rinsed with de-ionized (DI) H_2O (2 x 200 mL), and the rinse was discarded. CH_2Cl_2 (300 mL) was then added to the flask, and the solution was heated to 35 °C and stirred until the black disc was completely dissolved. The resulting organic solution was filtered through a pad of Celite™ 545. The resulting filtrate was washed with DI H_2O (2 x 200 mL), brine (2 x 200 mL), and DI H_2O again (2 x 200 mL). The black film that formed between the organic and aqueous phases was discarded, and the organic phase was then dried over anhydrous $MgSO_4$. The resulting organic solution was reduced by rotary evaporation to afford an off-white, crystalline solid (54.85 g, 82%). Spectroscopic characterization and purity data for this compound matched published data.[23]

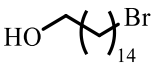

15-Bromopentadecanol.[23] Borane-THF complex solution (234.0 mL, 0.2340 mol, 1.504 equiv.) was cannula transferred under Ar into a 500-mL three-neck round-bottom flask equipped with a stir bar. 15-Bromopentadecanoic acid (50.00 g, 0.1556 mol, 1.000 equiv.) was added slowly at 0 °C to minimize bubbling. The light-yellow solution was warmed to room temperature and then stirred under Ar for 24 h. The reaction solution was then quenched with DI H_2O (200 mL) followed by 1.2 M aq. HCl (15.00 mL). The resulting mixture was then extracted with Et_2O (2 x 150 mL) and washed with brine (3 x 250 mL). The organic phase was then dried over anhydrous $MgSO_4$. The resulting organic solution was reduced by rotary evaporation to afford an off-white, powder. The resulting powder was recrystallized from hot MeOH and washed with cold MeOH to afford the product as a white, crystalline solid (40.27 g, 84%). Spectroscopic characterization and purity data for this compound matched published data.[23]

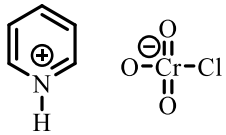

Pyridinium chlorochromate (PCC) on alumina.[30]

The following procedure was performed in air with materials used as purchased. 6 M Aq. HCl (111.7 mL, 0.6701 mol, 1.340 equiv.) was added to a 1-L round-bottom flask and stirred. Chromium (VI) oxide (50.00 g, 0.5001 mol, 1.000 equiv.) was added slowly and the reaction mixture was cooled in an ice bath. Anhydrous pyridine (40.45 mL, 0.5001 mol, 1.000 equiv.) was then added slowly. The orange reaction slurry was raised to 45 °C and stirred until the mixture became a homogeneous liquid. The reaction mixture was then removed from heat, and alumina (neutral, act. I, 50–200 μm, 368 g) was added slowly. The resulting mixture was manually stirred until all the alumina was uniformly coated. The mixture was then dried in air overnight at ambient temperature, and then dried in vacuo at ambient temperature to give the product as a bright orange powder (476.2 g, 1.050 x 10^{-3} mol PCC/g, 100%).

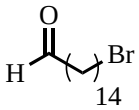

15-Bromopentadecanal.[23] PCC on alumina (55.78 g, 0.05850 mol, 1.800 equiv.) was added to a 500 mL three-neck round-bottom flask equipped with a stir bar. CH_2Cl_2 (300 mL, not anhydrous) was added to the reaction flask and the solution was stirred at a moderate speed. 15-Bromopentadecanol (10.00 g, 0.03250 mol, 1.000 equiv.) was added and the reaction flask was stoppered with a rubber septum with a venting needle. The needle was removed after 1 h, and the reaction slurry was stirred vigorously for 12 h. The reaction slurry was passed through a 150-mL fritted funnel filled with 0.5 cm of silica gel, 2 cm of Florisil®, and another 0.5 cm of silica gel

with additional CH_2Cl_2 (400 mL). Concentration of the CH_2Cl_2 under rotary evaporation afforded the product as a white solid (9.62 g, 97%). Spectroscopic characterization and purity data for this compound matched published data.[23]

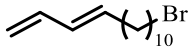

14-Bromotetradeca-1,3-diene.[22] This compound was synthesized as described in the literature.[22] Spectroscopic characterization and purity data for this compound matched published data.[22]

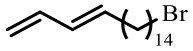

18-Bromooctadeca-1,3-diene.[22] This compound was synthesized as described in the literature.[22] Spectroscopic characterization and purity data for this compound matched published data.[22]

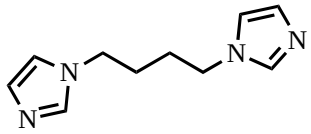

1,1'-(1,4-Butanediyl)bisimidazole.[17] 60 wt. % Sodium hydride in mineral oil (1.711 g, 0.04278 mol, 2.800 equiv.) and THF (150 mL) were added to a 250 mL, three-neck, round-bottom flask equipped with a reflux condenser and stir bar. The slurry was cooled to 0 °C, and imidazole (2.289 g, 0.03362 mol, 2.200 equiv.) was added slowly. The resulting mixture was heated at 40 °C for 15 min. 1,4-Dibromobutane (3.300 g, 0.01528 mol, 1.000 equiv.) was then injected, and the reaction mixture was stirred at 65 °C for 12 h. The contents of the flask were filtered and washed with additional THF (50 mL). The filtrate was concentrated under rotary evaporation to afford a yellow-orange oil. The resulting oil was dissolved in CH_2Cl_2 (100 mL), extracted with 1.2 M aq. HCl (100 mL), and washed with CH_2Cl_2 (3 x 100 mL). 1 M Aq. NaOH was added to the aqueous

layer until a pH of 8 was achieved, and this aqueous solution was then extracted with CH_2Cl_2 (3 x 100 mL). The combined CH_2Cl_2 extracts were dried over anhydrous $MgSO_4$ and then concentrated by rotary evaporation to afford the product as a white solid (1.4195 g, 49%). Spectroscopic characterization and purity data for this compound matched published data.[17]

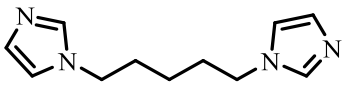

1,1'-(1,5-Pentanediyl)bisimidazole.[24] This compound was synthesized as described in the literature.[24] Spectroscopic characterization and purity data for this compound matched published data.[24]

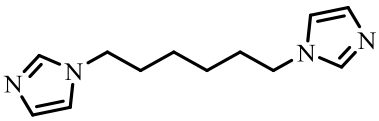

1,1'-(1,6-Hexanediyl)bisimidazole.[25] This compound was synthesized as described in the literature.[25] Spectroscopic characterization and purity data for this compound matched published data.[25]

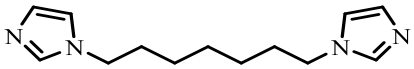

1,1'-(1,7-Heptanediyl)bisimidazole.[24] This compound was synthesized in a similar way as 1,1'-(1,4-butanediyl)bisimidazole but using 1,7-dibromoheptane instead of 1,4-dibromobutane. Spectroscopic characterization and purity data for this compound matched published data.[24]

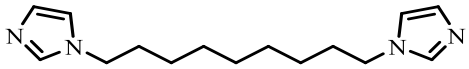

1,1'-(1,9-Nonanediyl)bisimidazole.[26] This compound was synthesized in a similar way as 1,1'-(1,4-butanediyl)bisimidazole but using 1,9-dibromononane instead of 1,4-dibromobutane. Spectroscopic characterization and purity data for this compound matched published data.[26]

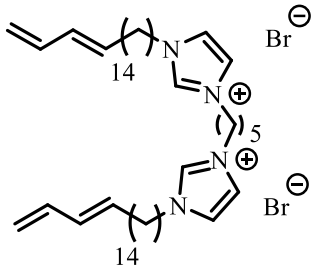

1,5-Bis(octadeca-15,17-dienylimidazolium)pentane dibromide [5H, 18T]. 18-Bromooctadeca-1,3-diene (1.04 g, 3.16 mmol, 2.31 equiv.) and 1,1'-(1,5-pentanediyl)bisimidazole (0.29 g, 1.4 mmol, 1.0 equiv.) were dissolved in CH_3CN (15 mL) in a 15-mL Schlenk flask equipped with a stir bar. The solution was stirred at 75 °C for 72 h in the dark. The contents of the Schlenk flask were cooled to room temperature, transferred to a 250-mL round-bottom flask equipped with a stir bar, and precipitated from Et_2O (200 mL). The resulting mixture was stirred at room temperature for 30 min, filtered, washed with additional Et_2O (100 mL), and dried in vacuo to give **[5H, 18T]** as a white solid (1.10 g, 93%). ^{1}H NMR (300 MHz, DMSO-d_6): δ 9.30 (t, J = 1.6 Hz, 1H), 7.82 (dd, J = 1.6, 0.6 Hz, 2H), 6.35 – 6.19 (m, 1H), 6.15 – 5.94 (m, 1H), 5.81 – 5.63 (m, 1H), 5.14 – 4.88 (m, 2H), 4.17 (q, J = 6.9 Hz, 4H), 2.03 (t, J = 7.0 Hz, 2H), 1.81 (dt, J = 14.8, 7.4 Hz, 4H), 1.41 – 1.13 (m, 24H). ^{13}C NMR (75 MHz, DMSO-d_6): δ 137.21, 135.97, 135.26, 130.86, 122.44, 115.07, 48.84, 48.43, 31.87, 29.33, 29.02, 28.98, 28.95, 28.84, 28.60, 28.57, 28.36, 25.51. FTIR (neat): 3057, 2918, 2850, 1565, 1463, 1162, 1012, 1001, 916, 835, 723 cm^{-1}. Calc. for

$C_{47}H_{82}Br_2N_4$: C, 65.41; H, 9.58; N, 6.49. Calc. for $C_{47}H_{82}Br_2N_4 \bullet 0.5H_2O$: C, 64.74; H, 9.59; N, 6.43. Found: C, 64.65; H, 9.29; N, 6.37.

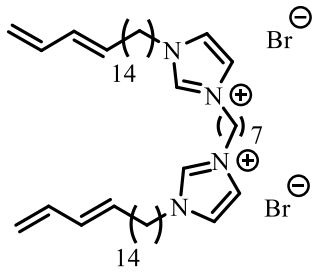

1,7-Bis(octadeca-15,17-dienylimidazolium)heptane dibromide [7H, 18T]. 18-Bromooctadeca-1,3-diene (1.02 g, 3.10 mmol, 2.30 equiv.) and 1,1'-(1,7-heptanediyl)bisimidazole (0.313 g, 1.35 mmol, 1.00 equiv.) were dissolved in CH_3CN (15 mL) in a 15-mL Schlenk flask equipped with a stir bar. The solution was stirred at 75 °C for 72 h in the dark. The contents of the Schlenk flask were cooled to room temperature, transferred to a 250-mL round-bottom flask equipped with a stir bar, and precipitated from Et_2O (200 mL). The resulting mixture was stirred at room temperature for 30 min, filtered, washed with additional Et_2O (100 mL), and dried in vacuo to give **[7H, 18T]** as a white solid (1.12 g, 93%). ^{1}H NMR (300 MHz, DMSO-d_6): δ 9.30 (s, 2H), 7.82 (d, J = 1.6 Hz, 4H), 6.41 – 6.15 (m, 2H), 6.12 – 5.92 (m, 2H), 5.82 – 5.61 (m, 2H), 5.15 – 4.86 (m, 4H), 4.16 (t, J = 7.2 Hz, 8H), 2.04 (q, J = 6.7 Hz, 4H), 1.78 (p, J = 7.3 Hz, 8H), 1.47 – 1.08 (m, 53H). ^{13}C NMR (75 MHz, DMSO-d_6): δ 137.20, 135.93, 135.26, 130.86, 122.44, 115.06, 48.81, 48.73, 31.87, 29.28, 29.18, 29.02, 28.98, 28.92, 28.83, 28.59, 28.57, 28.32, 25.47, 25.29. FTIR (neat): 2981, 2917, 2850, 1561, 1467, 1164, 1002, 949, 916, 820, 721 cm^{-1}. Calc. for $C_{49}H_{86}Br_2N_4$: C, 66.05; H, 9.73; N, 6.29. Calc. for $C_{49}H_{86}Br_2N_4 \bullet 0.5H_2O$: C, 65.39; H, 9.74; N, 6.22. Found: C, 65.55; H, 10.06; N, 6.30.

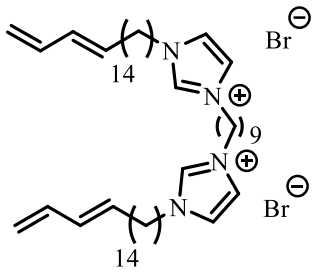

1,9-Bis(octadeca-15,17-dienylimidazolium)nonane dibromide [9H, 18T]. 18-Bromooctadeca-1,3-diene (1.25 g, 3.80 mol, 2.30 equiv.) and 1,1'-(1,9-nonanediyl)bisimidazole (0.43 g, 1.7 mol, 1.0 equiv.) were dissolved in CH_3CN (15 mL) in a 15-mL Schlenk flask equipped with a stir bar. The solution was stirred at 75 °C for 72 h in the dark. The contents of the Schlenk flask were cooled to room temperature, transferred to a 250-mL round-bottom flask equipped with a stir bar, and precipitated from Et_2O (200 mL). The resulting mixture was stirred at room temperature for 30 min, filtered, washed with additional Et_2O (100 mL), and dried in vacuo to give **[9H, 18T]** as a white solid (1.31 g, 86%). ^{1}H NMR (300 MHz, DMSO-d_6): δ 9.29 (t, J = 1.6 Hz, 2H), 7.82 (d, J = 1.6 Hz, 4H), 6.41 – 6.15 (m, 2H), 6.17 – 5.92 (m, 2H), 5.82 – 5.63 (m, 2H), 5.13 – 4.91 (m, 4H), 4.16 (t, J = 7.1 Hz, 8H), 2.04 (q, J = 6.7 Hz, 4H), 1.78 (p, J = 7.3 Hz, 8H), 1.41 – 1.10 (m, 56H). ^{13}C NMR (75 MHz, DMSO-d_6): δ 137.20, 135.94, 135.25, 130.86, 122.45, 115.06, 48.80, 31.87, 29.29, 29.26, 29.01, 28.98, 28.90, 28.83, 28.59, 28.57, 28.31, 28.28, 25.47, 25.44. FTIR (neat): 2918, 2850, 1561, 1467, 1165, 1003, 949, 919, 836, 746, 721 cm^{-1}. Calc. for $C_{51}H_{90}Br_2N_4$: C, 66.65; H, 9.87; N, 6.10. Calc. for $C_{51}H_{90}Br_2N_4 \bullet 1.5H_2O$: C, 64.74; H, 9.91; N, 5.92. Found: C, 64.70; H, 9.57; N, 5.90.

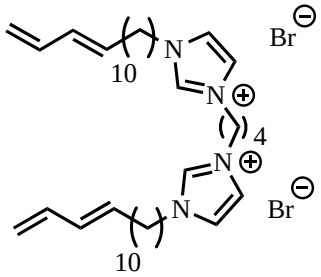

1,4-Bis(tetradeca-11,13-dienylimidazolium)butane dibromide [4H, 14T].[17] This compound was synthesized in a similar way as 1,5-bis(octadeca-15,17-dienylimidazolium)pentane dibromide but using 1,1'-(1,4-butanediyl)bisimidazole instead of 1,1'-(1,5-pentanediyl)bisimidazole and 14-bromotetradeca-1,3-diene instead of 18-bromooctadeca-1,3-diene. Spectroscopic characterization and purity data for this compound matched published data.[17]

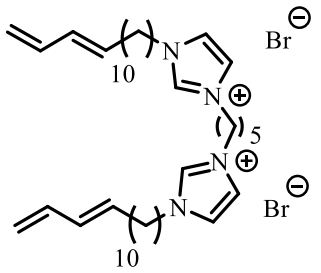

1,5-Bis(tetradeca-11,13-dienylimidazolium)pentane dibromide [5H, 14T]. 14-Bromotetradeca-1,3-diene (1.46 g, 5.34 mmol, 2.27 equiv.) and 1,1'-(1,5-pentanediyl)bisimidazole (0.47 g, 2.4 mmol, 1.0 equiv.) were dissolved in CH_3CN (15 mL) in a 15-mL Schlenk flask equipped with a stir bar. The solution was stirred at 75 °C for 72 h in the dark. The contents of the Schlenk flask were cooled to room temperature, transferred to a 250-mL round-bottom flask equipped with a stir bar, and precipitated from Et_2O (200 mL). The resulting mixture was stirred at room temperature for 30 min, filtered, washed with additional Et_2O (100 mL), and dried in vacuo to give **[5H, 14T]** as a white solid (1.60 g, 91%). ^{1}H NMR (300 MHz, DMSO-d_6): δ 9.32 (t, J = 1.6 Hz, 2H), 7.83 (p, J = 1.9 Hz, 4H), 6.40 – 6.18 (m, 2H), 6.12 – 5.94

(m, 2H), 5.79 – 5.59 (m, 2H), 5.13 – 4.87 (m, 4H), 4.18 (q, J = 7.0 Hz, 8H), 2.04 (q, J = 6.7 Hz, 4H), 1.81 (dp, J = 14.3, 7.1 Hz, 8H), 1.50 – 1.15 (m, 32H). ^{13}C NMR (75 MHz, DMSO-d_6): δ 137.20, 135.98, 135.25, 130.87, 122.44, 115.09, 48.83, 48.42, 31.87, 29.32, 28.87, 28.80, 28.60, 28.57, 28.33, 25.50, 22.02. FTIR (neat): 3054, 2919, 2852, 1564, 1462, 1161, 1012, 1002, 916, 831, 749, 723 cm^{-1}. Calc. for $C_{39}H_{66}Br_2N_4$: C, 62.39; H, 8.86; N, 7.46. Calc. for $C_{39}H_{66}Br_2N_4 \cdot 1.5H_2O$: C, 60.22; H, 8.94; N, 7.20. Found: C, 60.23; H, 8.74; N, 7.18.

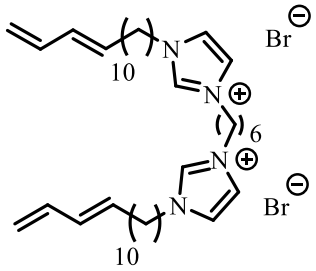

1,6-Bis(tetradeca-11,13-dienylimidazolium)hexane dibromide [6H, 14T].[17] This compound was synthesized in a similar way as 1,5-bis(octadeca-15,17-dienylimidazolium)pentane dibromide but using 1,1'-(1,6-hexanediyl)bisimidazole instead of 1,1'-(1,5-pentanediyl)bisimidazole and 14-bromotetradeca-1,3-diene instead of 18-bromooctadeca-1,3-diene. Spectroscopic characterization and purity data for this compound matched published data.[17]

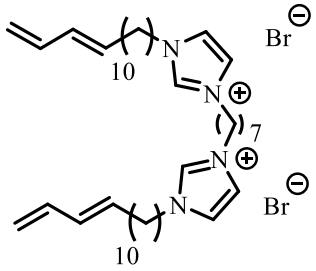

1,7-Bis(tetradeca-11,13-dienylimidazolium)heptane dibromide [7H, 14T]. 14-Bromotetradeca-1,3-diene (1.62 g, 5.93 mmol, 2.30 equiv.) and 1,1'-(1,7-

heptanediyl)bisimidazole (0.60 g, 2.6 mmol, 1.0 equiv.) were dissolved in CH_3CN (15 mL) in a 15-mL Schlenk flask equipped with a stir bar. The solution was stirred at 75 °C for 72 h in the dark. The contents of the Schlenk flask were cooled to room temperature, transferred to a 250-mL round-bottom flask equipped with a stir bar, and precipitated from Et_2O (200 mL). The resulting mixture was stirred at room temperature for 30 min, filtered, washed with additional Et_2O (100 mL), and dried in vacuo to give **[7H, 14T]** as a white solid (1.41 g, 70%). ^1H NMR (300 MHz, DMSO-d_6): δ 9.23 (t, J = 1.6 Hz, 2H), 7.85 – 7.64 (m, 4H), 6.45 – 6.14 (m, 2H), 6.11 – 5.90 (m, 2H), 5.81 – 5.57 (m, 2H), 5.14 – 4.90 (m, 4H), 4.15 (t, J = 7.2 Hz, 8H), 2.04 (q, J = 7.0 Hz, 4H), 1.79 (q, J = 7.2 Hz, 8H), 1.51 – 1.02 (m, 37H). ^{13}C NMR (75 MHz, DMSO-d_6): δ 137.21, 135.92, 135.26, 130.88, 122.45, 115.11, 48.83, 48.75, 31.88, 29.28, 29.20, 28.85, 28.81, 28.79, 28.61, 28.58, 28.30, 27.69, 25.46, 25.31. FTIR (neat): 3068, 2923, 2853, 1562, 1461, 1162, 1022, 972, 842, 724 cm^{-1}. Calc. for $C_{41}H_{70}Br_2N_4$: C, 63.23; H, 9.06; N, 7.19. Calc. for $C_{41}H_{70}Br_2N_4 \bullet 0.5H_2O$: C, 62.51; H, 9.08; N, 7.11. Found: C, 62.24; H, 9.15; N, 7.10.

3.5.2.1 NMR Spectra

Included below are NMR spectra of several monomers demonstrating that for each homolog the chemical shifts remained consistent while the integration values of the alkyl regions changed.

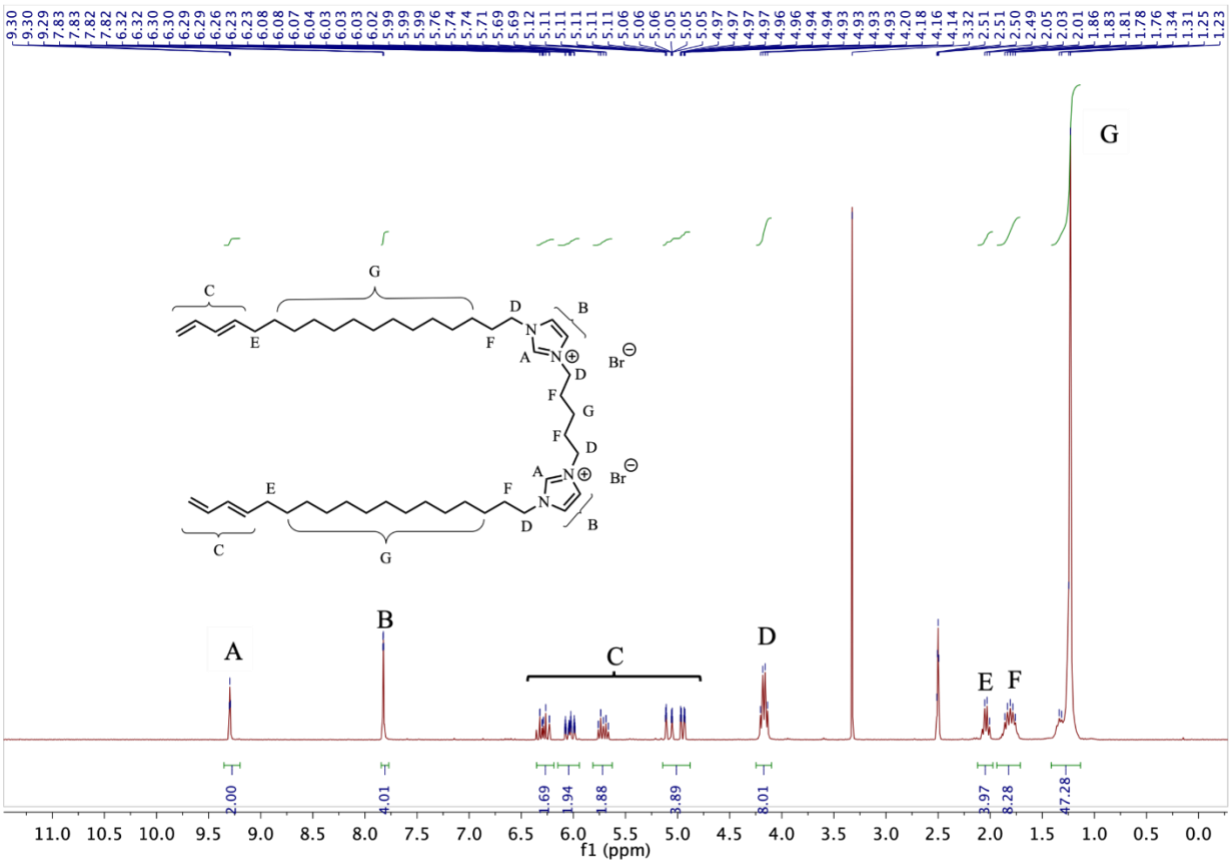

Figure 3.6 ^{1}H NMR spectrum of **[5H, 18T]** in DMSO-*d*$_6$.

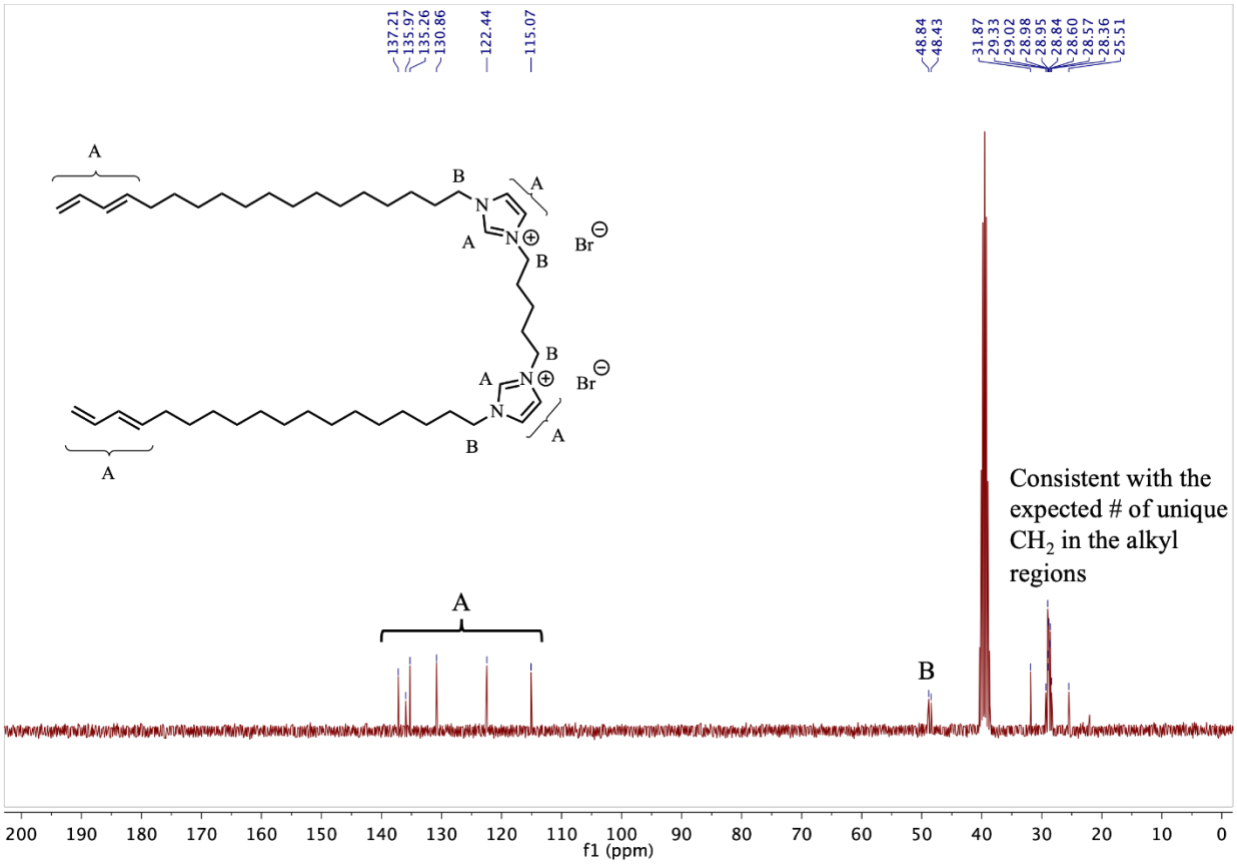

Figure 3.7 ^{13}C NMR spectrum of **[5H, 18T]** in DMSO-*d*$_6$.

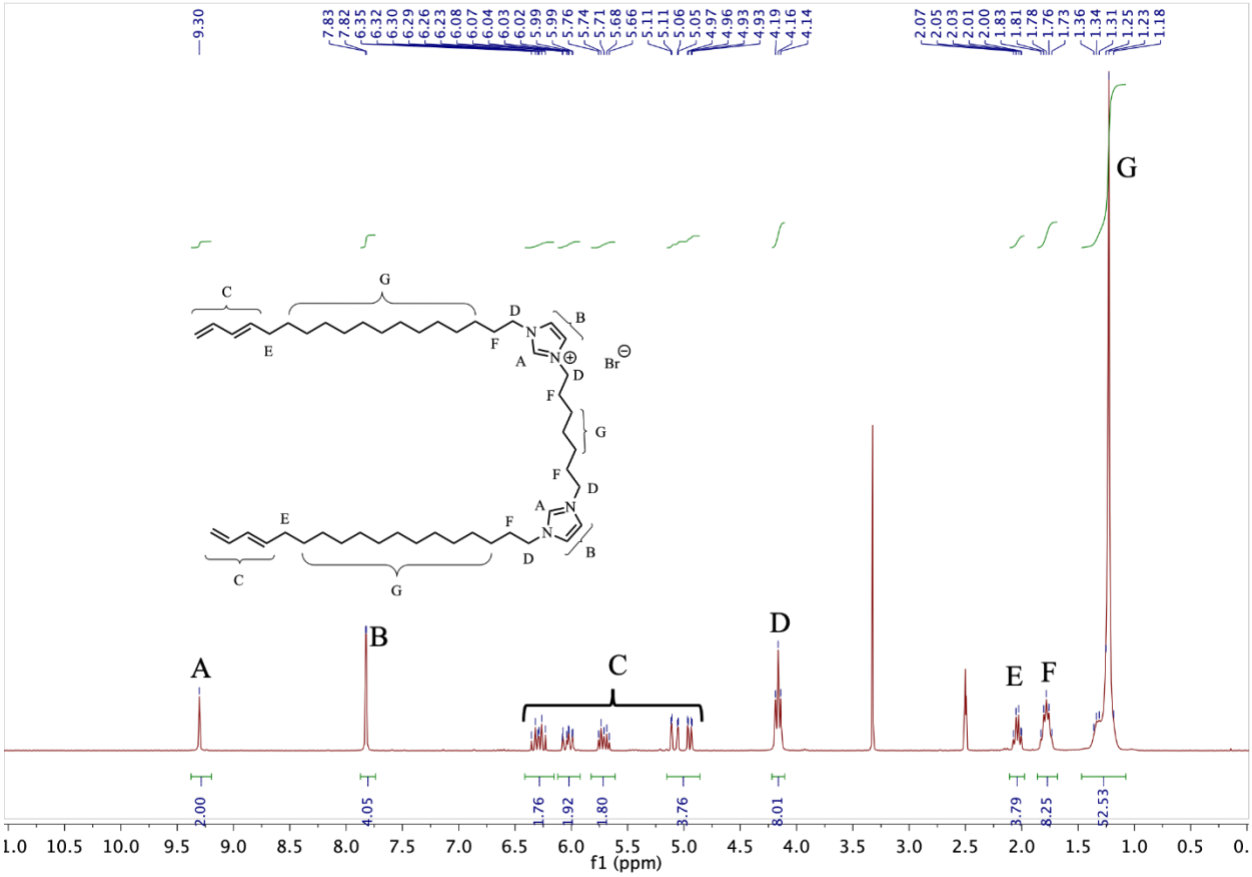

Figure 3.8 ^{1}H NMR spectrum of **[7H, 18T]** in DMSO-d_6.

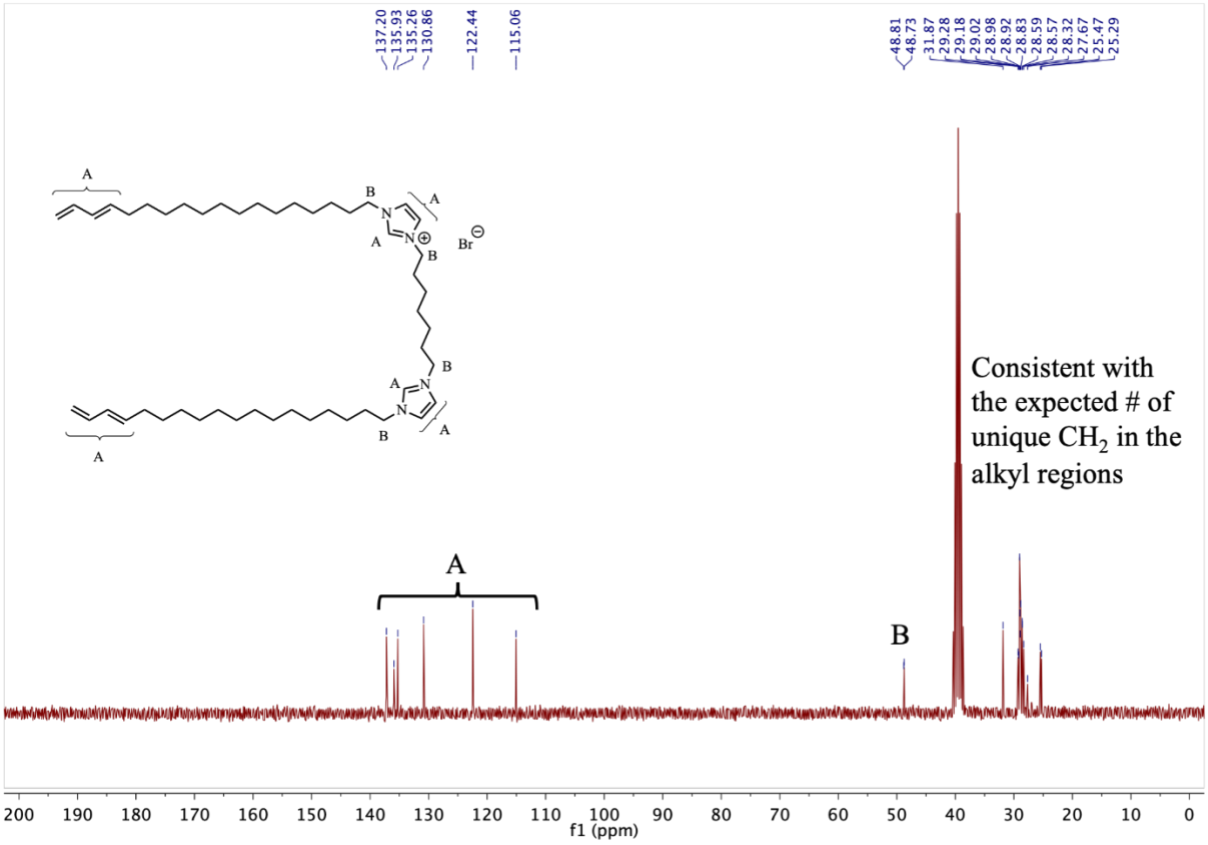

Figure 3.9 ^{13}C NMR spectrum of **[7H, 18T]** in DMSO-d_6.

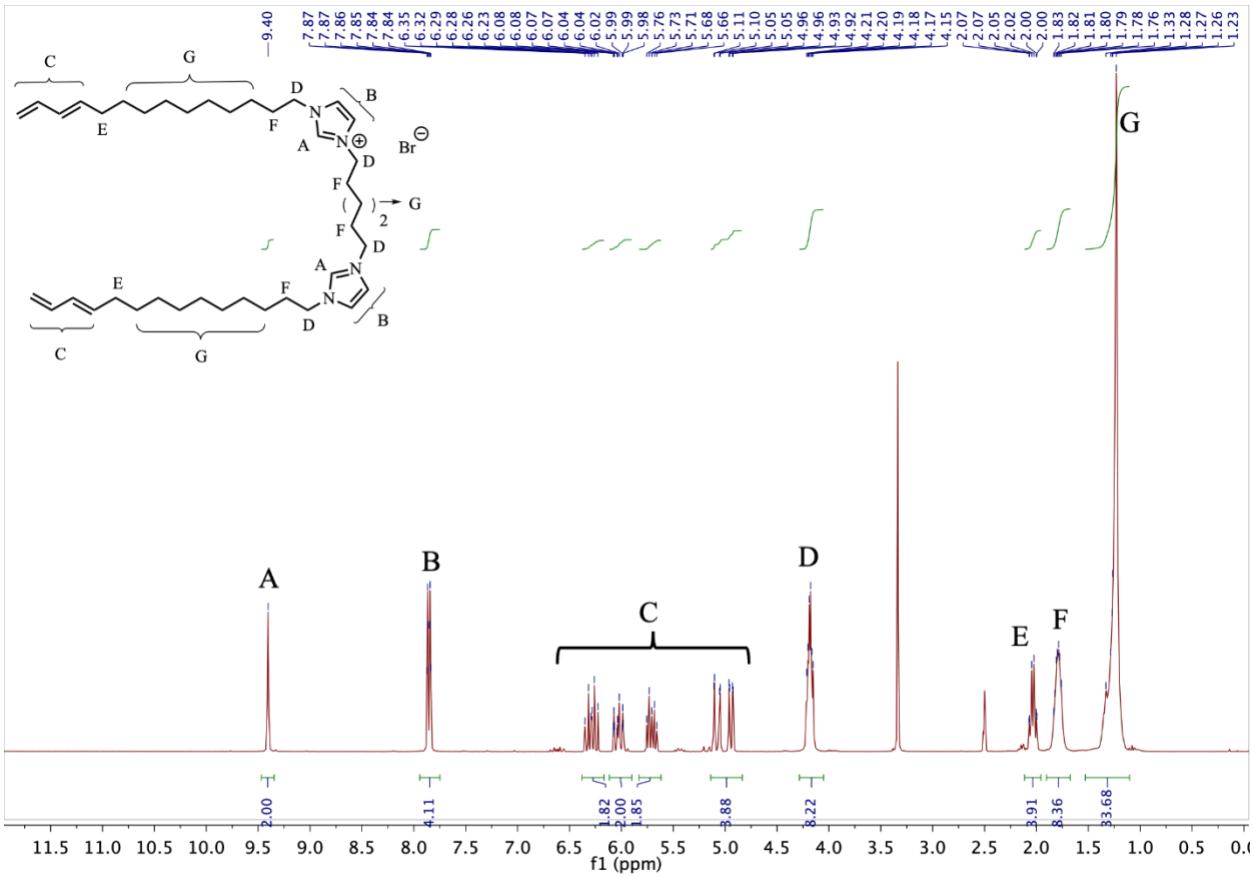

Figure 3.10 ^{1}H NMR spectrum of **[6H, 14T]** in DMSO-d_6.

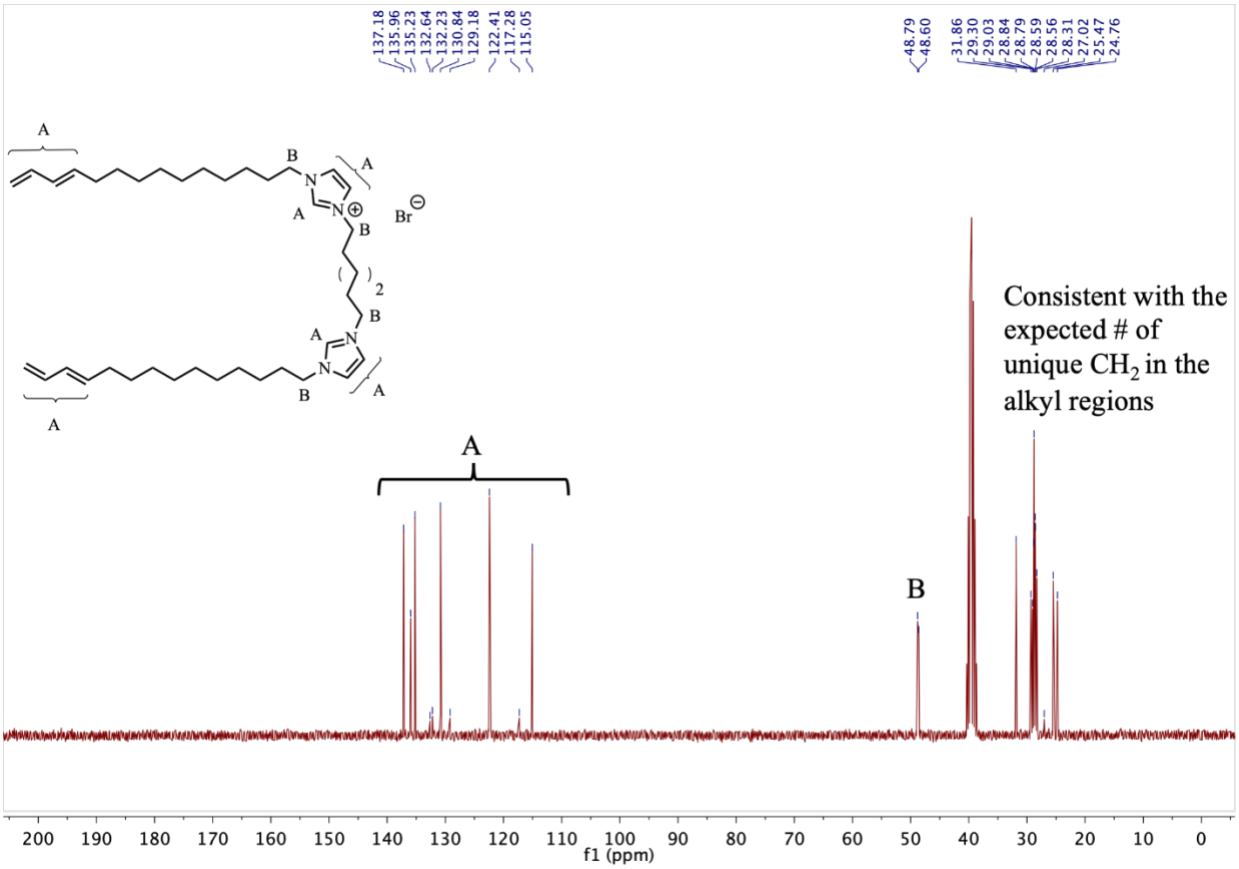

Figure 3.11 ^{13}C NMR spectrum of **[6H, 14T]** in DMSO-d_6.

3.5.3 Qualitative Screening of LLC Phase Behavior and Potential Q Phase Formation with Different Solvents Using the PLM-Based Penetration Scan Technique.[1c]

To quickly and qualitatively determine the LLC phase behavior of homologs of monomer **4a** (see Table 3.2) with a specific added solvent, the PLM penetration scan technique was employed.[1c] This technique is a solvent-amphiphile gradient assay using PLM that quickly (i.e., in minutes) determines qualitatively what phases can be formed by a certain amphiphile and solvent pair at a specific temperature. This technique was performed by taking the solid monomer and pressing it between a microscope slide and a cover slip. The sample was then placed on the

PLM thermal stage and annealed to its melting temperature or up to 90 °C, whichever came first. The sample was then slowly cooled back down to room temperature. A small amount (<30 μL) of the chosen solvent was added to the edge of the cover slip, and the solvent was drawn via capillary action into contact with the solid monomer, creating a concentration gradient. The specimen was then heated to 95 °C at a rate of 5 °C/min on the PLM programmable hot/cold stage, and its optical texture under crossed polarizers as a function of temperature was recorded via digital image capture. The differences in optical texture were used to determine the potential LLC phases formed. Since Q phases are black (i.e., isotropic) under PLM and are typically found between birefringent lamellar (L) and hexagonal (H) phases, a dark isotropic band between two birefringent LLC phases indicates a potential Q phase.[1c] The seven homologs of monomer **4a** were evaluated in this fashion with glycerol and with water.

Table 3.2 Summary of the preliminary qualitative Q-phase formation behavior of monomer **4a** and its seven homologs studied in this work when mixed with glycerol and water in the 25–95 °C temperature range, as determined via PLM-based solvent-penetration scan screening studies. These results do not guarantee the presence of a Q phase without more detailed phase diagram analysis of carefully prepared mixtures via full PLM phase elucidation supported by PXRD confirmation.

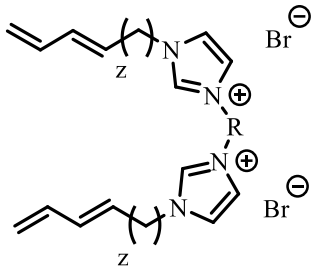

			Potential Q Phase via Penetration Scan		Potential Q Phase Onset Temperature (°C)	
Monomer	**R**	**z**	**Glycerol**	**Water**	**Glycerol**	**Water**
4a	6	14	Yes	Yes	65	68
[5H, 18T]	5	14	Yes	Yes	46	58
[7H, 18T]	7	14	Yes	Yes	51	48
[9H, 18T]	9	14	Yes	Yes	40	43
[4H, 14T]	4	10	No	Yes	(not applicable)	40
[5H, 14T]	5	10	Yes	Yes	25	26
[6H, 14T]	6	10	No	Yes	(not applicable)	29
[7H, 14T]	7	10	No	No	(not applicable)	(not applicable)

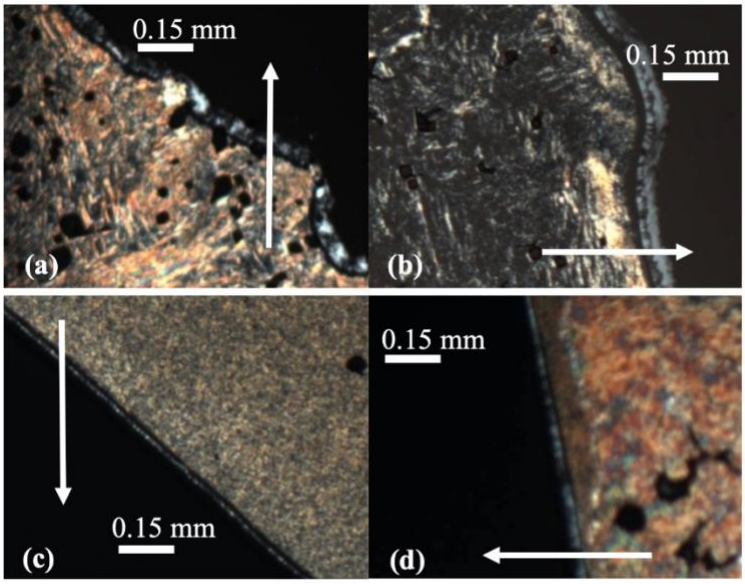

Figure 3.12 Representative PLM images (magnification: 50x) of glycerol penetration scans of homologs **[5H, 18T]**, **[7H, 18T]**, **[9H, 18T]**, and **[5H, 14T]**: (a) potential Q-phase formation for **[5H, 18T]** at 46 °C; (b) potential Q-phase formation for **[7H, 18T]** at 51 °C; (c) potential Q-phase formation for **[9H, 18T]** at 40 °C; (d) potential Q-phase formation for **[5H, 14T]** at 25 °C. The black (pseudo-isotropic region) between two bright, anisotropic LLC regions is indicative of the presence of a potential Q phase.[1c] The arrows in the PLM images point in the direction of increasing glycerol concentration.

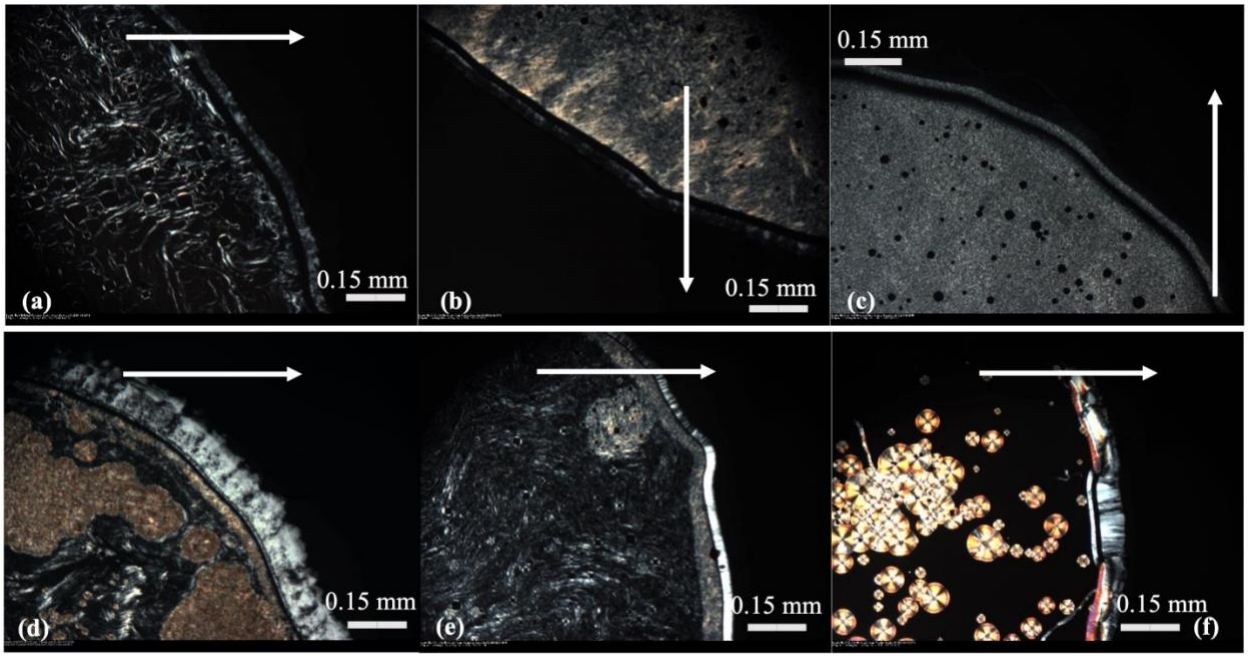

Figure 3.13 Representative PLM images (magnification: 50x) of water penetration scans of homologs **[5H, 18T]**, **[7H, 18T]**, **[9H, 18T]**, **[4H, 14T]**, **[5H, 14T]**, and **[6H, 14T]**: (a) potential Q-phase formation for **[5H, 18T]** at 58 °C; (b) potential Q-phase formation for **[7H, 18T]** at 48 °C; (c) potential Q-phase formation for **[9H, 18T]** at 43 °C; (d) potential Q-phase formation for **[4H, 14T]** at 40 °C; (e) potential Q phase formation for monomer **[5H, 14T]** at 26 °C; (f) potential Q-phase formation for monomer **[6H, 14T]** at 29 °C. The black (pseudo-isotropic region) between two bright, anisotropic LLC regions is indicative of the presence of a potential Q phase.[1c] The arrows in the PLM images point in the direction of increasing water concentration.

3.5.4 Preparation of LLC Samples, Determination of LLC Phase Behavior, and Elucidation of Partial Phase Diagrams

LLC samples of specific composition were made by adding an appropriate amount of monomer and solvent to custom-made glass vials. A small amount (i.e., 1 wt% of the total mixture mass) of radical photo-initiator, 2-hydroxy-2-methylpropiophenone (HMP), was added if required; and the vials were sealed with Parafilm™. LLC samples were mixed by alternately hand-mixing and centrifuging (2800 rpm) until completely homogeneous. It should be noted that the LLC samples are sensitive to water loss or gain, depending on the solvent system. Special attention was

taken to keep the samples sealed as much as possible during sample mixing and transferring to minimize composition drift.

For samples prepared with water, LLC samples of specific composition were prepared by adding the desired mass of monomer to tared, custom-made glass vials placed on a microbalance, followed by the addition of an appropriate mass of solvent via pipette. HMP photo-initiator (1 wt% of the total mixture mass) was then added if required. The vials were sealed with Parafilm™ and centrifuged at 2800 rpm. The samples were then alternately hand-mixed and centrifuged (2800 rpm) until homogeneous by visual inspection (ca. three cycles of hand-mixing and centrifuging).

For samples prepared with glycerol, LLC samples of specific composition were prepared by adding the desired mass of solvent to tared, custom-made glass vials placed on a microbalance, followed by the addition of an appropriate mass of monomer via spatula. HMP photo-initiator (1 wt% of the total mixture mass) was then added if required. The vials were sealed with Parafilm™ and centrifuged at 2800 rpm. The samples were then alternately hand-mixed and centrifuged (2800) until homogeneous by visual inspection (ca. three cycles of hand-mixing and centrifuging).

The composition and temperature ranges of the LLC phases formed by the mixtures described above were determined using variable-temperature PLM. Specimens of various mixture compositions were prepared and then pressed between a microscope slide and microscope cover-slip to help minimize composition drift from ambient atmospheric water uptake or solvent evaporation. This assembly was then placed on the PLM programmable hot/cold stage and annealed past its isotropic temperature or up to 90 °C (whichever came first). The sample was slowly cooled and allowed to come back to its room-temperature phase. The sample was then heated to 95 °C at a rate of 5 °C/min, and its optical textures as a function of temperature were

recorded via digital image capture. Images were captured at 50x magnification. Changes in optical texture were used to determine changes in the LLC phase of the mixture.

Whenever possible, the identity of each observed phase was confirmed using ambient-temperature PXRD by analyzing a bulk film of a composition point in each distinct phase region (as elucidated by PLM analysis) that was photo-cross-linked to permanently trap the phase microstructure. A sample with radical photo-initiator was placed between Mylar sheets with a thickness-appropriate spacer (to minimize composition drift due to ambient atmospheric water uptake or solvent evaporation), annealed at the appropriate temperature for 15 min on a programmable hot plate, and then photopolymerized for 1 h while held at that temperature. Room-temperature PXRD spectra of the resulting cross-linked bulk film samples were taken in the open air using a custom-made, clamped sandwich-type film holder with a central open window. The clamped polymer film was then positioned such that the open face of the film was directly in the path of the X-ray beam, between the beam source and the detector (i.e., through-film transmission mode). The *d*-spacing pattern of the PXRD peaks was used to quantitatively identify the type of LLC phase formed at the specified composition and temperature used to form the cross-linked sample, so long as more than one PXRD peak are present to clearly index an LLC phase with a specific geometry.[1]

Variable-temperature PXRD (VT-PXRD) analysis of unpolymerized LLC mixtures for phase identification was used to check non-Q-phase boundaries or if ambient-temperature PXRD analysis of a bulk film was not informative enough to draw conclusions on the phase. An LLC mixture of a composition point in each distinct region was formulated as described above but without photo-initiator. The (LLC monomer + glycerol or water) mixture was then spread onto the top of an open-face, circular aluminum pan (approx. sample dimensions: 10 mm in diameter x

0.2 mm thick), which was placed on a custom-built programmable sample heating stage for the PXRD instrument. The top of the unpolymerized mixture in the sample pan was then covered with a piece of Mylar sheet to minimize composition drift due to ambient water uptake or solvent evaporation, and allowed to equilibrate for 5–10 min. The Mylar-film-covered, unpolymerized sample then was analyzed via PXRD using a conventional powder diffraction geometry while held at the desired temperature for 1–2 h. The *d*-spacing pattern of the PXRD peaks was used to quantitatively identify the type of LLC phase formed, so long as more than one diffraction peak are present to clearly index an LLC phase with a specific geometry.[1] In the event that both ambient-temperature PXRD and VT-PXRD were not informative enough to draw conclusions on a suspected Q-phase region, bulk film samples were sent off to our collaborators at the University of Pennsylvania for SAXS analysis.

For illustration purposes, a schematic representation of the various phase regions and the different LLC phases typically observed in amphiphile-water mixtures is shown in Figure 3.8 below, as an ideal, symmetric phase diagram.[4] However, not all amphiphile-solvent systems show all of these phases, and actual phase diagrams are generally not this symmetric in nature.

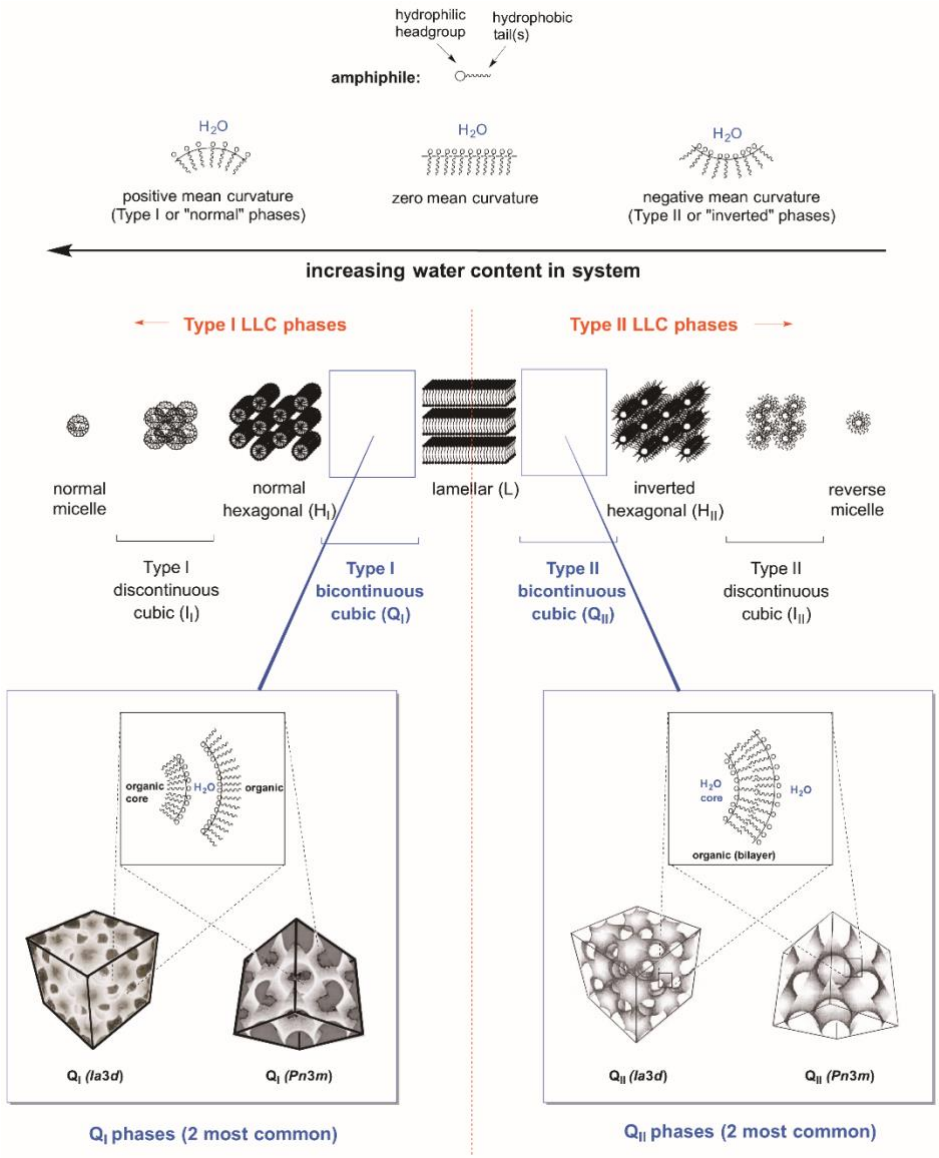

Figure 3.14 Schematic representation of the most common LLC phases formed by amphiphiles in water in an ideal phase progression, with a focus on the Q phases. Partially reproduced from Ref. 4. Copyright Nature Publishing Group, 2012.

Assignment of LLC phase regions was done by first assessing if the PLM optical texture was black or birefringent. If the optical texture was black and the corresponding PXRD spectrum had a broad/weak principal peak or effectively no sharp diffraction peaks (see Figure 3.19a), then the phase region was categorized as an amorphous isotropic phase (Iso) (i.e., an amorphous melt

or unordered collection of normal or reverse spherical micelles). If the PLM optical texture was birefringent and the PXRD spectrum exhibited a single or multiple sharp diffraction peaks, then the observed phase was assigned as hexagonal (H), lamellar (L), or an unidentified anisotropic phase or mixture of unidentified anisotropic phases (Unidentified anisotropic phase(s)). H phases have PXRD peaks with a *d*-spacing pattern of 1: 1/√3: 1/√4: 1/√7: 1/√9…etc. with respect to the principal peak.[1,8] L phases have PXRD peaks with a *d*-spacing pattern of 1: 1/2: 1/3: 1/4: 1/5…etc. with respect to the principal peak.[1,8] If the PXRD spectrum showed *d*-spacings that could not be clearly indexed to those of H or L phases but the presence of a sharp peak or peaks suggested some degree of order, then the phase was assigned as an Unidentified anisotropic phase(s), depending if there were multiple sharp peaks in the spectrum.

Assignment of Q phase regions and discontinuous cubic phase regions (I) was done by confirming the presence of a black, pseudo-isotropic optical texture (as a consequence of their cubic symmetry) and differences in their PXRD order. I phases typically have PXRD peaks with a *d*-spacing ratio of 1: 1/√3: 1/√8: 1/√11: 1/√12…etch, with respect to the principal peak.[27,28] They are also typically optically transparent because of their cubic symmetry but are not very viscous because they consist of cubic-packed individual normal or reverse micelles with minimal contact with each other.[1,27] In contrast, Q phases typically exhibit PXRD peaks with a *d*-spacing pattern of 1/√6: 1/√8: 1/√20: 1/√22…etc. with respect to the principal peak.[1,8] Q phases also are optically transparent but are typically very viscous in nature because they consist of 3D-interpenetrating hydrophobic and hydrophilic channel systems.[1] Based on these features and differences in features, phase regions that have black PLM optical textures and PXRD order could be differentiated into Q and I phases. Weakly ordered Q phases were identified as Q phases that followed the appropriate *d*-spacing pattern but had a broader than usual principal peak.

In addition, each H, Q, or I phase with the specific geometry/symmetry described above can also be sub-classified in terms of whether the phase curves around the hydrophobic domains (i.e., normal / Type I) or around the hydrophilic domains (inverted / Type II).[1] To unequivocally determine whether an observed LLC phase is Type I or Type II, an L phase needs to be present in the phase diagram as a central reference point that has no preferred net curvature towards either the hydrophilic or hydrophobic domains. Then, LLC phases on the solvent-excessive side of the L phase can be assigned as Type I (normal), and those on the solvent-deficient side can be assigned as Type II (inverted).[1] Unfortunately, only one of the homologs studied in this work showed an L phase in its partial phase diagram (i.e., **[7H, 18T]** with water); none of the homologs that showed a Q phase (i.e., **[5H, 18T]**, **[9H, 18T]**, **[5H, 14T]**, and **[6H, 14T]**) also exhibited an identifiable L phase for a clear Type I vs. Type II phase assignment.

Using the combined PLM and PXRD data and criteria above, partial phase diagrams of the seven monomer **4a** homologs were created as a function of system composition and temperature.

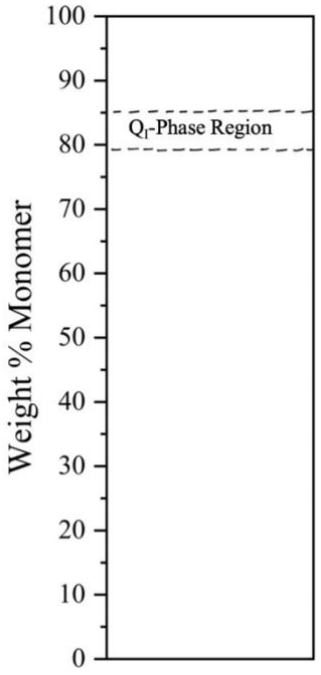

Figure 3.15 Partial phase diagram of monomer **4a** in glycerol at 65 °C constructed from data published in Ref. 17.

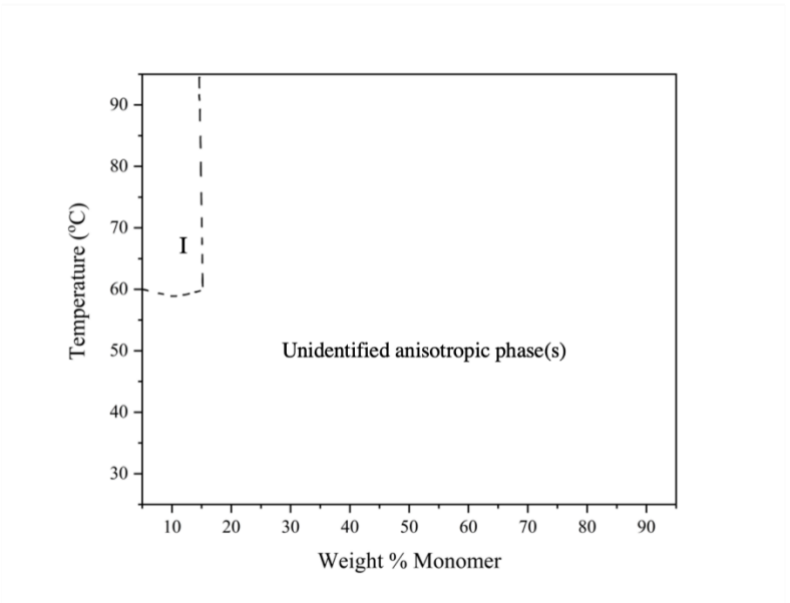

Figure 3.16 Partial phase diagram of **[5H, 18T]** with water. I = discontinuous cubic phase.

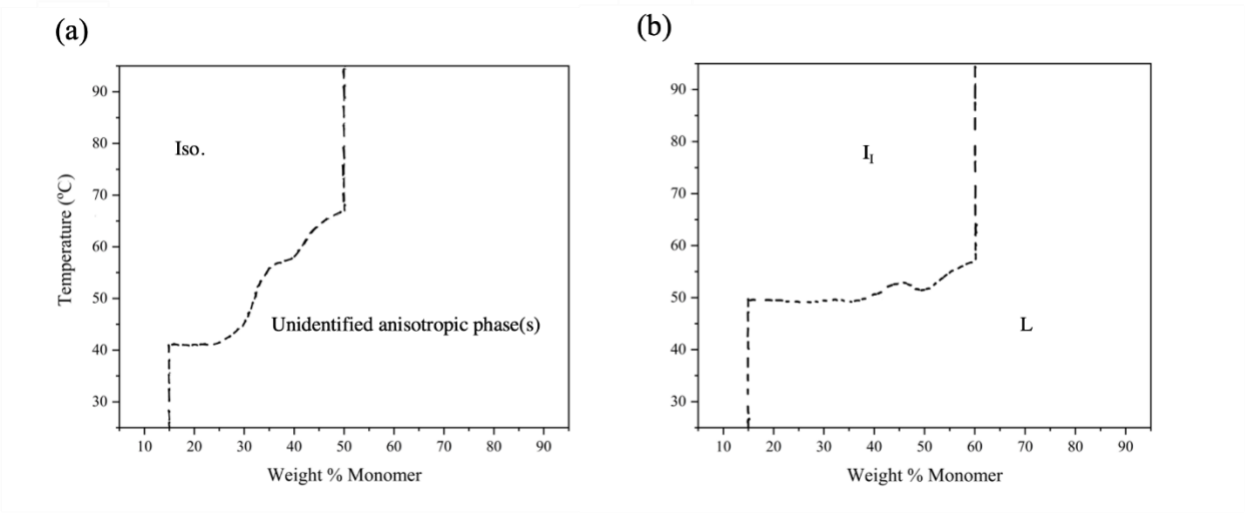

Figure 3.17 Partial phase diagrams of **[7H, 18T]** with (a) glycerol and (b) with water. Iso. = amorphous isotropic phase; L = lamellar phase; I_I = Type I discontinuous cubic phase.

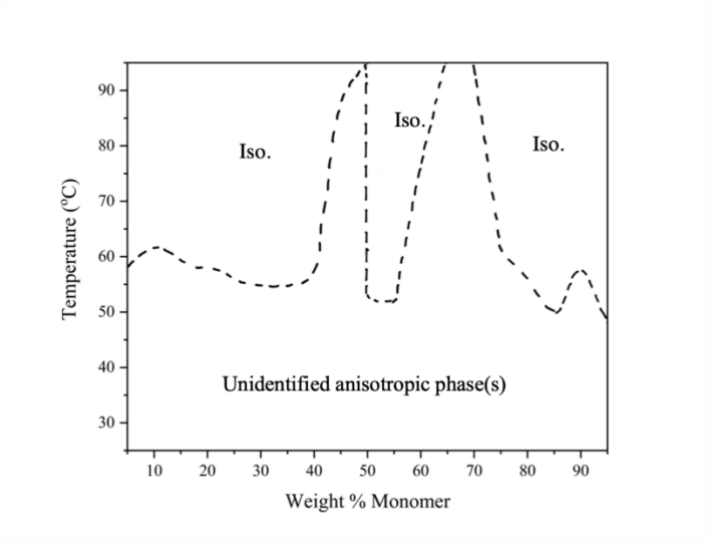

Figure 3.18 Partial phase diagram of **[9H, 18T]** in water. Iso. = amorphous isotropic phase.

Note: Although **[4H, 14T]** in water demonstrated the <u>potential</u> to form a Q phase by preliminary PLM penetration scan analysis (Table 3.2), more detailed and careful PLM composition and temperature analysis revealed that **[4H, 14T]** with water did not display any completely black optical textures. The lack of a black optical texture during the detailed PLM

analysis implied that a pure Q phase was not present and thus did not require further study via PXRD analysis. We hypothesize that the lack of a Q phase for **[4H, 14T]** may potentially be related to the spacer length between the ionic headgroups. With shortening spacer lengths, the ionic interactions between the headgroups may become more pronounced and could affect the ability of a gemini amphiphile to form a particular phase.[19,20]

For samples that demonstrated the potential to form a Q phase during preliminary PLM-based solvent-penetration scan screening (Table 3.2) and exhibited optically black regions during detailed PLM composition and temperature analysis, PXRD analysis was utilized to quantitatively confirm if the optically black region was a Q phase or a different type of optically isotropic phase. In some cases (e.g., **[5H, 14T]** in glycerol), rapid PLM penetration scan screening analysis suggested the potential for Q phase formation (Table 3.2), whereas the full PLM characterization followed by PXRD analysis of carefully prepared sample mixtures did not reveal formation of an actual Q phase (see Table 3.1).

3.5.4.1 Example PXRD Profiles and PLM Images Used for Phase Assignments in the Elucidation of the Partial Phase Diagrams

Note: It was not possible to identify whether the Q phases formed were *Ia3d* or *Pn3m* from the PXRD spectra in the main manuscript and ESI. Neither our PXRD instrument (nor our collaborator's SAXS instrument) was able to resolve enough diffraction peaks in the Q-phase samples to unequivocally identify an *Ia3d* or a *Pn3m* unit cell.

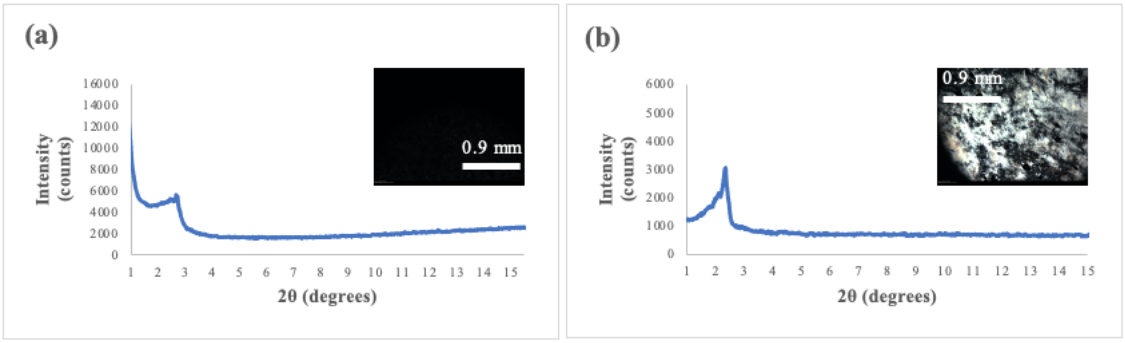

Figure 3.19 Example PXRD profiles and PLM images used to assign disordered isotropic (Iso) phases and unidentified anisotropic phase(s) in the partial phase diagram: (a) VT-PXRD profile and PLM image of a disordered isotropic (Iso) phase obtained from an unpolymerized mixture of 30/70 (w/w) **[5H, 18T]**/glycerol at 65 °C. (b) PXRD profile and PLM image of an unidentified anisotropic phase or mixture of phases obtained from a mixture of 70/30 (w/w) **[5H, 18T]**/glycerol at 65 °C.

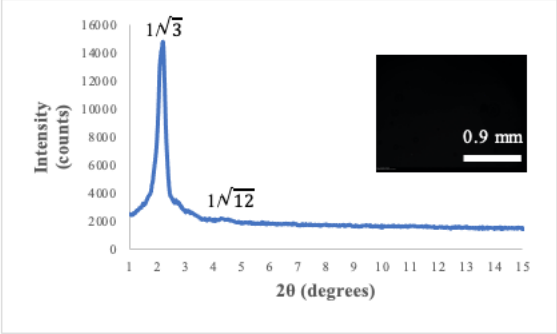

Figure 3.20 VT-PXRD profile and PLM image of the discontinuous cubic (I) phase formed by an unpolymerized mixture of 10/90 (w/w) **[5H, 18T]**/water at 62 °C. The PXRD *d*-spacings and black optical texture are consistent with an I phase.[27,28]

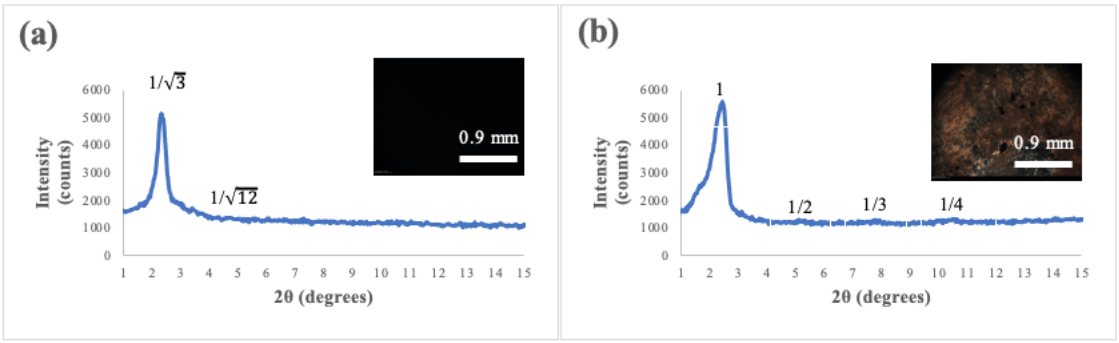

Figure 3.21 Example VT-PXRD and PLM images of some LLC phases formed by **[7H, 18T]** with water: (a) VT-PXRD profile and PLM image of a discontinuous cubic (I) phase formed by an unpolymerized mixture of 40/60 (w/w) **[7H, 18T]**/water at 80 °C. The PXRD peak *d*-spacings and black optical texture are consistent with an I phase.[27,28] (b) VT-PXRD profile and PLM image of the lamellar (L) phase formed by an unpolymerized mixture of 75/25 (w/w) **[7H, 18T]**/water at 50 °C. The equally spaced 2θ peaks and birefringent optical texture are indicative of an L phase.[1,8]

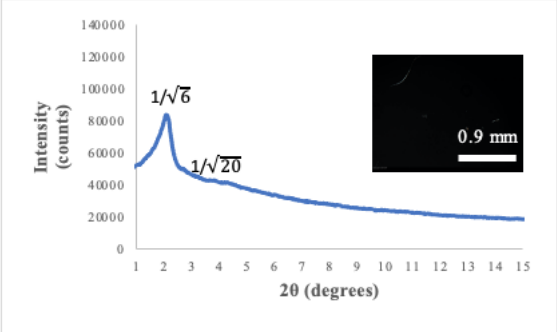

Figure 3.22 PXRD profile and PLM image of a bulk cross-linked Q-phase film formed by photopolymerization of a mixture of 74/25/1 (w/w/w) **[9H,18T]**/glycerol/HMP at 55 °C.

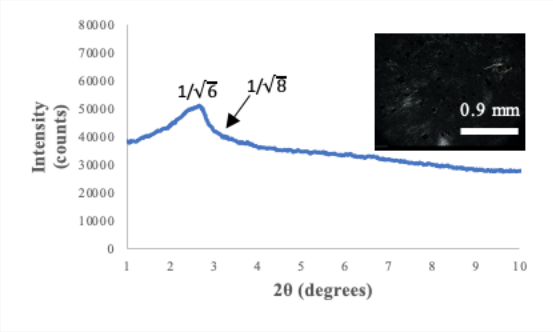

Figure 3.23 PXRD profile and PLM image of a bulk cross-linked Q-phase film formed by photopolymerization of a mixture of 89/10/1 (w/w/w) **[5H, 14T]**/water/HMP at 55 °C.

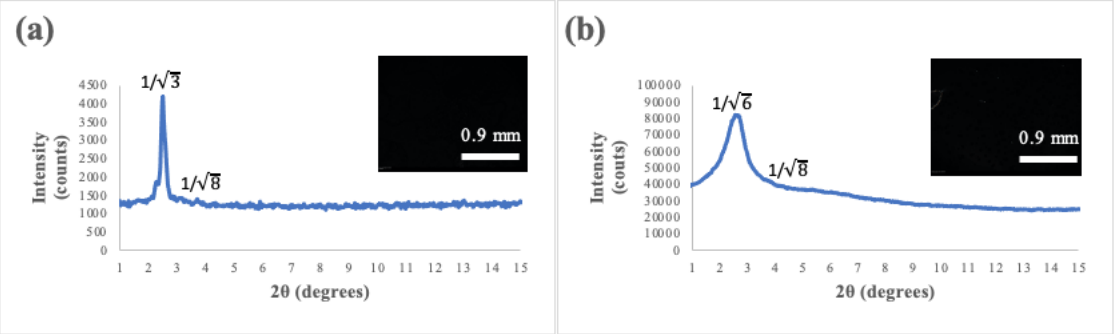

Figure 3.24 Example PXRD and PLM images of some LLC phases formed by **[6H, 14T]** with water: (a) VT-PXRD profile and PLM image of a discontinuous cubic (I) phase formed by an unpolymerized mixture of 10/90 (w/w) **[6H, 14T]**/water at 30 °C. The PXRD peak *d*-spacings and black optical texture are consistent with an I phase.[27,28] (b) PXRD profile and PLM image of a bulk cross-linked Q-phase film formed by photopolymerization of a mixture of 84/15/1 (w/w/w) **[6H, 14T]**/water/HMP at 55 °C.

3.5.4.2 Single-run SAXS Profile Obtained to Confirm the Q-phase Structure of a Cross-linked Sample Analyzed by PXRD

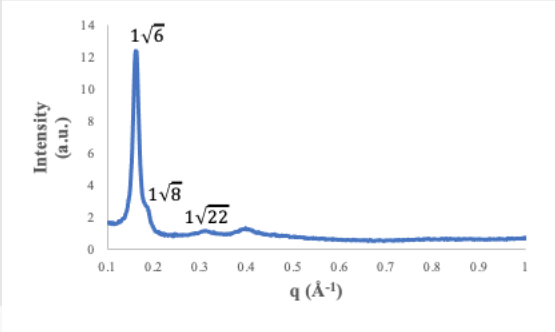

Figure 3.25 SAXS profile of a bulk cross-linked Q-phase film prepared from a mixture of **[5H, 18T]**/glycerol/HMP (79/29/1 (w/w/w)) for which a PXRD spectrum was shown in Figure 3.3 in Section 3.4. The signal at ca. 0.4 $Å^{-1}$ is from Kapton film support.

As can be seen from the SAXS spectrum above, the primary peak and shoulder appear to be in a ratio of 1/√6: 1/√8. Both the PXRD and SAXS profiles for this sample are consistent with one another and indicative of a Q phase. However, given the lack of other discernable peaks, we refrain from assigning a specific space group to the Q phase of this sample (and similarly to the other observed Q phases in this chapter).

3.5.5 Example FT-IR Data for Determining the Extent of Polymerization in Photo-cross-linked Q-phase Samples

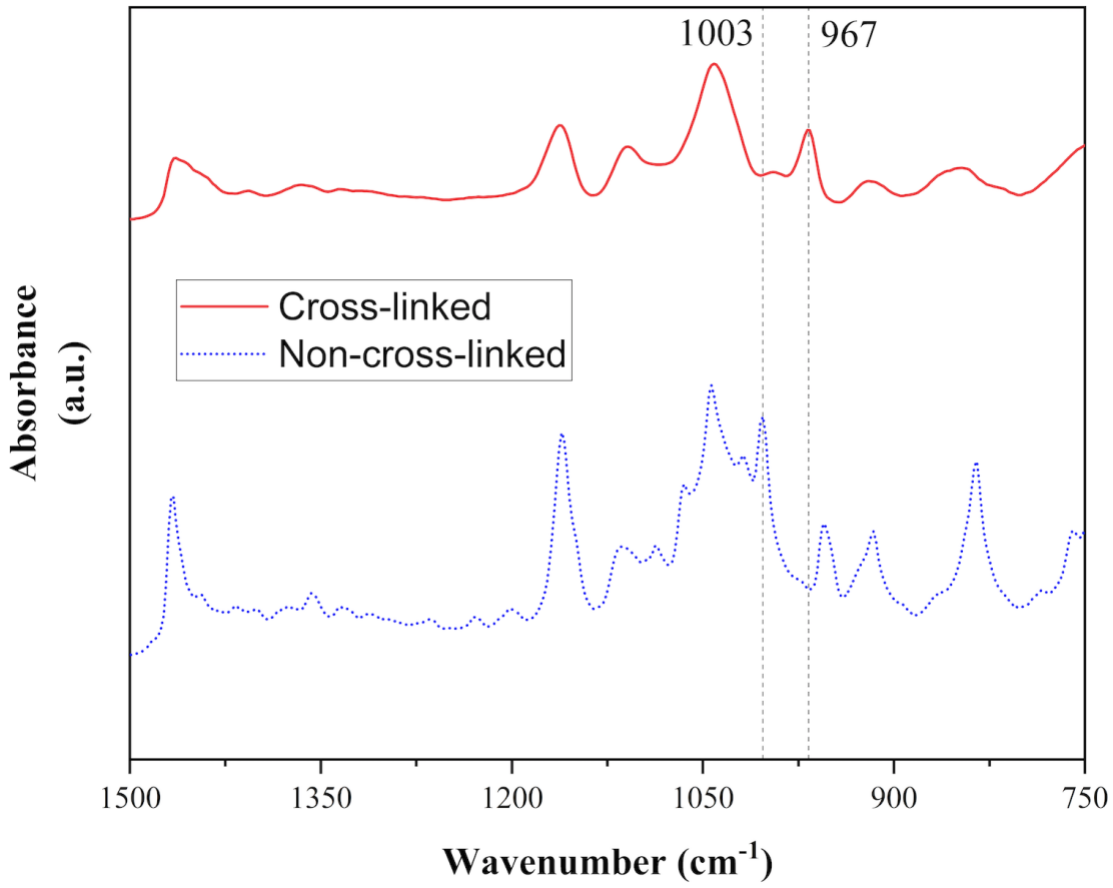

Figure 3.26 Representative FT-IR spectra of a bulk Q-phase film of a mixture of 79/20/1 (w/w/w) **[5H, 18T]**/glycerol/HMP pre- and post-photopolymerization. The disappearance of the band at 1003 cm^{-1} (corresponding to the -C–H out-of-plane wag of CH_2=CH_2) and the appearance of a new band at 967 cm^{-1} (corresponding to CH=CH *trans* units) signify essentially complete 1,3-diene group conversion.[9]

3.5.6 Acknowledgments

P.L., M. I. R., S. S. D., K. E. M. and D. L. G. thank the Joint Science and Technology Office for Chemical Biological Defense (JSTO CBD) for funding under CB10872. O. Q. I. thanks the NSF (grant DMR-1720530) for partial funding of the instrument used for SAXS analysis at the University of Pennsylvania.

3.6 References

1. For general reviews on LLC phases, see: (a) Tate, M. W.; Eikenberry, E. F.; Turner, D. C.; Shyamsunder, E.; Gruner, S. M. Nonbilayer phases of membrane lipids. *Chem. Phys. Lipids* **1991**, *57*, 147–164. (b) Seddon, J. M. Structure of the inverted hexagonal (H_{II}) phase, and non-lamellar phase transitions of lipids. *Biochim. Biophys. Acta* **1990**, *1031*, 1–69. (c) Tiddy, G. J. T. Surfactant-water liquid crystal phases. *Phys. Rep.* **1980**, *57*, 1–46.
2. For reviews of cross-linked LLC phases and their applications, see: (a) Gin, D. L.; Pecinovsky, C. S.; Bara, J. E.; Kerr, R. L. Functional Lyotropic Liquid Crystal Materials. *Struct. Bonding* **2007**, *128*, 181–222. (b) Gin, D. L.; Lu, X.; Nemade, P. R.; Pecinovsky, C. S.; Xu, Y.; Zhou, M. Recent Advances in the Design of Polymerizable Lyotropic Liquid-Crystal Assemblies for Heterogeneous Catalysis and Selective Separations. *Adv. Funct. Mater*. **2006**, *16*, 865–878. (c) Mueller, A.; O'Brien, D. F. Supramolecular Materials via Polymerization of Mesophases of Hydrated Amphiphiles. *Chem. Rev*. **2002**, *102*, 727–758. (d) Gin, D. L.; Gu, W.; Pindzola, B. A.; Zhou, W. Polymerized Lyotropic Liquid Crystal Assemblies for Materials Applications. *Acc. Chem Res.* **2001**, *34*, 973–980.

3. For a recent review of LC-based materials for ion transport, see: Kato, T.; Yoshio, M.; Ichikawa, T.; Soberats, B.; Ohno, H.; Funahashi, M. Transport of ions and electrons in nanostructured liquid crystals. *Nat. Rev. Mater.* **2017**, *2*, 1–20.
4. For a review of nanoporous polymers based on Q LLC phases and their applications, see: Wiesenauer, B. R.; Gin, D. L. Nanoporous Polymer Materials Based on Self-Organized, Bicontinuous Cubic Lyotropic Liquid Crystal Assemblies and Their Applications. *Polym. J.* **2012** *44*, 461–468.
5. Israelachivili, J. N. Intermolecular and Surface Forces with Applications to Colloidal and Biological Systems. Academic: London; **1985**, 249.
6. Fontell, K. Cubic phases in surfactant and surfactant-like lipid systems. *Colloid Polym. Sci.* **1990**, *268*, 264–285.
7. Kobayashi, T.; Li, Y.-X.; Ono, A.; Zeng, X.-B.; Ichikawa, T. Gyroid structured aqua-sheets with sub-nanometer thickness enabling 3D fast proton relay conduction. *Chem. Sci.* **2019**, *10*, 6245–6253.
8. Pindzola, B. A.; Jin, J.; Gin, D. L. Cross-Linked Normal Hexagonal and Bicontinuous Cubic Assemblies via Polymerizable Gemini Amphiphiles. *J. Am. Chem. Soc.* **2003**, *125*, 2940–2949.
9. Zhou, M.; Nemade, P. R.; Lu, X.; Zeng, X.; Hatakeyama, E. S.; Noble, R. D.; Gin, D. L. New Type of Membrane Material for Water Desalination Based on a Cross-linked Bicontinuous Cubic Lyotropic Liquid Crystal Assembly. *J. Am. Chem. Soc.* **2007**, *129*, 9574–9575.
10. Hatakeyama, E. S.; Wiesenauer, B. R.; Gabriel, C. J.; Noble, R. D.; Gin, D. L. Nanoporous, bicontinuous Cubic Lyotropic Liquid Crystal Networks via Polymerizable Gemini Ammonium Surfactants. *Chem. Mater.* **2010**, *22*, 4525–4527.

11. Kerr, R. L.; Miller, S. A.; Shoemaker, R. K.; Elliott, B. J.; Gin, D. L. New Type of Li Ion Conductor with 3D Interconnected Nanochannels via Polymerization of a Liquid Organic Electrolyte-Filled Lyotropic Liquid-Crystal Assembly. *J. Am. Chem. Soc*. **2009**, *131*, 15972–15973.
12. Lee, Y. S.; Yang, J. Z.; Sisson, T. M.; Frankel, D. A.; Gleeson, J. T.; Aksay, E.; Keller, S. L.; Gruner, S. M.; O'Brien, D. F. Polymerization of nonlamellar lipid assemblies. *J. Am. Chem. Soc.* **1995**, *117*, 5573–5578.
13. Takeuchi, H.; Ichikawa, T.; Yoshio, M.; Kato, T.; Ohno, H. Induction of bicontinuous cubic liquid-crystalline assemblies for polymerizable amphiphiles via tailor-made design of ionic liquids. *Chem. Commun.* **2016**, *52*, 13861–13864.
14. McGrath, K. M.; Drummond, C. J. Polymerisation of liquid crystalline phases in binary surfactant/water systems. Part 1. Allyldodecyldimethylammonium bromide and allyldidodecylmethylammonium bromide. *Colloid Polym. Sci.* **1996**, 274, 316–333.
15. Yang, D.; O'Brien, D. F.; Marder, S. R. Polymerized bicontinuous cubic nanoparticles (cubosome) from a reactive monoacylglycerol. *J. Am. Chem. Soc.* **2002**, *124*, 13388–13389.
16. Gao, X.; Lu, F.; Liu, Y.; Sun, N.; Zheng, L. The facile construction of an anion exchange membrane with 3D interconnected ionic nano-channels. *Chem. Commun.* **2017**, *53*, 767–770.
17. Carter, B. M.; Wiesenauer, B. R.; Hatakeyama, E. S.; Barton, J. L.; Noble, R. D.; Gin, D.L. Glycerol-based Bicontinuous Cubic Lyotropic Liquid Crystal Monomer System for the Fabrication of Thin-film Membranes with Uniform Nanopores. *Chem. Mater*. **2012**, *24*, 4005–4007.

18. Dwulet, G. E.; Dischinger, S. M.; McGrath, M. J.; Basalla, A. J.; Malecha, J. J.; Noble, R. D.; Gin, D. L. Breathable, Polydopamine-Coated Nanoporous Membranes That Selectively Reject Nerve and Blister Agent Simulant Vapors. *Ind. Eng. Chem. Res.* **2019**, *58*, 21890–21893.
19. Perroni, D. V.; Baez-Cotto, C. M.; Sorenson, G. P.; Mahanthappa, M. K. Linker Length-Dependent Control of Gemini Surfactant Aqueous Lyotropic Gyroid Phase Stability. *J. Phys. Chem. Lett.* **2015**, *6*, 993–998.
20. Mantha, S.; McDaniel, J. G.; Perroni, D. V.; Mahanthappa, M. K.; Yethiraj, A. Electrostatic Interactions Govern "Odd/Even" Effects in Water-Induced Gemini Surfactant Self-Assembly. *J. Phys. Chem. B* **2017**, *121*, 565–576.
21. Jennings, J.; Green, B.; Mann, T. J.; Guymon, C. A.; Mahanthappa, M. K. Nanoporous Polymer Networks Templated by Gemini Surfactant Lyotropic Liquid Crystals. *Chem. Mater.* **2018**, *30*, 185–196.
22. Hoag, B. P.; Gin, D. L. Cross-Linkable Liquid Crystal Monomers Containing Hydrocarbon 1,3-Diene Tail Systems. *Macromolecules* **2000**, *33*, 8549–8558.
23. Pindzola, B. A.; Hoag, B. P.; Gin, D. L. Polymerization of a Phosphonium Diene Amphiphile in the Regular Hexagonal Phase with Retention of Mesostructure. *J. Am. Chem. Soc.* **2001**, *123*, 4617–4618.
24. Sharma, S.; Tandon, M.; Lown, J. W. Design and Synthesis of Novel Thiazole-Containing Cross-Linked Polyamides Related to the Antiviral Antibiotic Distamycin. *J. Org. Chem.* **2000**, *65*, 1102–1107.
25. Bara, J. E.; Hatakeyama, E. S.; Wiesenauer, B. R.; Zeng, X.; Noble, R. D.; Gin, D. L. Thermotropic Liquid Crystal Behavior of Gemini Imidazolium-based Ionic Amphiphiles. *Liq. Cryst.* **2010**, *37*, 1587–1599.

26. Merino, I.; Thompson, J. D.; Millard, C. B.; Schmidt, J. J.; Pang, Y.-P. Bis-imidazole as molecular probes for peripheral sites of the zinc endopeptidase of botulinum neurotoxin serotype A. *Bioorg. Med. Chem.* **2006**, *14*, 3583–3591.
27. Seddon, J. M.; Robins, J.; Gulik-Krzywicki, T.; Delacroix, H. Inverse micellar phases of phospholipids and glycolipids. *Phys. Chem. Chem. Phys.* **2000**, *2*, 4485–4493.
28. Huang, Y.; Gui, S. Factors affecting the structure of lyotropic liquid crystals and the correlation between structure and drug diffusion. *RSC Adv.* **2018**, *8*, 6978 – 6987.
29. Blanton, T. N.; Huang, T. C.; Toraya, H.; Hubbard, C. R.; Robie, S. B.; Louër, D.; Göbel, H. E.; Will, G.; Gilles, R.; Raftery, T. JCPDS–International Centre for Diffraction Data round robin study of silver behenate. A possible low-angle X-ray diffraction calibration standard. *Powd. Diffract.* **1995**, *10*, 91–95.
30. Piancatelli, G. *Encyclopedia of Reagents for Organic Synthesis*, **2001**, 1, John Wiley & Son Ltd., United Kingdom.

Chapter 4: Stable Cross-linked Lyotropic Gyroid Mesophases from Single-head/Single-tail Cross-linkable Monomers

In the collaborative work detailed in this chapter (and associated joint publication), I designed, synthesized, and structurally characterized the new cross-linkable monomer; and worked on studies related to selective initiation of polymerizable groups.

(A modified version of this chapter was originally published as: Imran, O. Q.; Li, P.; Kim, N. K.; Gin, D. L.; Osuji, C. O. "Stable cross-linked lyotropic gyroid mesophases from single-head/single-tail cross-linkable monomers." *Chem. Commun.* **2021**, *57*, 10931–10934.)

4.1 Abstract

A single-head/single-tail surfactant with a polymerizable group at each end is presented as a new simplified motif for intrinsically cross-linkable, gyroid-phase lyotropic mesogens. The resulting nanoporous polymer networks exhibit excellent structural stability in various solvents and are capable of molecular size discrimination.

4.2 Introduction

Cross-linked lyotropic liquid crystal (LLC) phases are nanoporous polymer materials that have been found to be useful for a number of applications, including templated synthesis, heterogeneous catalysis, molecular size filtration, and enhanced ion transport.[1] They are prepared by the direct polymerization of cross-linkable amphiphile (i.e., surfactant) monomer systems that form periodic, phase-separated assemblies around a polar liquid such as water, with retention of the phase nanostructure. This process yields stabilized polymer structures with uniform, ca. 1 nm-

wide pores in which the hydrophilic headgroups of the monomers are localized at the pore walls, thereby providing the ability to control or functionalize the pore environment for specific applications.

Although LLC phases with different pore architectures are known, bicontinuous (Q) phases are highly desired for the preparation of LLC networks for selective molecular transport and uptake applications.[2] This is because Q phases possess 3D-interconnected pore systems with overall cubic symmetry, and thus do not require alignment for good transport performance or internal access as with lower-dimensionality LLC phases.[2]

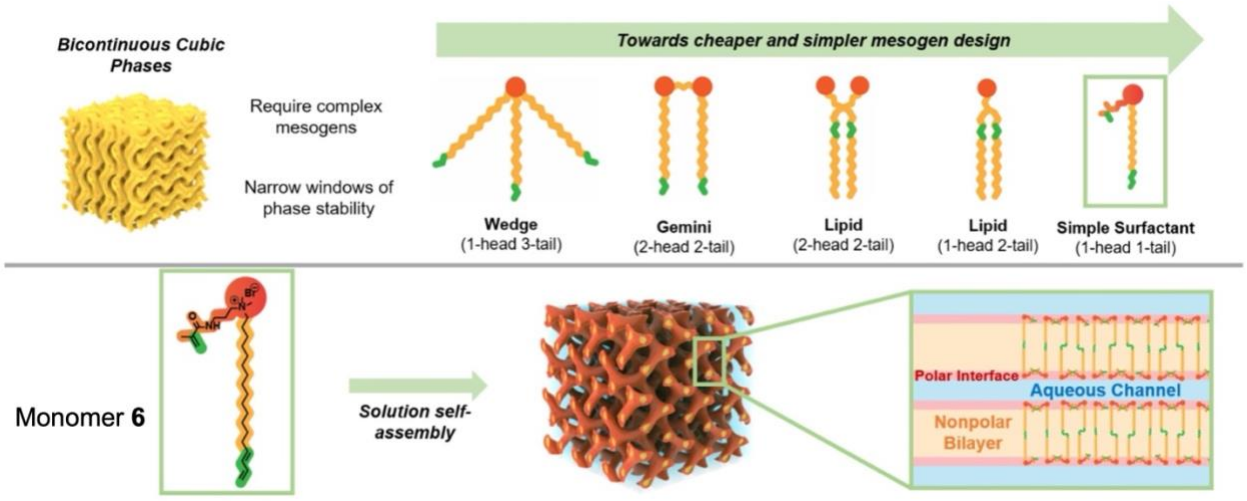

Figure 4.1 Schematic of double-gyroid Q phase and typical cross-linkable LLC monomer architectures that form Q phases (red/orange = hydrophilic headgroup, yellow = hydrophobic tail, green = polymerizable group). The novel design of monomer **6**, as well as its self-assembly into a nanoporous, normal-type, double-gyroid network, are also depicted.

Unfortunately, only a very limited number of Q-phase LLC monomer platforms have been reported that can be cross-linked with phase retention. Most of these are based on fairly elaborate monomer motifs (Figure 4.1) that typically require costly and/or complicated syntheses, making them difficult to scale-up or structurally modify. In particular, cross-linkable Q-phase monomer

systems based on reactive lipid-like (i.e., single-head/two-tail),[3,4] gemini (i.e., bridged two-headgroup/two-tail),[5-12] taper-shaped (i.e., single-head/three-tail),[13,14] and two-headed-lipid (i.e., two-head/two-tail)[15] amphiphiles have been reported that can be radically polymerized with retention of phase architecture. Many of these were intrinsically cross-linkable single-monomer systems,[5-9,13,14] while others were cross-linkable mixtures of LLC monomers[3,4] or blends with co-monomers or organic additives.[8,10-12,15] The hydrophilic headgroups in these systems ranged from uncharged[4] to ionic[5-8,13,14] and zwitterionic,[3,9-11] but they all had a polymerizable group in their hydrophobic tails as a common feature.

A small number of structurally simpler, single-head/single-tail amphiphilic monomers have also been reported to form Q phases.[16-20] Based on a 'simple surfactant' motif, they are easier to synthesize[18,19] and chemically modify. These amphiphiles were uncharged,[17] ionic,[16,18] or zwitterionic[19] in nature, but they all contained only one radically polymerizable group per molecule (either near the headgroup[16,18] or in the tail[17]) and thus required cross-linking co-monomers to form stable Q networks.[17,19] In some cases, blending with an organic additive was also required to form a Q phase.[18]

Herein, we present an intrinsically cross-linkable, single-head/single-tail amphiphile (**6**) that can be radically polymerized as a single-monomer system to generate highly stable Q-phase networks (Figure 4.1). This new monomer motif carries a polymerizable methacrylamide group near the ionic headgroup and a polymerizable diene group in the hydrophobic tail, allowing it to be radically cross-linked without added co-monomers/cross-linkers, unlike prior Q-phase single-head/single-tail monomer systems. Monomer **6** is readily synthesized from a commercial polymerizable amine and forms a gyroid-type Q phase with water at room temperature as confirmed by polarized optical microscopy (POM) and small-angle X-ray scattering (SAXS).

After photopolymerization, the resulting polymeric materials exhibit excellent retention of the mesophase nanostructure. Notably, the nanostructure is stable with respect to long-term exposure to acidic and alkaline aqueous conditions, as well as to organic solvents of interest. Preliminary studies also show that the different polymerizable groups in the hydrophilic vs. hydrophobic regions of the monomer can be initiated non-selectively, or with some selectivity for one reactive group, via the use of different aqueous solutions for Q phase formation or radical photo-initiators with different solubilities. Experiments involving uptake of charged solutes and pressure-driven filtration of a neutral solute indicate the Q-phase networks have a pore diameter in the range of 1.5 nm, which agrees well with the calculated pore size based on SAXS data.

4.3 Results and Discussion

Monomer **6** was synthesized by reacting *N*-[3-(dimethylamino)propyl]methacrylamide with 18-bromooctadeca-1,3-diene[21] in CH_3CN at 70 °C in a one-step S_N2 reaction. After purification, the structure and purity of **6** were verified by ^1H NMR, ^{13}C NMR, FT-IR, and elemental analyses (see Section 4.6 for more details). The design of **6** was based on a non-cross-linkable cationic monomer with a single methacrylamide group near the head that was recently found to form a Q phase with aqueous solutions (i.e., monomer **7**, see Figure 4.3 and Figure 4.5). By replacing the long alkyl tail on this monomer with a polymerizable diene tail, an intrinsically cross-linkable analog was generated. The diene tail system was chosen because of its similarity in shape and hydrophobic character to regular *n*-alkyl tails compared to tail systems with bulkier or more polar polymerizable moieties,[21,22] thereby increasing the probability of retaining the Q phase of the original monomer. Although not the focus here, **6** can also form other LLC mesophases such as lamellar and hexagonal (see Figure 4.10).

A Q phase was obtained a room temperature at a composition of 87.5/11.5/1.0 (w/w/w) monomer **6**/water/2,2-dimethoxy-2-phenylacetophenone (DMPA, a radical photo-initiator). Polymer films with retention of the Q-phase structure (typical thicknesses between 50–150 μm) were obtained by photo-cross-linking the monomer mesophase with UV light under N_2 purge for ca. 3 h (Figure 4.2a–c). The monomer mesophase and the resulting polymer films exhibited dark POM images, consistent with the optically isotropic character of Q phases (Figure 4.2d and e). SAXS spectra of the mesophase and polymer films (Figure 4.2f) display the characteristic peaks associated with the (211) and (220) planes of the double-gyroid structure (space group *Ia3d*), appearing at normalized scattering vector ratios of 1: √(4/3) (i.e., √8: √6). From these *q*-values, the lattice parameter *a* of the monomer mesophase and polymerized films was calculated to be 8.74 and 8.55 nm, respectively. No evidence of lattice swelling (i.e., changes in *a*) was seen in dry vs. wet polymer films (see Figure 4.11).

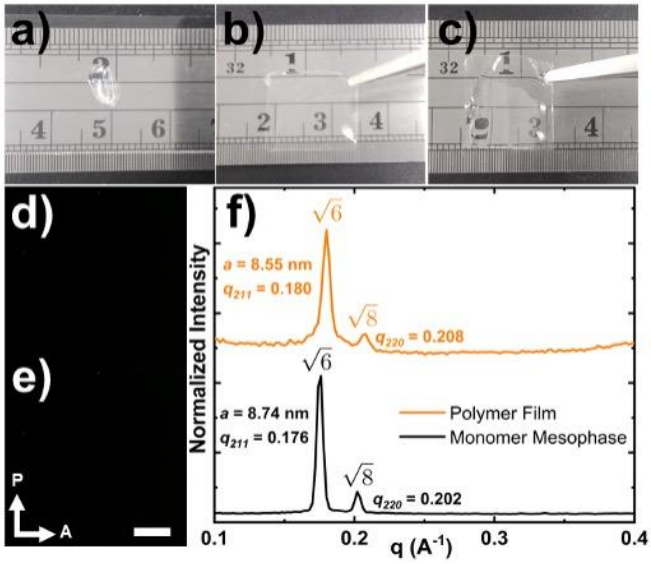

Figure 4.2 Photos of (a) monomer gyroid mesophase of **6**, water, and photo-initiator, (b) dry polymer film of cross-linked gyroid phase of **6**, and (c) same polymer film of **6** after 30-min water immersion; POM micrographs of (d) monomer mesophase and (e) dry polymer film observed between crossed polarizers (scale bar = 100 μm); (f) SAXS spectra of gyroid mesophase and polymer of **6**.

The fabrication of a Q-phase nanostructure polymer film does not always guarantee stability of the Q-phase microstructure at the molecular level. The novel structural motif of **6**, with two-chain addition polymerizable groups at opposite ends of the molecule, affords significantly more Q-phase stability when polymerized than monomer **7**, a similar Q-phase-forming monomer with only one polymerizable group (see Figure 4.5) or the combination of **7** and an added bifunctional cross-linker (1,10-decanediol dimethacrylate (DDMA)). Figure 4.3a compares the SAXS spectra of Q-phase films made form **7** (left), **7** + DMMA (center), and **6** (right) after water immersion for ca. 24 h. In both cases involving **7**, the SAXS spectra show successful retention of the gyroid phase upon cross-linking. However, after water immersion of these gyroid polymer films, SAXS analysis shows disappearance or significant diminishment of the (220) (i.e., $\sqrt{8}$) peak, along with an increase in the primary peak width and a larger value of the lattice parameter, consistent with partial or total loss of the double-gyroid nanostructure. Speculatively, this loss of structure upon water exposure may originate from a combination of leaching of monomers that were not cross-linked to the polymer matrix, and molecular scale rearrangement for monomers linked only at a single site. In contrast, the polymer film made from intrinsically cross-linkable **6** exhibited negligible difference in the SAXS traces of as-made and water-immersed films, indicating the Q-phase structure is much more robustly locked-in at the molecular level. Further testing of the polymer films confirmed that the gyroid polymers are stable to at least 210 °C, and that they maintain their structure even after prolonged immersion in aqueous acid and base, as well as in organic and halogenated organic solvents (Figure 4.3b). While there are prior reports of cross-linked gyroid structures produced from LLC monomers with more-complex structures, we are unaware of LLC-derived nanostructured polymers with the remarkable thermal and chemical/solvent stability demonstrated here.

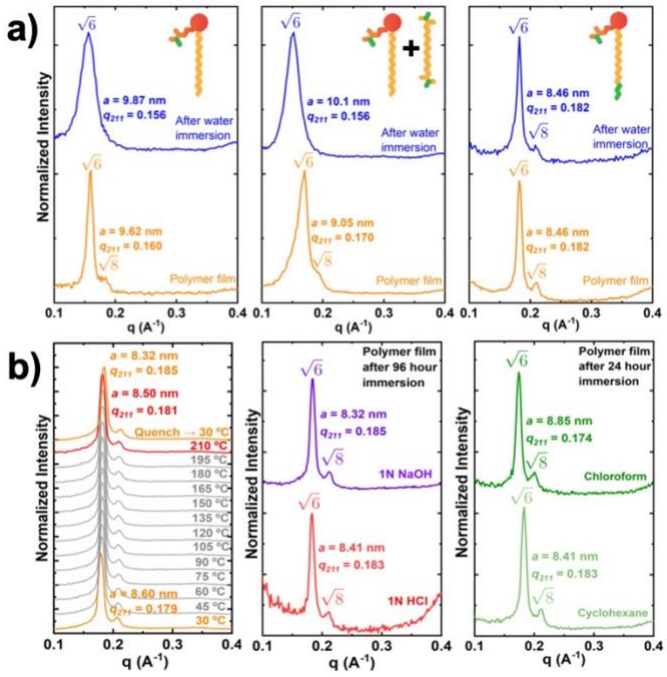

Figure 4.3 (a) SAXS plots comparing degree of retention of double-gyroid phase after 24 h of water immersion for polymer films made from (left) monomer **7**; (center) monomer **7** + DDMA cross-linker; and (right) monomer **6**; (b) SAXS plots summarizing the stability of the gyroid nanostructure in monomer **6**-derived polymers at elevated temperatures, as well as in various solvent environments (at room temperature).

Preliminary studies also show that the methacrylamide and diene groups in the hydrophilic vs. hydrophobic regions of the monomer can be initiated non-selectively, or with some degree of selectivity for one reactive group over the other, with retention of the Q phase. When water was used to form the Q phase of **6** with DMPA as a hydrophobic photo-initiator, FTIR analysis showed that the diene tails were largely polymerized, but only a small fraction of the methacrylamide groups near the head was converted. However, when a 0.1 M aq. LiCl solution was used to form the phase instead of pure water, near-quantitative conversion of both the head and tail polymerizable groups was achieved (see Figure 4.12). We hypothesize that the increase in ionic strength of the aqueous phase may reduce the ability of the methacrylamides near the water/organic interface to reside near the aqueous phase, forcing them to reside more in the hydrophobic regions

where the hydrophobic DMPA initiator and diene tails are located for more effective initiation of both groups. The use of 2-hydroxy-4'-(2-hydroxyethoxy)-2-methylpropiophenone (HHMP), an uncharged, water-soluble radical photo-initiator, showed complete conversion of both the head and tail polymerizable groups (see Figure 4.13), probably because its organic yet hydrophilic nature allows it to partition between the aqueous and organic domains and initiate groups residing in or near both. In each case, SAXS confirmed Q phase retention after partial or near-complete photopolymerization. Prior work on selective initiation of LLC monomers with two different polymerizable groups has only been demonstrated in vesicles for proof-of-concept;[23-25] selective polymerization in a Q phase is unprecedented. Although completely independent initiation of one reactive group over the other has not been achieved yet, these results suggest that it may be possible to alter the mechanical properties of gyroid films of **6** by controlling the degree of polymerization in the head vs. tail regions.

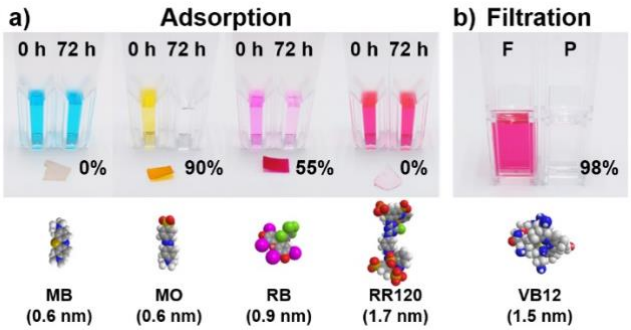

Figure 4.4 (a) Photos of uptake of charged dyes into gyroid polymers. The rejection of small cationic Methylene Blue (MB) and large anionic Reactive Red 120 (RR120) indicates the polymers have charge- and size-based selectivity; (b) Photo of Vitamin B12 (VB12) feed (f) and permeate (P) obtained from pressure-driven filtration of gyroid polymer membranes of **6**, indicating 98% solute rejection.

The nanoporous nature of the cross-linked gyroid polymers makes them natural candidates for applications such as selective adsorption and nanofiltration (NF). These applications have been pursued in other polymerized LLC phases,[26] but the gyroid morphology is particularly valued because of its continuous percolated nature. The solvent and thermal stability of the cross-linked gyroid polymers suggest that they could be of interest in a wide range of selective transport applications, ranging from aqueous and organic solvent NF, to ion-conduction in ambient or harsh environments such as Li-ion batteries or alkaline fuel cells, respectively. The theoretical pore size of the aqueous channels separating the intertwined gyroid structures was estimated as ca. 1.5 nm, and the specific surface area is estimated to be in the ca. 500 m^2g^{-1} range (see the Supporting Information).[27] Figure 4.4a summarizes the uptake of various charged dyes into Q-phase polymer films of **1** immersed into aq. Dye solutions for 72 h. The solute sizes reported are the calculated geometric mean dimensions of the molecules (see Table 4.4). The films showed no discernible uptake of Methylene Blue (MB), which at 0.6 nm is smaller than the estimated aqueous channel size. This rejection is likely due to electrostatic repulsion between this cationic dye and the positively charged interior surfaces of the membrane pores due to the quaternary ammonium group on the surfactant. In contrast, the negatively charged dyes Methyl Orange (MO, 0.6 nm), Rose Bengal (RB, 0.9 nm), and Reactive Red 120 (RR120, 1.7 nm) were taken up by the polymer, but the amount adsorbed is a function of the size of the dye. The lack of discernable uptake of RR120 suggests that it is simply too large to enter the channels of the polymer, despite favorable electrostatic attraction. These results qualitatively indicate that the pore size lies between 0.9 and 1.7 nm. This range of length scales is of interest for NF as recently demonstrated in other LLC-based membranes.[26] Figure 4.4b shows a photograph of the permeate from the pressure-driven filtration of a Vitamin B12 feed (VB12, 1.5 nm) through a ca. 100 μm-thick gyroid polymer film

of **6**. The near-complete (98%) rejection of uncharged VB12 suggests that the effective pore size is in the range of 1.5 nm, consistent with our estimate from SAXS data. The thickness-normalized permeability of the films is roughly 0.1 L m^{-2} h^{-1} bar^{-1} μm, which agrees well with previously reported NF data on cross-linked Q-phase films with similar pore sizes but made using more-complex LLC monomers.[15,28]

4.4 Conclusions

In conclusion, we report a novel intrinsically cross-linkable surfactant motif for the formation of nanoporous polymer films with a gyroid Q-phase structure. SAXS and POM data confirm the successful retention of the gyroid nanostructure in the cross-linked polymer films. The benefit of having two polymerizable groups (as opposed to one) on the monomer is illustrated by comparing the long-term stability of the polymeric films upon water exposure. The solvent and temperature stabilities of the fabricated gyroid films indicate their potential for separation applications. Lastly, the transport performance (i.e., effective pore size based on rejection, and water permeability) of the fabricated gyroid films has been studied. The results motivate further study and optimization of this platform based on a novel LLC monomer motif.

4.5 Supporting Information

4.5.1 Materials

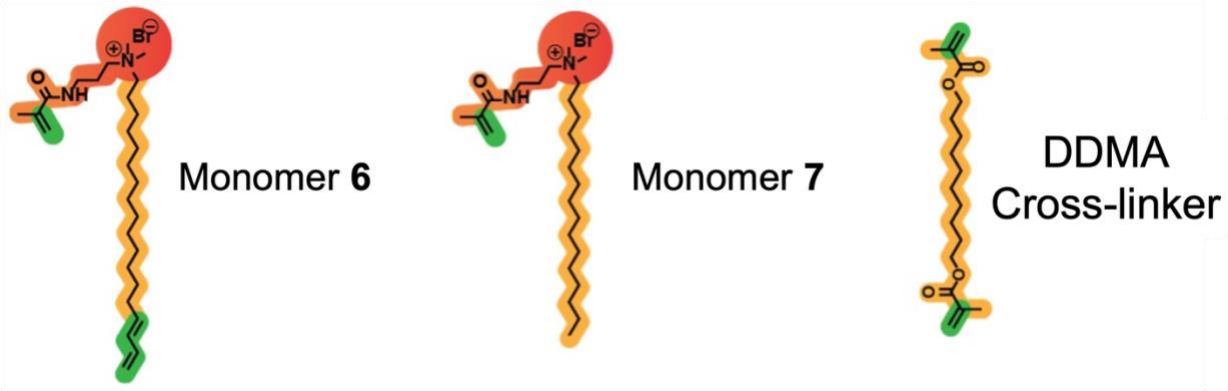

Figure 4.5 Chemical structures of intrinsically cross-linkable monomer **6**, non-cross-linkable monomer **7**, and commercial cross-linker DDMA. (red/orange = hydrophilic headgroup region, yellow = hydrophobic tail region, green = polymerizable site).

4.5.1.1 Synthesis of Monomers **6** and **7**

Chromium (VI) oxide, pyridine, *tert*-butyl lithium (1.6 M in pentane), hydrogen bromide (48% wt. % in H_2O), borane-tetrahydrofuran complex solution (1.0 M in THF), *ω*-pentadecalactone (98%), sulfuric acid, triethanolamine (98%), *N*-3-(dimethylamino)propylmethacrylamide, 3,5-di-*tert*-4-butylhydroxytoluene, 1-bromohexadecane (97%), and Florisil® (<200 mesh) were purchased from the Sigma-Aldrich Chemical Co. and used as received unless otherwise specified. *N,N,N',N',*-tetramethylethylenediamine (98%), allyltrimethylsilane (98%), and 2-isopropoxy-4,4,5,5-tetramethyl-1,3,2-dioxaborolane (98%) were purchased from TCI America and used as received unless otherwise specified. Aluminum oxide (neutral, act. I, 50–200 μm) and silica gel (normal-phase, 200 x 400 mesh) were purchased from Sorbent Technologies. Sodium chloride, magnesium sulfate, Celite™ 545, and hydrochloric acid (all ACS Reagents) were purchased from Fisher Scientific and used as received. All solvents

were obtained from the Sigma-Aldrich Chemical Co. and were purified/dehydrated via vacuum distillation and then de-gassed by repeated freeze-pump-thaw cycles and stored under Ar. All chemical syntheses were carried out under a dry Ar atmosphere using standard Schlenk line techniques unless otherwise noted.

NMR spectra were obtained using a Bruker Avance-III 300 NMR spectrometer (300 MHz for ^{1}H, 75 MHz for ^{13}C). Chemical shifts are reported in parts per million relative to the solvent residual signal (DMSO, δ_H = 2.50 ppm, δ_C = 39.52 ppm). FTIR spectra (neat) were recorded on an Agilent Cary 630 FTIR instrument single-reflection horizontal ATR accessory with diamond crystal. Elemental analysis was performed by Galbraith Laboratories, Inc.

(*E*)-*N*-(3-methacrylamidopropyl)-*N*,*N*-dimethyloctadeca-15,17-dien-1-aminium bromide (monomer 6)

18-Bromooctadeca-1,3-diene (1.9979 g, 6.0658 mmol, 1.0000 equiv.), *N*-3-(dimethylamino)propylmethacrylamide (1.1360 g, 6.6725 mmol, 1.1000 equiv.), and 3–4 crystals of 3,5-di-*tert*-4-butylhydroxytoluene were dissolved in CH_3CN (10 mL) in a 25-mL amber Schlenk flask equipped with a stir bar. The solution was stirred at 70 °C for 24 h in the dark. The contents of the Schlenk flask were cooled to room temperature and precipitated from Et_2O (200 mL) in a Dry Ice-acetone bath. The precipitate was filtered immediately and dried in vacuo to give monomer **6** as a white solid (2.6491 g, 87%). ^{1}H NMR (300 MHz, DMSO-d_6): δ 8.06 (t, J = 5.8 Hz, 1H), 6.39 – 6.20 (m, 1H), 6.11 – 5.96 (m, 1H), 5.79 – 5.65 (m, 1H), 5.67 (td, J = 1.9, 1.0 Hz, 1H), 5.35 (p, J = 1.6 Hz, 1H), 5.15 – 5.02 (m, 1H), 5.01 – 4.90 (m, 1H), 3.21 (ddd, J = 19.0, 9.7, 4.9 Hz, 6H), 2.99 (s, 6H), 2.03 (q, 1H), 1.86 (dd, J = 1.6, 0.9 Hz, 3H), 1.61 (s, 2H), 1.39 – 1.21 (m, 14H). ^{13}C NMR (75 MHz, DMSO-d_6): δ 167.64, 139.75, 137.23, 135.29, 130.88, 119.28,

115.09, 62.84, 50.12, 35.91, 31.88, 29.03, 28.99, 28.85, 28.60, 28.58, 28.52, 25.77, 22.46, 21.65, 18.61. FTIR (neat): 3224, 2917, 2849, 1656, 1619, 1531, 1467, 1318, 1212, 1070, 1003, 912, 803, 720 cm^{-1}. Calc. for $C_{27}H_{51}BrN_2O$: C, 64.91; H, 10.29; N, 5.61. Found: C, 64.68; H, 10.26; N, 5.58.

***N*-(3-Methacrylamidopropyl)-*N*,*N*-dimethylhexadecan-1-aminium bromide (monomer 7)**

1-Bromohexadecane (8.0000 g, 0.026200 mol, 1.0000 equiv.), *N*-3-(dimethylamino)propylmethacrylamide (4.9068 g, 0.028821 mol, 1.1000 equiv.), and 3–4 crystals of 3,5-di-*tert*-4-butylhydroxytoluene were dissolved in CH_3CN (50 mL) in a 100-mL amber Schlenk flask equipped with a stir bar. The solution was stirred at 70 °C for 24 h in the dark. The contents of the Schlenk flask were cooled to room temperature and precipitated from Et_2O (200 mL) in a Dry Ice-acetone bath. The precipitate was filtered immediately and dried in vacuo to give monomer **7** as a white solid (8.1317 g, 65%). ^{1}H NMR (300 MHz, DMSO-d_6): δ 8.08 (t, J = 5.8 Hz, 1H), 5.69 (dd, J = 1.5, 0.9 Hz, 1H), 5.35 (p, J = 1.5 Hz, 1H), 3.30 – 3.11 (m, 6H), 3.00 (s, 6H), 1.93 – 1.76 (m, 4H), 1.61 (s, 2H), 1.24 (s, 25H), 0.91 – 0.80 (m, 3H). ^{13}C NMR (75 MHz, DMSO-d_6): δ 167.63, 139.73, 119.27, 62.84, 60.90, 50.12, 35.90, 31.27, 29.04, 28.99, 28.94, 28.80, 28.69, 28.51, 25.77, 22.43, 22.08, 21.64, 18.60, 13.94. FTIR (neat): 3378, 2918, 2850, 1653, 1612, 1530, 1465, 1334, 1220, 1067, 970, 923, 809, 720 cm^{-1}. Calc. for $C_{25}H_{51}BrN_2O$: C, 63.14; H, 10.81; N, 5.89. Calc. for $C_{25}H_{53}BrN_2O_2 \cdot H_2O$: C, 60.83; H, 10.82; N, 5.68. Found: C, 60.82; H, 10.75; N, 5.68.

Note: The newly synthesized monomers are hygroscopic, ionic organic compounds that are difficult to dry completely and usually do not combust well. However, their obtained elemental

analysis values are within the accepted ±0.4% tolerance range for C, H, and N to be considered pure when the presence of associated water molecules is accounted for.[5]

4.5.1.2 Other Mesophase Additives

All other materials used in mesophase formulation were purchased from Sigma-Aldrich and used as received. A cross-linker additive 1,10-decanediol dimethacrylate (DDMA) was used for a mesophase formulation discussed in Figure 4.3a. The standard radical photo-initiator used for most mesophase formulations was 2,2-dimethoxy-2-phenylacetophenone (DMPA); but for the data discussed in Figure 4.13 2-hydroxy-4'-(2-hydroxyethoxy)-2-methylpropiophenone (HHMP) was the photo-initiator used for mesophase formulation instead of DMPA.

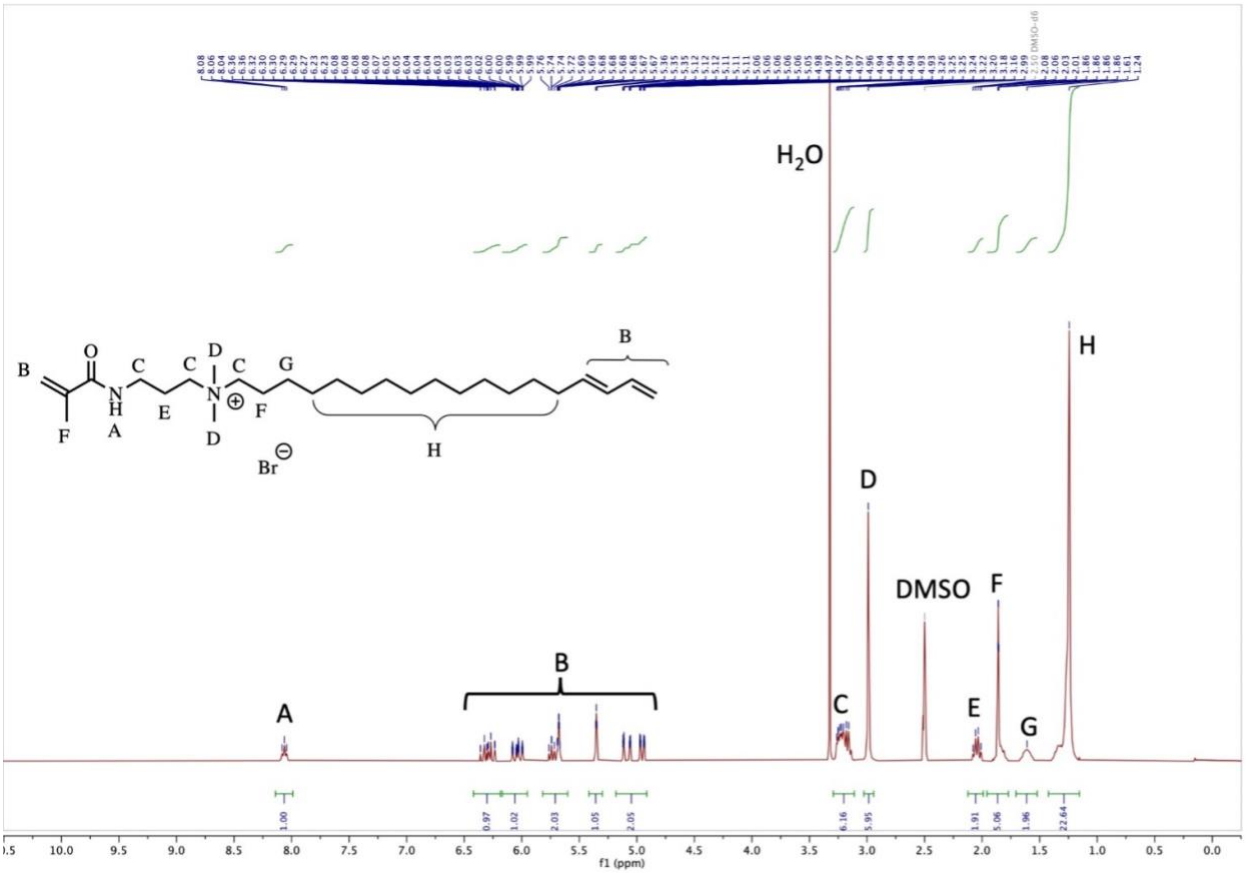

Figure 4.6 ^{1}H NMR spectrum of monomer **6** in DMSO-d_6.

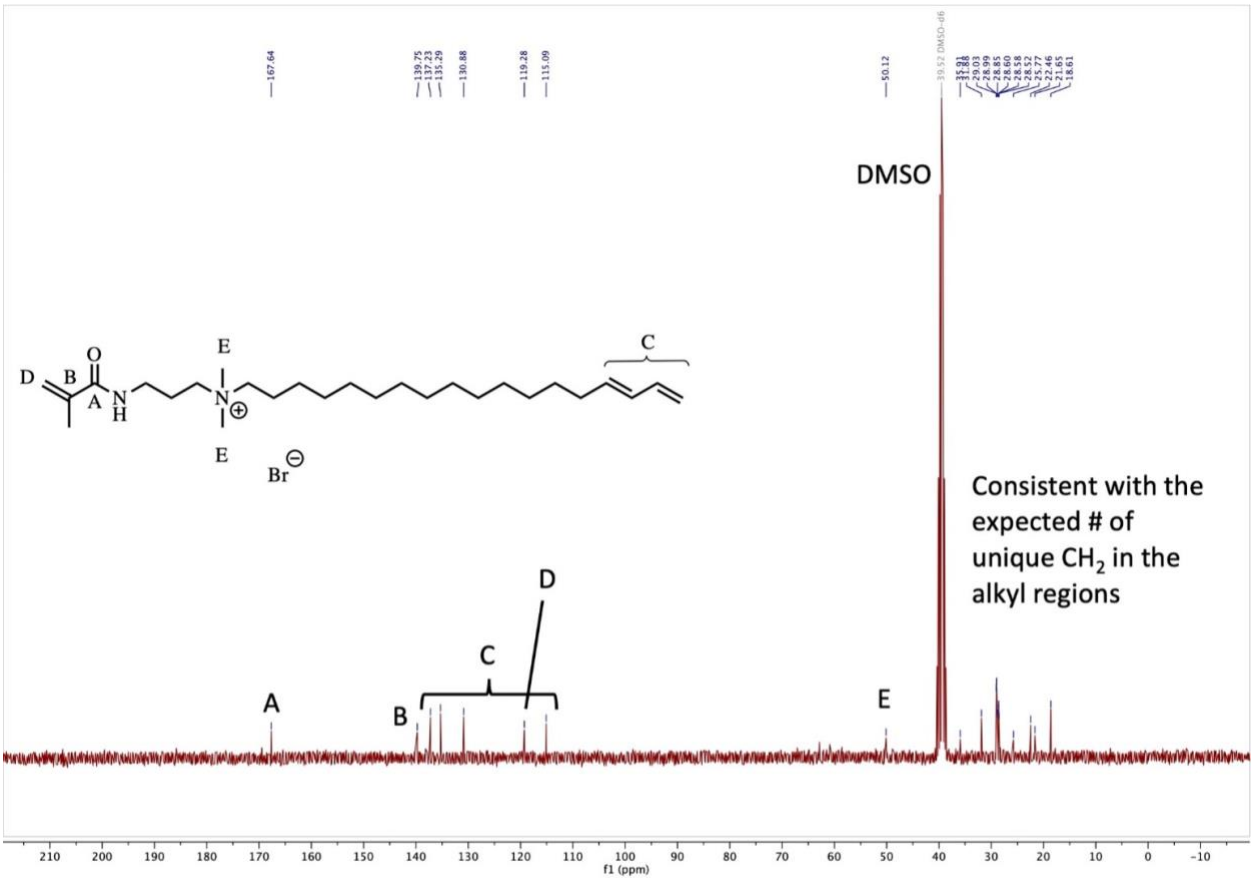

Figure 4.7 ^{13}C NMR spectrum of monomer **6** in DMSO-d_6.

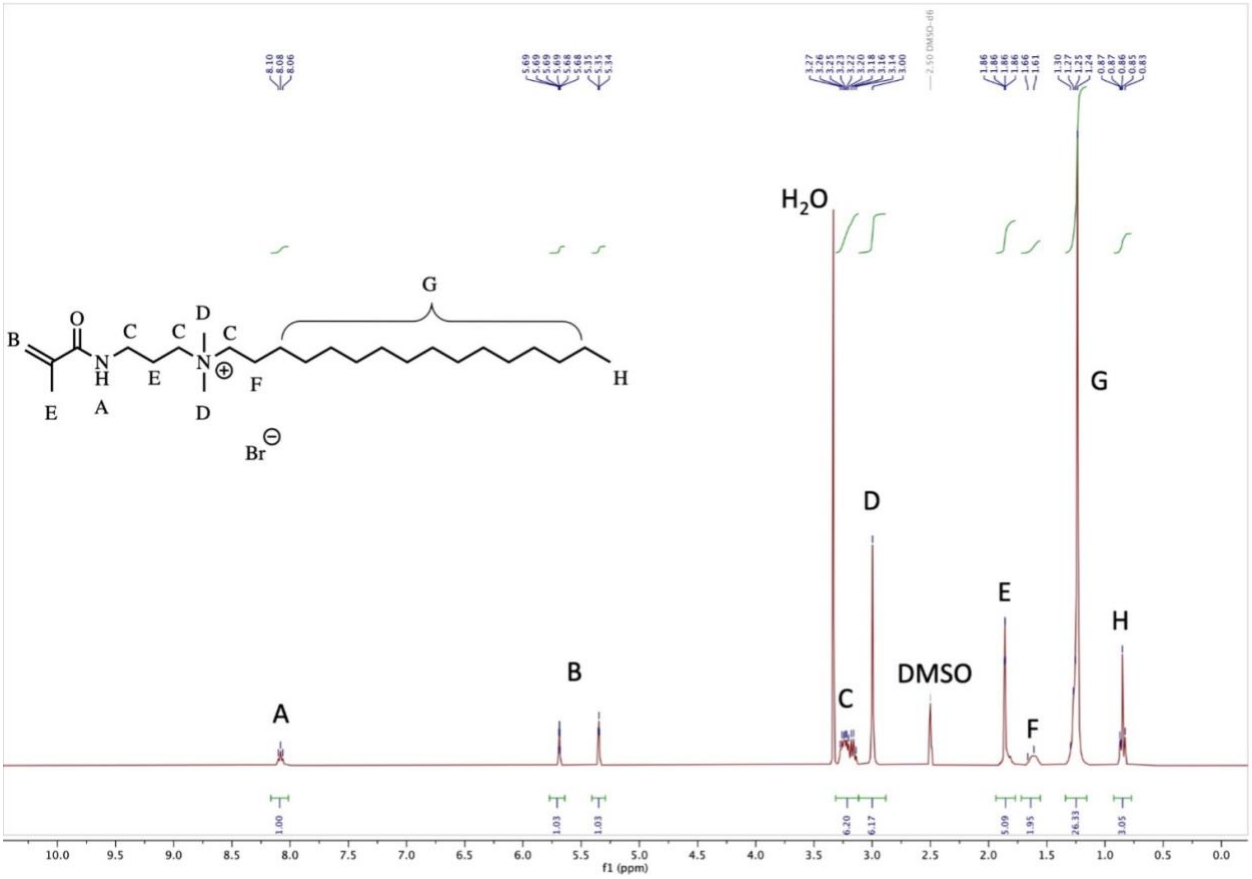

Figure 4.8 ^{1}H NMR spectrum of monomer **7** in DMSO-d_6.

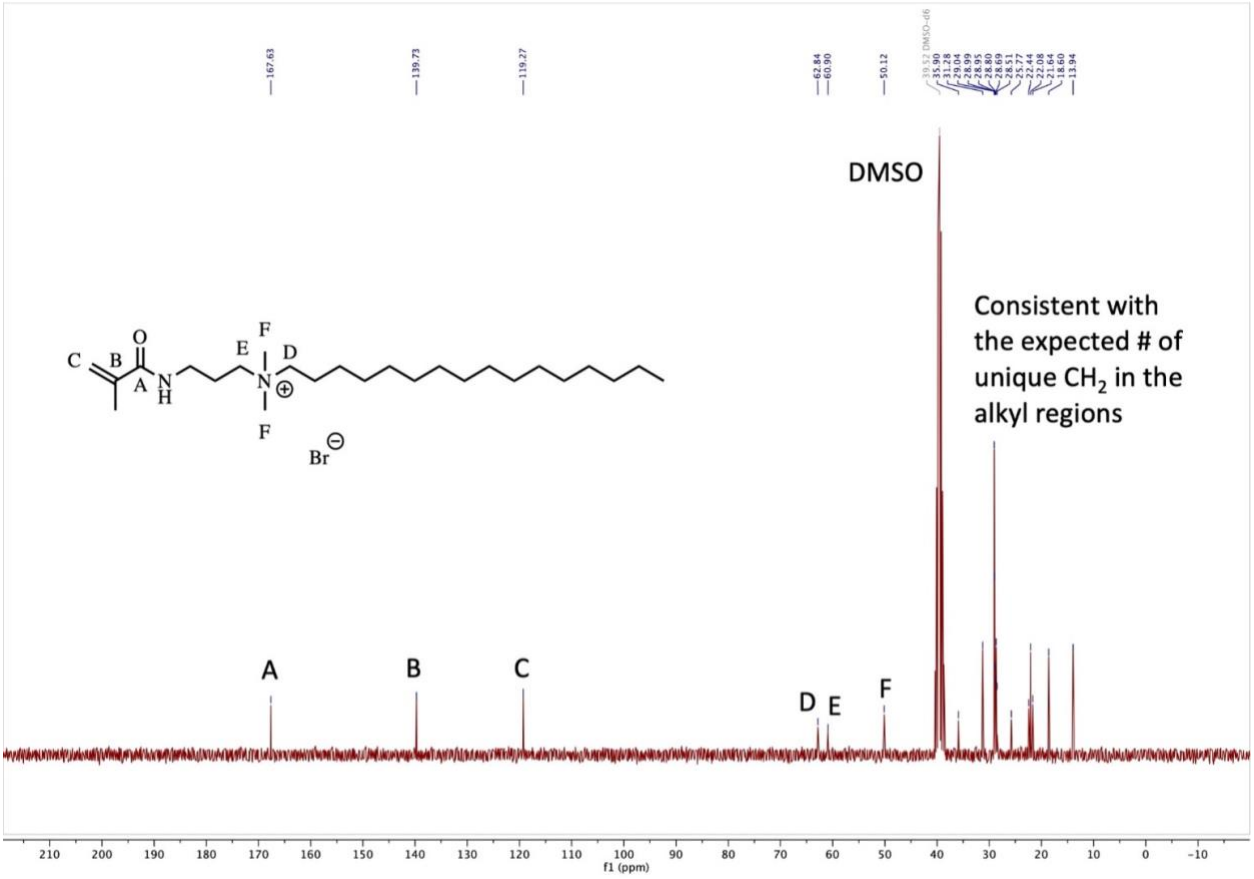

Figure 4.9 ^{13}C NMR spectrum of monomer **7** in DMSO-d_6.

4.5.2 Methods

4.5.2.1 Mesophase Compositions

Table 4.1 Compositions of the double-gyroid mesophases

Sample	**Monomer (wt%)**	**Water (wt%)**	**DMPA (wt%)**	**DDMA cross-linker (wt%)**
Monomer **6,** gyroid phase (base case)	87.5	11.5	1	0
Monomer **7,** gyroid phase	88	11	1	0
Monomer **7** + DDMA, gyroid phase	84	11	1	4

4.5.2.2 General Mesophase Formulation Procedure

In a 1.5-mL microcentrifuge tube, 100 μL of DMPA solution (1 wt% DMPA in ethyl acetate) were pipetted. The solvent was evaporated via vacuum, leaving ca. 1 mg DMPA initiator coated on the vial walls and base. Monomer powder (typically 87.5 mg) was measured into the vial, after which 11.5 μL of water were pipetted into the vial, for a total of 100 mg of vial contents.

The tubes at were centrifuged at 14500 rpm for ca. 1 h. After the centrifugation, the tubes were left in a 70 °C drying oven in the dark for 2 min, after which the contents of the tubes were manually mixed with a blunt needle. After these steps, the tubes were returned to the centrifuge for another 1 hour run at the same speed. This sequence of steps was repeated 2–4 times until a

uniformly transparent, high-viscosity gyroid monomer mesophase was formed in the centrifuge tubes, possessing a highly-viscous ‘gel-like’ consistency.

4.5.2.3 Polymer Film Fabrication Procedure

20–50 mg of the gyroid monomer mesophase was sandwiched between two clean glass slides, and then pressed until the mesophase spread to a sufficiently large area (typically >4 cm^2). On occasion a bench/shop vise was used to spread the high viscosity mesophase over a sufficiently large area between the glass slides.

The samples were placed in a chamber with nitrogen purge and UV-cross-linked by exposure to a beam from a 100-W Sunspot SM system. The lamp emission spectrum is distributed in the wavelength range between 250–450 nm, with the peak intensity at 365 nm. After UV exposure for 3 h, cross-linked gyroid films were obtained between the glass slides. A razor blade was used to remove sections of the polymer gyroid films from the glass substrate. The risk of water evaporation during this long-duration polymerization is minimized by the ‘sandwiching’ of the monomer mesophase between glass slides, which prevents the majority of the material from coming into contact with an evaporation surface. Further, the lack of observed phase change under POM (Figure 4.2) in the polymer film (i.e., gyroid to lamellar or crystal), combined with the very minor difference in SAXS traces of mesophase and polymer (Figure 4.2), indicate that any evaporation has a negligible effect on the nanostructure during the long polymerization.

4.5.2.4 Polarized Optical Microscopy (POM)

The unpolymerized monomer mesophase and the corresponding polymerized films were observed under crossed-polarizers using a Zeiss Axiovert 200 M inverted microscope with a CCD camera accessory connected to a computer.

4.5.2.5 Small-Angle X-ray Scattering (SAXS)

SAXS analysis was performed using a Xenocs Xeuss 2.0 system in the Dual Source and Environmental X-ray Scattering (DEXS) facility at the University of Pennsylvania. A GeniX3D Cu source with a wavelength of $\lambda = 1.54$ Å was used, with a typical sample to detector distance of 37.5 cm providing a range of accessible scattering vectors (q) from 0.016 to 1.4 $Å^{-1}$. Silver behenate was used as a standard for calibrating the sample-to-detector distance. Both monomer mesophase and polymer film samples were packed between Kapton windows. Foxtrot software was used for azimuthal integration of scattering patterns into 1-D plots of scattering intensity (I) versus q. The lattice parameter a of the double-gyroid unit cell was calculated from the q-values of the (211) peaks in the 1D plots via the relation $a = (2\pi\sqrt{6})/q$. For temperature-dependent SAXS measurements, a polymer film was placed on a Linkam heating stage (Model Number L-HFSX350). The stage was heated from 30 °C to 210 °C with a heating scan rate of 10 °C/min, and X-ray spectra were obtained at every 15 °C within the temperature range.

4.5.2.6 Fourier-transform Infrared (FTIR) Spectroscopy

FTIR spectra (neat) were recorded using an Agilent Cary 630 FTIR instrument single-reflection horizontal ATR accessory with diamond crystal.

4.5.2.7 Charged Dye Solute Adsorption Experiments

Gyroid polymer films (approximately 1 cm^2 in area) with weights ranging from 5.0 to 9.6 mg were immersed in 40-mL volumes of aqueous dye solutions and shaken on a laboratory vortex mixer for 72 h to encourage dye uptake. The following aq. concentrations were used for the various dyes: Methylene Blue (15 μM), Methyl Orange (15 μM), Rose Bengal (15 μM), and Reactive Red 120 (75 μM). After 72 h, the polymer films were removed from the dye solutions and photographed. The percent change in the absorbances of the dye solutions at the 0- and 72-h marks were measured from a Cary 300 UV-Vis spectrophotometer operated in transmission mode using a dual-beam configuration.

4.5.2.8 Uncharged Solute Filtration Experiments

A thick gyroid film (*ca.* 100 μm) was installed in a high-pressure stirred cell (HP4750 Stirred Cell). Active membrane area was *ca.* 2 cm^2 (membrane diameter of 1.6 cm). An aqueous Vitamin B12 feed solution (0.05 wt%, 369 μM) was permeated through the membrane at an applied pressure of ca. 500 psig (ca. 35 bar). The first 1 mL of permeate was discarded, and the second 1 mL was collected for measurement. VB12 rejection was quantified by the absorbance differences measured between feed and permeate solutions with a Cary 300 UV-Vis spectrophotometer.

4.5.3 Supplementary Data

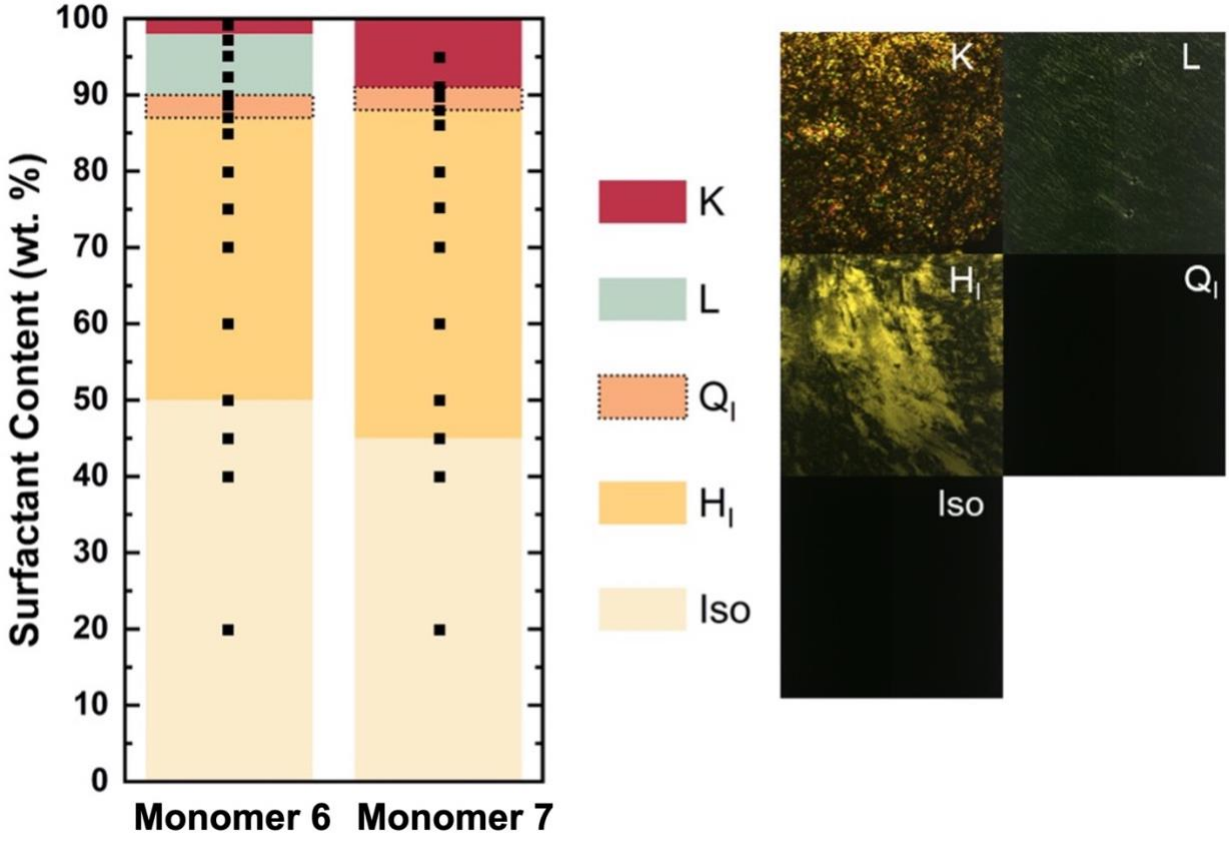

Figure 4.10 Binary phase diagrams of aqueous mixtures of monomer **6** and of monomer **7** at room temperature (22–25 °C), as approximately determined from POM analysis. Typical POM textures for micellar/isotropic (Iso), normal hexagonal (H_I), normal bicontinuous cubic (Q_I), lamellar (L) and crystal phases (K) are shown. (Note: The H and Q phases observed for monomer **6** + water were assigned as Type I (i.e., normal) phases based on their position on the water-excessive side of an observed central L phase (see Ref. 1)). On occasion, coexistence of phases was observed at the estimated phase boundaries. Black squares indicate compositions where mesophase determination was made via POM.

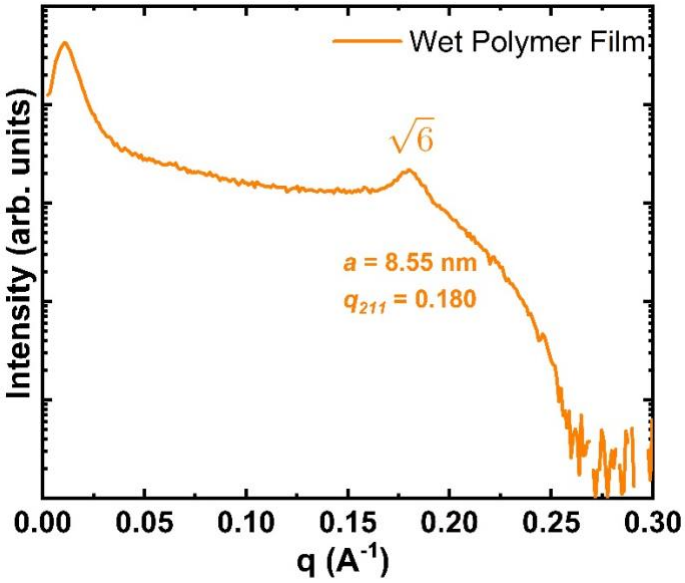

Figure 4.11 SAXS spectrum of a wet polymer film of **6** under non-vacuum conditions from a secondary (different q-range; lower-resolution) instrument (Rigaku SMAX-3000). The SAXS data were collected with the sample cavity filled with water. Due to the i) lower power and ii) shorter q-range of the non-vacuum instrument ($q < 0.22$ A^{-1}), as well as iii) the intensity attenuation from the presence of water in the sample holder, the (220) peak expected at $q = 0.208$ A^{-1} cannot be discerned. However, the lattice parameter of the wet film ($a = 8.55$ nm) was unchanged relative to the lattice parameter reported for a dry film in Figure 4.2 ($a = 8.55$ nm). This invariance of the structure indicates that water immersion does not significantly swell the gyroid polymer network.

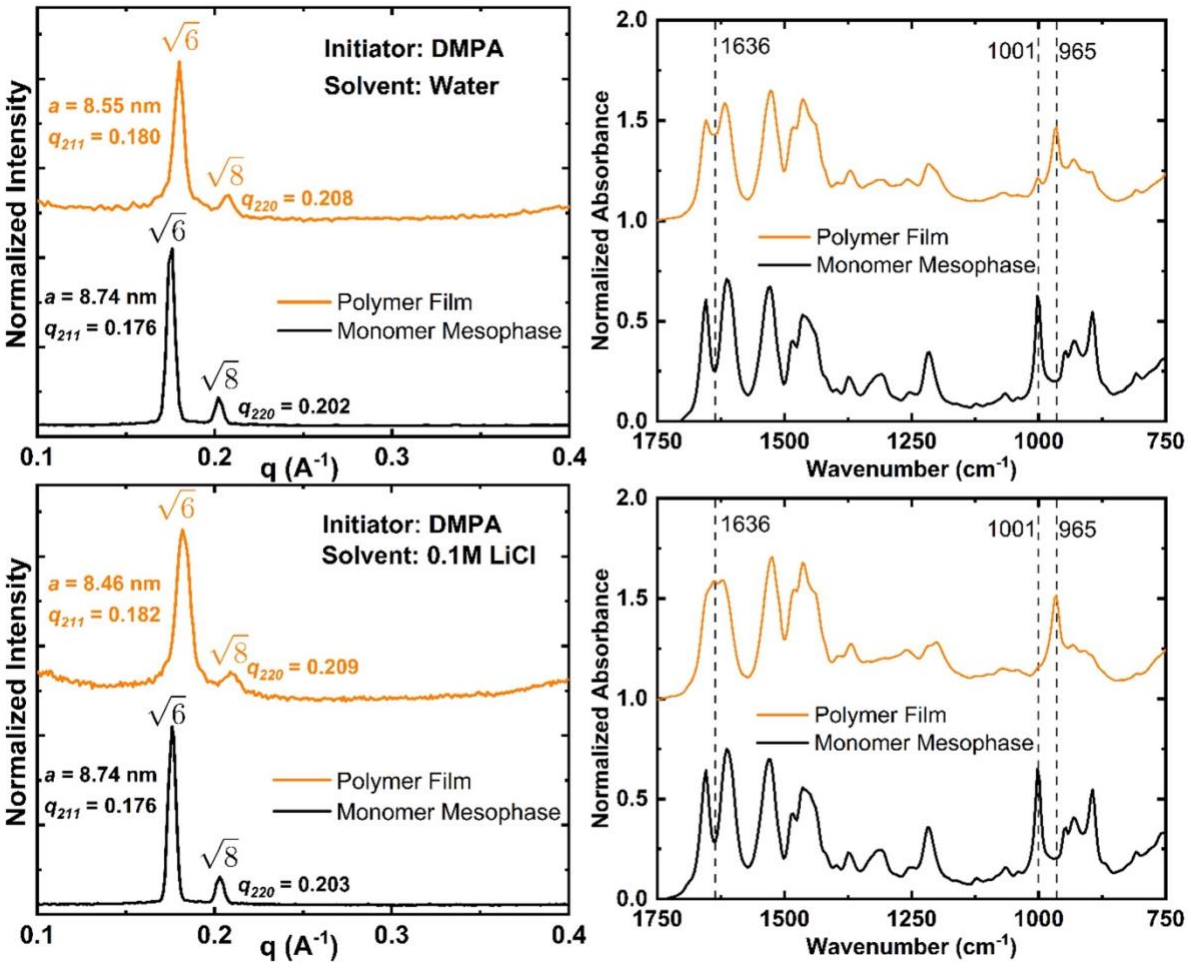

Figure 4.12 SAXS and FTIR data for double-gyroid polymer films of **6** formulated with water and 0.1 M aq. LiCl, with 1 wt% DMPA initiator used for both solvents. For both solvents, FTIR spectra show that the diene tails exhibit quantitative conversion (disappearance of peak at 1001 cm^{-1} and appearance of a peak at 965 cm^{-1}). The polymer made from the 0.1 M aq. LiCl-based Q-phase exhibits higher conversion of the methacrylamide headgroups (peak magnitude at 1636 cm^{-1}) than the corresponding water-based polymer material.

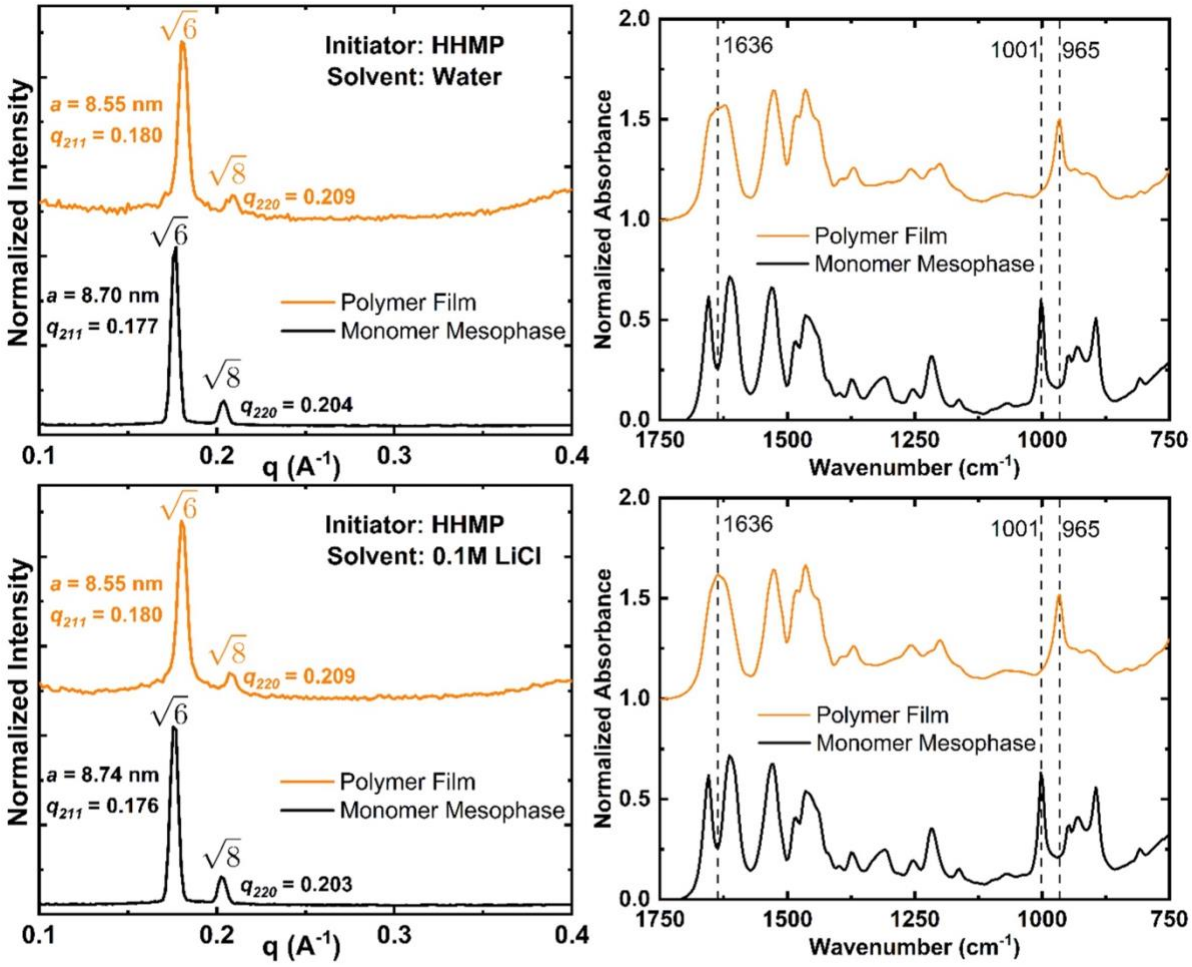

Figure 4.13 SAXS and FTIR data for double-gyroid polymer films of **6** formulated with water and separately with 0.1 M aq. LiCl, with 1 wt% HHMP initiator used for both solvent systems. In both cases, the diene tail groups and methacrylamide headgroups show near-quantitative conversion in the FTIR spectra.

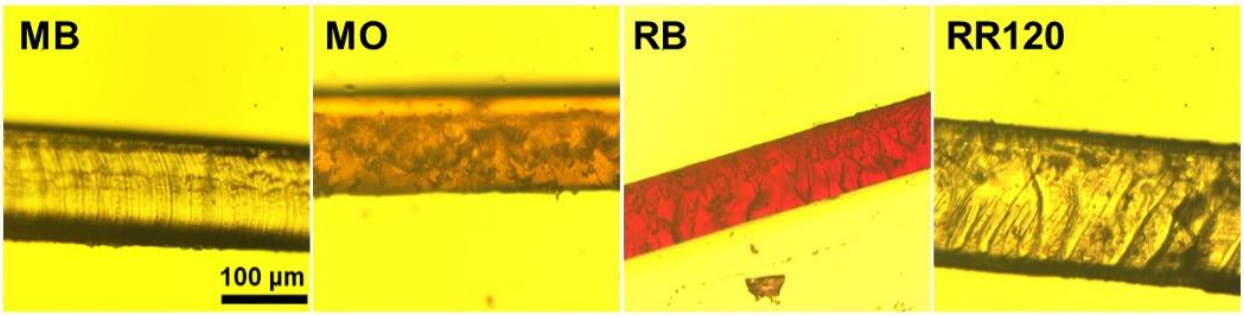

Figure 4.14 Optical micrographs of cross-sections of the gyroid polymer films of **6** shown in Figure 4.4. The absence of blue and red staining in MB and RR120 immersed films, respectively, indicates that the gyroid polymer pores are unable to adsorb those dyes in the film bulk due to charge and size exclusion mechanisms. Conversely, MO and RB dyes are fully infiltrated into the bulk of the gyroid films, providing additional evidence that the pore dimensions of the gyroid polymers are larger than the molecular sizes of those dyes.

4.5.4 Supplementary Calculations

4.5.4.1. Lipid and Water Domain Volume Fraction Calculation

Calculations of the water channel dimensions in a normal-type double-gyroid phase require estimates of lattice parameter *a* (obtained from SAXS), as well as volume fraction estimates for the lipid and water domains. We assume that the Br^- counterions associated with monomer **6** are present in the water channels. However, it is expected that Br^- ions are present near the pore walls; and further, that they act as 'hard spheres' to some degree, effectively constricting the pore dimension. To estimate this effect, in the subsequent calculations we include 50% of the Br^- volume fraction in the lipid volume ($\emptyset_{mem}$) and 50% in the water channel volume.

Table 4.2 Molecular weight and densities of monomer **6** components

	MW (Da)	**Wt %**	**Density (g/mL)**
Monomer 6 organic part	419.72	84	0.9 (assumed)
Monomer 6 Br^- ion	79.9	16	3.1

Table 4.3 Volume fraction calculations for various monomer **6** mesophase compositions

Mesophase	**H_I**	**Q_I**	**L**
***a* (nm)**	4.87	8.55	3.31
Monomer 6 (wt%)	70	88.5	93
Water (wt%)	30	11.5	7
Monomer 6 organic part (wt%)	58.8	74.34	78.1
Monomer 6 Br^- ion (wt%)	11.2	14.16	14.9
Monomer 6 organic part (vol%)	66	83.7	88.0
Monomer 6 Br^- ion (vol %)	3.7	4.6	4.9
Water (vol%)	30.3	11.7	7.1

4.5.4.2 Pore Diameter Calculation

Pore sizes within the *Ia3d* double-gyroid network were estimated from the approach outlined by Asghar et al. (Ref. 27). First, the molecular volume *v* is estimated by using molecular weight (MW), density, and Avogadro's number. Here we only use the MW of the organic portion.

$$v = \frac{MW}{\rho N_{Avo}} = 0.775\ nm^3 \qquad \text{(Eq. 4.1)}$$

Next, the cross-sectional area of the molecule (at area-neutral surface within the lipid layer) A_n is calculated from the lattice parameter of the lamellar phase (a = 3.31 nm) and the volume fraction of the solid phase $\emptyset_{mem}$= 0.9045 (i.e., 0.88 + 0.049/2).

$$A_n = \frac{2v}{a_{lamellar}\emptyset_{mem}} = 0.5177 \text{ nm}^2$$

(Eq. 4.2)

Once the molecular parameter A_n (assumed to constant for all mesophases) is obtained, the radius r of surfactant cylinders in the H_I phase is calculated from the hexagonal phase lattice parameter (a = 4.87 nm) and volume fraction $\emptyset_{mem}$= 0.6785 (i.e., 0.66 + 0.037/2).

$$r = \sqrt{\frac{\sqrt{3}\emptyset_{mem}a_{hex}^2}{2\pi}} = 2.106 \text{ nm}$$

(Eq. 4.3)

The cross-sectional area per surfactant molecule at the surfactant-water interface, $A_{\text{interface}}$ is then estimated as:

$$A_{interface} = \frac{2v}{r} = 0.7360 \text{ nm}^2$$

(Eq. 4.4)

Next, the molecular volume within the lipid bilayer corresponding to the area-neutral surface (assumed constant for all mesophases) is estimated as follows:

$$v_n = v\left(\frac{A_n}{A_{interface}}\right)^2 = 0.3834 \text{ nm}^3$$

(Eq. 4.5)

Lastly, the following implicit equation is used to calculate for *z*, which is the distance from the center of the water channel to area-neutral surface, by utilizing the geometric constants associated with *Ia3d* geometry ($A_0 = 3.091$, $\chi = -8$).

$$\frac{2A_0 a_{gyroid}^2}{A_n}\left(1 + \frac{2\pi\chi}{A_0 a_{gyroid}^2} z^2\right) = \left[\frac{a_{gyroid}^3 - 2A_0 a_{gyroid}^2 z\left(1 + \frac{2\pi\chi}{3A_0 a_{gyroid}^2} z^2\right)}{v_n}\right]$$

(Eq. 4.6)

The value of *z* was calculated to be *z* = 0.78 nm. The value *z* represents an upper-bound for the water channel radius, assuming the area-neutral surface is found at the surfactant-water interface. Therefore, the upper bound for water channel diameter is 1.56 nm (i.e., 2 x 0.78 nm). If it is assumed that the area-neutral surface is found 1 to 2 carbons deeper in the solid layer than the surfactant-water interface, then *z* can be estimated as 0.65 nm, giving a pore diameter estimate of 1.3 nm.

4.5.4.3 Dye Size Calculations

The estimation of the molecular sizes is a complex and context dependent calculation. The geometric mean calculation procedure used here has many limitations, such as reporting an intermediate value between the longest and shortest dimensions of the molecule, which can obscure the effect of the 'controlling' molecular dimension. However, one advantage of the geometric mean lies in providing a single number for relative comparison purposes between variously shaped molecules (e.g., cylindrical Methyl Orange versus globular Vitamin B12). The additional utility provided by more accurate chemical size calculations can also be minimal when considering that molecular conformations can change in confined electrostatic pore environments.

Molecular dimensions reported in Figure 4.4 for the five dyes were calculated through ChemDraw and Chem3D software. The chemical structures of the respective dyes were first drawn in ChemDraw and then imported into Chem3D. The counter-ions were excluded from the chemical structures of dyes to simplify the size calculations and to avoid the software reporting of anomalous numbers. The molecular structure was aligned with the x-axis and centered on the origin using the corresponding commands in the View menu. Following this, an MM2 'Minimize Energy' simulation was performed on the molecules (except VB12) for 1000 iterations to obtain a molecular conformation with more realistic bond lengths and angles. Cartesian coordinates for all atoms were generated from the corresponding command in the Chem3D View menu. The table of Cartesian coordinates was then exported to Microsoft Excel. Following this, the range for each coordinate dimension was calculated from the coordinates of all molecules (i.e. $x_{max} - x_{min}$, y_{max}-y_{min}, and z_{max}-z_{min}). Lastly, the GEOMEAN command in Excel was used to calculate the geometric mean of the *x*,*y*, and *z* range. The obtained geometric mean value is reported as the effective dye size in the manuscript and Figure 4.4.

Table 4.4 Calculated molecular dimensions for various dyes

Dye	**MW (Da)**	$x_{max} - x_{min}$ **(nm)**	$y_{max} - y_{min}$ **(nm)**	$z_{max} - z_{min}$ **(nm)**	**Geometric mean (nm)**
Methyl Orange	327	1.373	0.544	0.312	0.615
Methylene Blue	320	1.379	0.227	0.551	0.557
Rose Bengal	974	0.710	1.000	1.085	0.916
Reactive Red 120	1469	1.893	1.404	1.748	1.668
Vitamin B12	1355	1.438	1.696	1.362	1.492

4.5.4.4 Specific Surface Area (SSA) Calculation

We employ two methods here to estimate the specific surface area (*S*) of the double-gyroid *Ia3d* network.

The first estimation technique is adapted from work by Detsi et al.[29] Assuming that the *Ia3d* unit cell consists of 2 pores and 2 solid ligaments, we can estimate the ligament size d_l from the SAXS obtained lattice parameter *a* and previously calculated pore diameter ($d_p = z$) as follows:

$$d_l = \frac{a}{2} - d_p = \frac{8.55}{2} - 1.56 = 2.715 \text{ nm}$$

(Eq. 4.7)

Next, the formula below (adapted from Equation 5 of Ref. 29) is used to calculate *S* for the double-gyroid network, taking the value of dimensionless constant C = 5.8 and bulk density ρ = 1014 kg/m^3 (i.e., mass fraction weighted average of component densities in Table 4.2).

$$S = \frac{C}{\rho d_l}\left(\frac{d_l}{d_p}\right)^{-1} = 1210 \ \frac{\text{m}^2}{\text{g}}$$

(Eq. 4.8)

An alternate estimate of the specific surface area can be obtained from the approach outlined by Ravikovitch and Neimark.[30] First, the reduced surface area per unit cell A_1 is estimated as follows (adapted from Equation 2 of Ref. 30):

$$A_1 = A_0 + 2\pi\chi\left(\frac{d_l}{2a}\right)^2 = 1.825$$

(Eq. 4.9)

Next, *S* is estimated from the equation below (adapted from Equation 6 of Ref. 30).

$$S = \frac{2A_1}{\rho a \emptyset_{mem,gyroid}} = \frac{2(1.825)}{(1014)(8.55 \times 10^{-9})(0.86)} = 490\ \frac{\mathrm{m}^2}{\mathrm{g}}$$

(Eq. 4.10)

We note that both expressions for S follow essentially the same functional form and differ primarily in the value of the constant employed. The actual value of S is likely closer to the lower estimate (i.e., 490 $m^2\ g^{-1}$).

The estimates for S can also be used to roughly estimate the adsorption capacity of the gyroid polymers. Using the lower S estimate, the surface-area-per-headgroup A_n (Eq. 4.2), and Avogadro's number, an estimated n_{sites} for the number/moles of positively charged quaternary ammonium sites per mass of gyroid polymer is obtained:

$$n_{sites} = \frac{S}{A_n N_{Avo}} = \frac{490}{(5.18 \times 10^{-19})(6.022 \times 10^{23})} = 1.6 \times 10^{-3}\,\frac{\mathrm{mol}}{\mathrm{g}}$$

(Eq. 4.11)

Combining the above calculation with the absorption data in Figure 4.4, the masses of immersed polymer films, and an assumed 1:1 binding site ratio between dye molecule: quaternary ammonium headgroup, we can estimate the adsorption capacity used up by the dye uptake reported in Figure 4.4. For example, for the MO dye solution (V_{MO} = 40 mL, c_{MO} = 15 μmol/L, abs_{MO} = 90% absorption @ 72 hrs), the immersed polymer film had a mass m_{film} = 6.0 mg, leading to:

$$\text{Used Adsorption Capacity} = \frac{V_{\mathrm{MO}} c_{\mathrm{MO}} abs_{\mathrm{MO}}}{n_{sites} m_{\mathrm{film}}} = 0.057 = 5.7\ \%$$

(Eq. 4.12)

The above estimate can also be repeated for the RB dye (V_{MO} = 40 mL, c_{MO} = 15 μmol/L, abs_{MO} = 55% absorption @ 72 h, m_{film} = 5.0 mg), leading to an estimate for 4.2% used capacity. These estimates indicate that most likely the actual equilibrium absorption capacity of the gyroid

polymers is much higher than the measured adsorption numbers at the 72-h mark for MO (29 mg/g or 90 μmol/g) and RB (64 mg/g or 66 μmol/g) dyes.

It should be noted that the above calculations are rough estimates and can be performed with different assumptions to obtain different estimates. For instance, for the estimated surface area per headgroup, $A_{interface}$ (Eq. 4.4) can be used instead of A_n (Eq. 4.2). Similarly, for adsorption capacity estimates, the larger estimate of S (1210 m^2/g) can be utilized. Given that the RB dye molecule has 2 negatively charged sites, the adsorption capacity of the polymer films can be estimated differently by assuming a 1:2 dye molecule: quaternary ammonium headgroup ratio. Additional complexities not addressed by these rough estimates include the relative geometric confinement of dye molecules within the channel dimensions disrupting perfect monolayer formation, and the possibility of progressively slower diffusion deeper into the bulk of the gyroid polymer film.

Finally, the areal density σ of quaternary ammonium species at the water interface can be used with an assumption regarding stoichiometry of the dye based on electrostatic interactions (e.g., 1 RB per 2 quaternary ammonium sites) to arrive at an estimate for the adsorption capacity. Functionally this is related to the estimate above for n_{sites}, but it uses the estimate of the ligament size d_l as the starting point. For a lamellar sheet of thickness t the volume per unit area is $t/2$ as there are two surfaces and the mass is $m = t\rho/2$ where ρ is the density of the polymer sheet. The number of groups at the surface per unit area is then the product of the number of groups per molecule ($g_m = 1$ quaternary ammonium), the number of molecules per unit thickness of the sheet ($m_s = 2$, due to bilayer arrangement), the mass $t\rho$, and Avogadro's number, divided by the molar mass of the molecules. Here, with 499.6 the molar mass of monomer **6**, the estimated areal density is:

$$\sigma_{LAM}\sigma = \frac{g_m m_s m}{M} N_{Avo} = \frac{t\rho}{M} N_{Avo} = 3.2\ \text{nm}^{-2}$$

(Eq. 4.13)

For cylinders of diameter D, $m = \frac{\rho D}{4}$ and the areal density is given by a similar expression, reduced by a factor of 2

$$\sigma_{CYL} = \frac{D\rho}{2M} N_{Avo} = 1.6\ \text{nm}^{-2}$$

(Eq. 4.14)

For completeness, for spheres, per unit area, the mass is $m = \frac{\rho D}{6}$ and the corresponding expression for areal density of sites is:

$$\sigma_{SPH} = \frac{D\rho}{3M} N_{Avo}$$

(Eq. 4.15)

If we use the geometric mean of the LAM and CYL results to approximate the expected areal density for a gyroid surface, we yield 2.3 nm^{-2}. This number agrees reasonably well with the expected areal density of roughly 2 nm^{-2} based on $\sigma_{GYR} = 1/A_n$.

We can estimate the absorption capacity n_{sites} now as

$$\sigma_{SPH} n_{sites} = \frac{S\,\sigma}{N_{Avo}} = \frac{(490)(2.3 \times 10^{18})}{(6.022 \times 10^{23})} = 1.9 \times 10^{-3}\,\frac{\text{mol}}{\text{g}}$$

(Eq. 4.16)

4.5.5 Acknowledgments

C. O. O. and O. Q. I. acknowledge NSF support through CBET 2010890. C. O. O. also acknowledges NSF support through DMF-1945966. The authors acknowledge use of the DEXS

facility at the Univ. of Pennsylvania (NSF MRSEC 1720530), the purchase of which was made possible by NSF MRI 1725969, ARO DURIP W911NF-17-1-0282, and the Univ. of Pennsylvania. P.L. and D. L. G. thank the Joint Science and Technology Office for Chemical Biological Defense (JSTO CBD) for funding under CB10872.

4.6 References

1. For reviews of cross-linked LLC phases and their applications, see: (a) Gin, D. L.; Lu, X.; Nemade, P. R.; Pecinovsky, C. S.; Xu, Y.; Zhou, M. Recent Advances in the Design of Polymerizable Lyotropic Liquid-Crystal Assemblies for Heterogeneous Catalysis and Selective Separations. *Adv. Funct. Mater*. **2006**, *16*, 865–878. (b) Mueller, A.; O'Brien, D. F. Supramolecular Materials via Polymerization of Mesophases of Hydrated Amphiphiles. *Chem. Rev*. **2002**, *102*, 727–758. (c) Gin, D. L.; Gu, W.; Pindzola, B. A.; Zhou, W. Polymerized Lyotropic Liquid Crystal Assemblies for Materials Applications. *Acc. Chem Res.* **2001**, *34*, 973–980.
2. Wiesenauer, B. R.; Gin, D. L. Nanoporous Polymer Materials Based on Self-Organized, Bicontinuous Cubic Lyotropic Liquid Crystal Assemblies and Their Applications. *Polym. J.* **2012** *44*, 461–468.
3. Lee, Y. S.; Yang, J. Z.; Sisson, T. M.; Frankel, D. A.; Gleeson, J. T.; Aksay, E.; Keller, S. L.; Gruner, S. M.; O'Brien, D. F. Polymerization of nonlamellar lipid assemblies. *J. Am. Chem. Soc.* **1995**, *117*, 5573–5578.
4. Srisiri, W.; Benedicto, A.; O'Brien, D. F. Stabilization of a bicontinuous cubic phase from polymerizable monoacylglycerol and diacylglycerol. *Langmuir* **1998**, *14*, 1921–1926.

5. Pindzola, B. A.; Jin, J.; Gin, D. L. Cross-Linked Normal Hexagonal and Bicontinuous Cubic Assemblies via Polymerizable Gemini Amphiphiles. *J. Am. Chem. Soc.* **2003**, *125*, 2940–2949.
6. Hatakeyama, E. S.; Wiesenauer, B. R.; Gabriel, C. J.; Noble, R. D.; Gin, D. L. Nanoporous, bicontinuous Cubic Lyotropic Liquid Crystal Networks via Polymerizable Gemini Ammonium Surfactants. *Chem. Mater.* **2010**, *22*, 4525–4527.
7. Carter, B. M.; Wiesenauer, B. R.; Hatakeyama, E. S.; Barton, J. L.; Noble, R. D.; Gin, D.L. Glycerol-based Bicontinuous Cubic Lyotropic Liquid Crystal Monomer System for the Fabrication of Thin-film Membranes with Uniform Nanopores. *Chem. Mater.* **2012**, *24*, 4005–4007.
8. Lu, X.; Nguyen, V.; Zhou, M.; Zeng, X.; Jin, J.; Elliott, B. J.; Gin, D. L. Cross-linked Bicontinuous Cubic Lyotropic Liquid Crystal-Butyl Rubber Composites: Highly Selective, Breathable Barrier Materials for Chemical Agent Protection. *Adv. Mater.* **2006**, *18*, 3294–3298.
9. Kobayashi, T.; Li, Y.-X.; Ono, A.; Zeng, X.-B.; Ichikawa, T. Gyroid structured aqua-sheets with sub-nanometer thickness enabling 3D fast proton relay conduction. *Chem. Sci.* **2019**, *10*, 6245–6253.
10. Maekawa, A.; Kobayashi, T.; Ichikawa, T. Gyroid nanostructured soft membranes formed by controlling the degree of crosslinking polymerization of bicontinuous cubic liquid-crystalline monomers. *Polym. J.* **2021**, *53*, 463–470.
11. Kobayashi, T.; Li, Y.-X.; Hirota, Y.; Maekawa, A.; Nishiyama, N.; Zeng, X.-B.; Ichikawa, T. Gyroid-Nanostructured All-Solid Polymer Films Combining High H^+ Conductivity with Low H_2 Permeability. *Macromol. Rapid. Commun.* **2021**, 2100115.

12. Jennings, J.; Green, B.; Mann, T. J.; Guymon, C. A.; Mahanthappa, M. K. Nanoporous Polymer Networks Templated by Gemini Surfactant Lyotropic Liquid Crystals. *Chem. Mater.* **2018**, *30*, 185–196.
13. Kerr, R. L.; Miller, S. A.; Shoemaker, R. K.; Elliott, B. J.; Gin, D. L. New Type of Li Ion Conductor with 3D Interconnected Nanochannels via Polymerization of a Liquid Organic Electrolyte-Filled Lyotropic Liquid-Crystal Assembly. *J. Am. Chem. Soc*. **2009**, *131*, 15972–15973.
14. Zhang, H.; Li, L.; Möller, M.; Zhu, X.; Rueda, J. J. H.; Rosenthal, M.; Ivanov, D. A. From channel-forming ionic liquid crystals exhibiting humidity-induced phase transitions to nanostructured ion-conducting polymer membranes. *Adv. Mater*. **2013**, *25*, 3543–3548.
15. Takeuchi, H.; Ichikawa, T.; Yoshio, M.; Kato, T.; Ohno, H. Induction of bicontinuous cubic liquid-crystalline assemblies for polymerizable amphiphiles via tailor-made design of ionic liquids. *Chem. Commun.* **2016**, *52*, 13861–13864.
16. McGrath, K. M.; Drummond, C. J. Polymerisation of liquid crystalline phases in binary surfactant/water systems. Part 1. Allyldodecyldimethylammonium bromide and allyldidodecylmethylammonium bromide. *Colloid Polym. Sci.* **1996**, 274, 316–333.
17. Yang, D.; O'Brien, D. F.; Marder, S. R. Polymerized bicontinuous cubic nanoparticles (cubosome) from a reactive monoacylglycerol. *J. Am. Chem. Soc.* **2002**, *124*, 13388–13389.
18. Gao, X.; Lu, F.; Liu, Y.; Sun, N.; Zheng, L. The facile construction of an anion exchange membrane with 3D interconnected ionic nano-channels. *Chem. Commun.* **2017**, *53*, 767–770.
19. Wu, H.; Xu, F.; Gao, G.; Feng, X. Highly Ordered Interconnected 1 nm Pores in Polymers Fabricated from Easily Accessible Gyroid Liquid Crystals. *Macromolecules* **2021**, *54*, 5856–5865.

20. Feng, X.; Imran. Q.; Zhang, Y.; Sixdenier, L.; Lu, X.; Kaufman, G.; Gabinet, U.; Kawabata, K.; Elimelech, M.; Osuji, C. O. Precise nanofiltration in a fouling-resistant self-assembled membrane with water-continuous transport pathways. *Sci. Adv.* **2019**, *5*, eaav9308.
21. Pindzola, B. A.; Hoag, B. P.; Gin, D. L. Polymerization of a Phosphonium Diene Amphiphile in the Regular Hexagonal Phase with Retention of Mesostructure. *J. Am. Chem. Soc.* **2001**, *123*, 4617–4618.
22. Hoag, B. P.; Gin, D. L. Cross-Linkable Liquid Crystal Monomers Containing Hydrocarbon 1,3-Diene Tail Systems. *Macromolecules* **2000**, *33*, 8549–8558.
23. Sisson, T. M.; Srisiri, W.; O'Brien, D. F. Novel Polymer Architectures via the Selective Polymerization of Lyotropic Liquid Crystals of Heterobifunctional Amphiphiles. *J. Am. Chem. Soc.* **1998**, *120*, 2322–2329.
24. Liu, S.; O'Brien, D. F. Cross-Linking Polymerization in Two-Dimensional Assemblies: Effect of the Reactive Group Site. *Macromolecules* **1999**, *32*, 5519– 5524.
25. Liu, S.; Sisson, T. M.; O'Brien, D. F. Synthesis and Polymerization of Heterobifunctional Amphiphiles to Cross-Link Supramolecular Assemblies. *Macromolecules*, **2001**, *34*, 465–473.
26. Zhang, Y.; Dong, R.; Gabinet, U. R.; Poling-Skutvik, R.; Kim, N. K.; Lee, C.; Imran, O. Q.; Feng, X.; Osuji, C. O. Rapid Fabrication by Lyotropic Self-Assembly of Thin Nanofiltration Membranes with Uniform 1 Nanometer Pores. *ACS Nano* **2021**, *15*, 8192–8203.
27. Asghar, K. A.; Rowlands, D. A.; Elliott, J. M.; Squires, A. M. Predicting Sizes of Hexagonal and Gyroid Metal Nanostructures from Liquid Crystal Templating. *ACS Nano* **2015**, *9*, 10970–10978.

28. Dischinger, S. M.; Rosenblum, J.; Noble, R. D.; Gin, D. L.; Linden, K. G. Application of a lyotropic liquid crystal nanofiltration membrane for hydraulic fracturing flowback water: Selectivity and implications for treatment. *J. Membr. Sci.* **2017**, *543*, 319–327.
29. Detsi, E.; De Jong, E.; Zinchenko, A.; Vukovic, Z.; Vukovic, I.; Punzhin, S.; Loos, K.; ten Brinke, G.; De Raedt, H. A.; Onck, P. R.; De Hosson, J. T. M. On the specific surface area of nanoporous materials. *Acta Mater.* **2011**, *59*, 7488–7497.
30. Ravikovitch, P. I.; Neimark, A. V. Relations between Structural Parameters and Adsorption Characterization of Templated Nanoporous Materials with Cubic Symmetry. *Langmuir* **2000**, *16*, 2419–2423.

Chapter 5: A pH- and Light-responsive Nanoporous Lyotropic Gyroid Polymer Network

In the collaborative work detailed in this chapter (and associated joint publication), I designed, synthesized, and structurally characterized the new spiropyran monomer. I also demonstrated the ability to blend monomer **6** and **8** together to yield reversible, acidochromic changes bulk polymer films. Finally, I designed and carried out the UV-light-mediated ion uptake studies.

(A modified version of this chapter was originally submitted to *Advanced Materials* as: Li, P.; Johnson, C.; Dyer, S. S.; Osuji, C. O.; Gin, D. L. "A pH- and Light-responsive Nanoporous Lyotropic Gyroid Polymer Network." *Adv. Mater.* **2022**, submitted.

5.1 Abstract

Bicontinuous cubic (Q) lyotropic liquid crystal (LLC)-derived polymer networks possess periodic, uniform-size, 3D-interconnected nanopores that make them highly desirable organic materials for selective molecular separation and uptake applications. To date, there are no reported examples of a Q-phase network with additional functional properties, such as catalytic reactivity, response to external stimuli, or gated transport, that would expand the usefulness of this class of porous materials. Here, we present a functionalized gyroid-type Q polymer network material that can be used for potential gated transport or adaptive uptake applications. This material contains a novel spiropyran-containing dopant monomer that upon blending and cross-linking with a gyroid-forming LLC monomer, yields a gyroid polymer material that retains its phase architecture while reversibly responding to changes in external solution and vapor pH. Our studies also demonstrate

that this system is capable of irreversibly binding to aq. Pb^{2+} ions when activated by UV light, allowing it to function as a potential colorimetric sorbent or gated-response material.

5.2 Introduction

Lyotropic liquid crystal (LLC) networks are nanostructured cross-linked polymer materials with periodic, molecular-size pores that have been found to be useful for important applications such as templated synthesis, heterogeneous catalysis, molecular-size filtration, vapor transport, and enhanced ion transport.[1] LLC networks are prepared by designing reactive (i.e., polymerizable) organic amphiphiles (i.e., LLC monomers) that, upon mixing with a polar liquid such as water, phase-separate into ordered but fluid arrays with monodisperse, nanoscale hydrophobic and hydrophilic domains (i.e., LLC phases).[2] The resulting LLC phases are soft gels that can then be converted into physically robust solid materials by cross-linking the monomers. Properly executed, such cross-linking preserves the ordered nanostructure of the LLC phase, resulting in an ordered polymer network with nanoscale structure.[1] Typically, the cross-linking occurs in the hydrophobic domains formed by the polymerizable tails of the amphiphilic monomers, leaving the water-filled hydrophilic domains to act as open pores for molecular transport, uptake, or functional group localization/concentration.[1]

LLC phases (and the nanoporous polymer materials formed from them) have a range of dimensionalities and symmetries, depending on the structure and packing of the phase-separated domains formed by the amphiphiles. Close-packed normal (Type I) or inverted (Type II) cylindrical micelles form the 1D hexagonal (H) phases; stacks of planar sheets form the 2D lamellar (L) phase; and 3D-interpenetrating hydrophilic and hydrophobic domains separated by a cubic bicontinuous layer form the bicontinuous cubic (Q) phases (which can also be Type I

(normal) or Type II (inverted)).[2,3] Although formation of a particular LLC phase is primarily dependent upon system composition, specific LLC phases can also be favored to form via amphiphile design or by modulating system temperature and pressure.[1–3] Pore size within a targeted phase can also be modified to a limited degree by careful adjustment of the same parameters.[2,3] In addition to phase structure and pore size tunability, it is also possible to incorporate additional capabilities into LLC networks by including functional groups on the amphiphile headgroups that make up the walls of the pores. The ability to control both phase architecture and nanopore environment is one of the hallmarks of LLC networks as a class of functional organic nanomaterials.

Although numerous cross-linked LLC materials are known, Q-phase networks in particular are highly sought after for molecular separation and uptake applications.[4] This is because Q phases possess 3D-interconnected nanopores that do not require macroscopic pore alignment for good transport or access as in the case of lower-dimensionality LLC phases such as the H and L phases.[4] Q-phase LLC networks have been demonstrated to be useful for breathable toxic agent vapor rejection,[5,6] water desalination,[7,8] and enhanced ion-transport.[9] However, only a very limited number of intrinsically cross-linkable Q-phase LLC monomer platforms have been reported that can be cross-linked with phase retention. Q phases are more sensitive than lower-dimensionality LLC phases and require specific amphiphile structural motifs and precise amphiphile/solvent compositions in order to achieve a phase.[2] As a result, Q-phase network materials have typically been designed from rather elaborate monomer motifs (i.e., symmetric gemini amphiphiles,[7,10-12] wedge-shaped amphiphiles,[9] and traditional lipid-like amphiphiles,[13]) that require complex/costly syntheses and are difficult to scale up. Only recently has a structurally simpler (i.e., single-head/single-tail), intrinsically cross-linkable Q-phase-forming monomer motif (**6**) been developed

to address these issues (see Figure 5.1 for the structure of this monomer).[14] This monomer forms a Type I bicontinuous cubic (Q_I) phase with a gyroid-type unit cell. The resulting gyroid-type Q_I-phase polymer network formed from **6** exhibits excellent structural stability in a variety of aqueous and organic solvents, and like previous ionic Q LLC networks, is capable of molecular size and charge discrimination.[14]

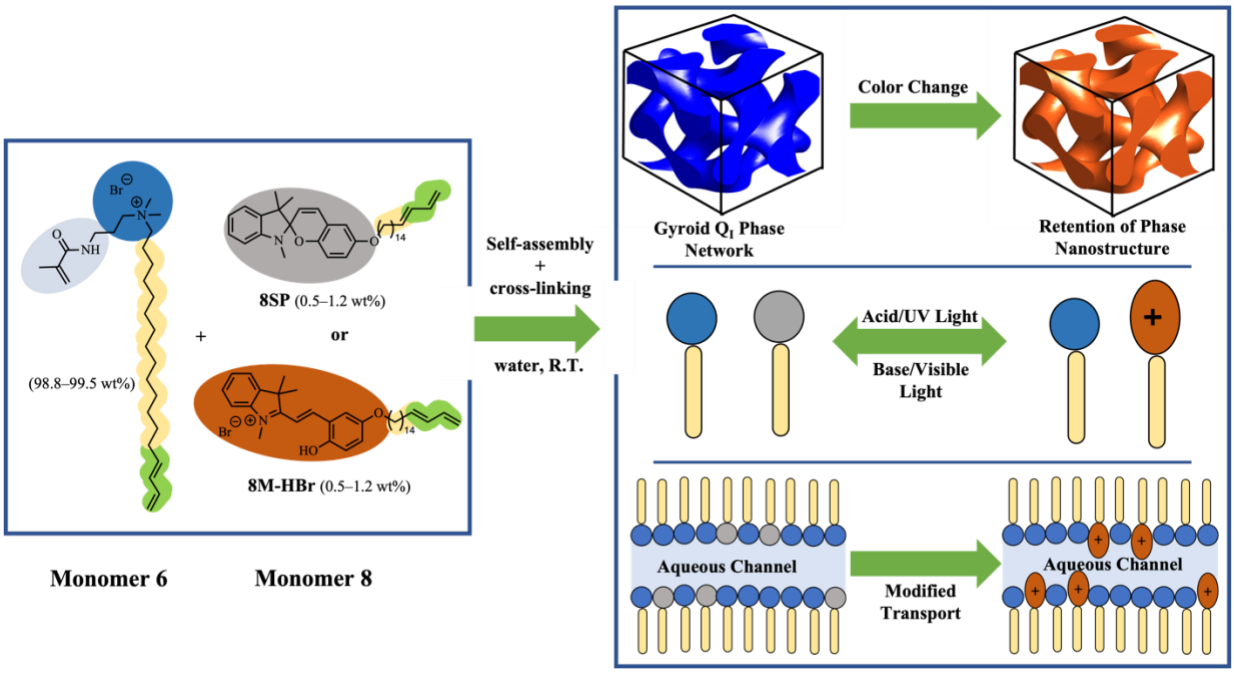

Figure 5.1 Structures of previously developed Q_I-phase-forming LLC monomer **6** and novel non-LLC-forming co-monomer platform **8** in its spiropyran form (**8SP**) and its protonated-merocyanine form (**8M-HBr**) (blue/light-blue = hydrophilic region, yellow = hydrophobic region, green = polymerizable group, gray = spiropyran group, orange = protonated-merocyanine group). Various blends of (**6** + **8SP**) and (**6** + **8M-HBr**) self-assemble into gyroid-type Q_I phases that can be cross-linked in situ with retention of the phase order. The resulting nanoporous gyroid polymer networks undergo reversible physical changes in terms of color and unit cell dimensionality

5.3 Results and Discussion

Intrinsically cross-linkable LLC monomer **6** was chosen as the gyroid-phase forming monomer because of its relatively simple and modular synthesis and because of the high thermal and chemical/solvent stability of the cross-linked network that it forms.[14] Because of these

features, a spiropyran-based derivative of **6** (i.e., monomer platform **8**) was chosen as an initial design target for a functional Q-phase monomer, or as a functional monomer dopant for blending into the Q phase of **6**, since spiropyran-merocyanine switching in response to various stimuli is well researched.[17-23] Monomer **8SP** was synthesized by reacting 1',3',3'-trimethyl-6-hydroxyspiro(2*H*-1-benzopyran-2,2'-indoline) with 18-bromooctadeca-1,3-diene in a solution of K_2CO_3 and $HCON(CH_3)_2$ at 80 °C in an S_N2 reaction. After purification, the structure and purity of **8SP** were verified by ^{1}H NMR, ^{13}C NMR, FT-IR, UV-visible, HRMS, and elemental analyses (see Section 5.5 for more details). The acidochromic conversion of **8SP** to **8M-HBr** was achieved by dissolving **8SP** in an 1:1 (v/v) solution of $(CH_3)_2CO$: CH_2Cl_2 and adding an equimolar amount of 0.422 M aq. HBr solution.[21] The structure and purity of **8M-HBr** were verified by ^{1}H NMR, ^{13}C NMR, FT-IR, UV-visible, HRMS, and elemental analyses (see the Section 5.5 for more details). The 1,3-diene polymerizable tail was chosen for the spiropyran-based monomers to maintain compatibility with the polymerizable diene tail of **6**.

Unfortunately, preliminary phase screening of **8SP** and **8M-HBr** did not reveal any relevant LLC phase behavior. The lack of LLC behavior echoes the general difficulty in designing novel Q-phase-forming LLC monomers. Previous studies have shown that blending and co-polymerization of functionalized non-LLC-phase-forming monomers with LLC monomers of similar structure can yield functional polymer networks with the desired phase.[15] However, the formation of functionalized cross-linkable LLC blends using this approach has only been demonstrated to be possible with the H_{II} phase.[15] Q-phase-forming monomers have been blended with co-monomers to tune the Q-phase window, but there is yet to be an example in which a functional co-monomer is blended with a Q-phase monomer to yield a Q-phase material with functional properties outside of basic molecular sieving.[4]

Despite the lack of LLC phase behavior from monomers **8SP** and **8M-HBr**, various blends of **6** and these two forms of **8** were prepared with a goal of evenly distributing the spiropyran-based monomer throughout the resulting gyroid LLC phase with retention of the spiropyran functional group's chromic sensitivity. [Because gyroid phases were obtained with blends of both (**6** + **8SP**) and (**6** + **8M-HBr**), for the remainder of this manuscript such monomer blends will be referred to as (**6** + **8**) for brevity.] It was found that 0.5–1.2 wt% of **8** with respect to **6** formed a stable gyroid phase at a composition of 87.5/11.5/1.0 (w/w/w) monomer blend (**6** + **8**)/water/2,2-dimethoxy-2-phenylacetophenone (DMPA, a radical photo-initiator) at room temperature (22 °C). Polymer films with retention of the gyroid structure (typical thicknesses between 50–150 μm) were obtained by radically photo-cross-linking the monomer mesophase with 365-nm UV light under N_2 purge for ca. 3 h at room temperature. FT-IR spectroscopy confirmed the near-complete conversion of the polymerizable groups (see Figure 5.13). The monomer mesophase and resulting cross-linked polymer films exhibited uniformly dark images under polarized light microscopy (PLM) analysis, consistent with the optically isotropic nature of Q phases. Small-angle X-ray scattering (SAXS) spectra of the monomer mesophase and cross-linked films revealed the characteristic $\sqrt{6} : \sqrt{8}$ relative Bragg peak locations associated with a gyroid-type Q phase (Figure 5.2).[1,4] Temperature stability studies on the polymer films of these (**6** + **8**) blends indicated that the cross-linked gyroid phase is stable up to 120 °C with no distinct changes to the lattice parameter beyond a small amount of temperature-induced drying (see Figure 5.14). Unlike the colorless materials formed with just monomer **6**,[14] the monomer mesophases and polymer films of (**6** + **8**) described in this study are slightly colored (very pale yellow to very pale orange) due to the added spiropyran-based dopant monomer.

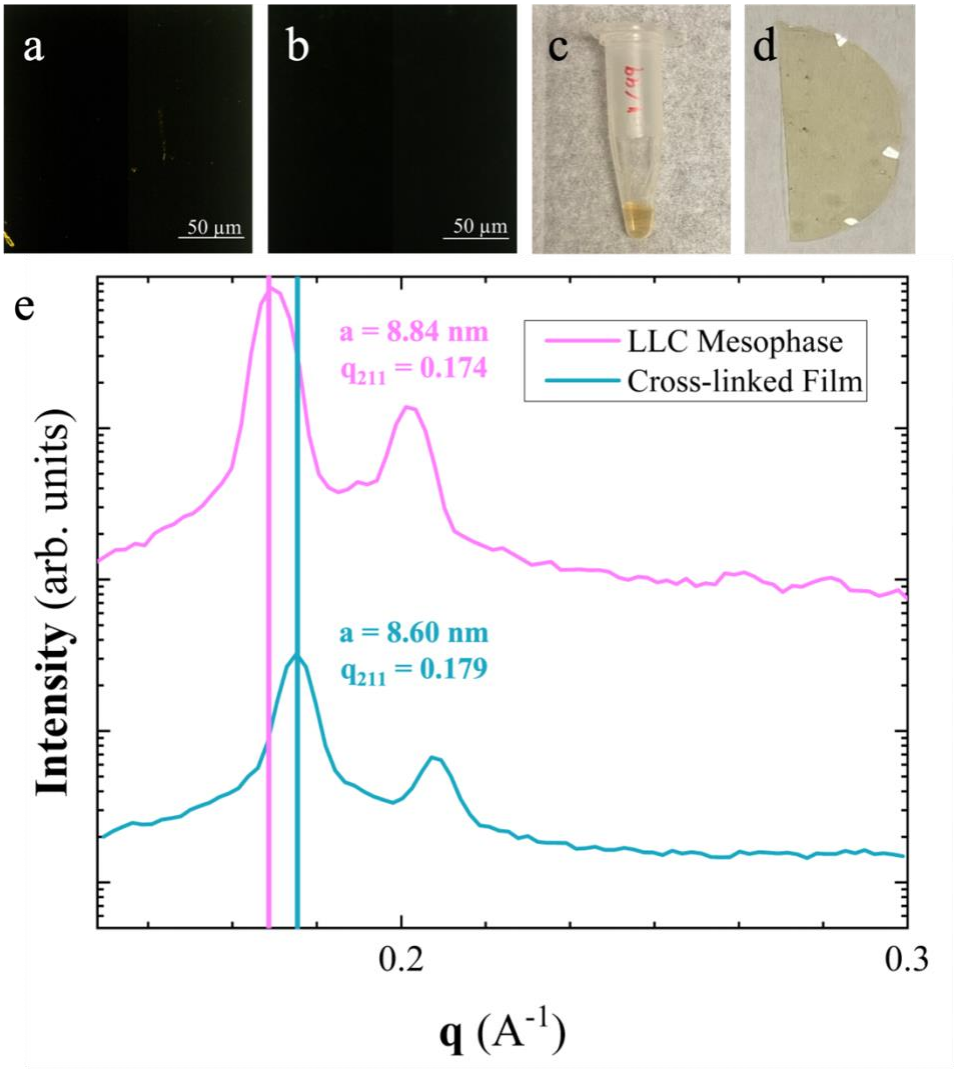

Figure 5.2 PLM micrographs of (a) the monomer mesophase and (b) a dry polymer film observed between crossed polarizers; (c) photo of the monomer mesophase blend pre-polymerization and (d) photo of the resulting cross-linked gyroid polymer film; and (e) representative SAXS spectra of the monomer mesophase and cross-linked polymer films fabricated from 87.5/11.5/1.0 (w/w/w) monomer blend (**6** + **8**) / water / DMPA.

The spiropyran-doped gyroid-phase polymer films described above were initially treated with aq. acid as the chromic stimulus. Acid exposure was the first choice of stimulus due to the excellent acid stability of cross-linked gyroid films of **6**[14] and the availability of commercial aq. HBr solutions. Also, the use of HBr would not result in counter-anion mixtures with the Br^- ions on monomers **6** and **8**, which would complicate structural analysis. Upon soaking the spiropyran-

doped films in aq. solutions of varying pH, UV-vis analysis confirmed effectively complete conversion of the **8SP** units to their **8M-HBr** form in the films (Figure 5.15). In addition, SAXS analysis confirmed retention of the gyroid nanostructure, with slight lattice swelling (i.e., an increase in unit cell parameter, *a*) observed in the wet vs. dry polymer films (Figure 5.16). Despite the evidence of lattice swelling upon exposure to aq. HBr solution, ^{1}H NMR studies of the polymer films soaked in D_2O (Figure 5.17) revealed no leaching of **8** from the bulk cross-linked network, thus indicating that **8** was successfully cross-linked within the bulk polymer film. Previous studies of gyroid-phase polymer films of **6** revealed no lattice swelling.[14] The lattice swelling of the present system is likely due to the presence of the spiropyran dopant monomer. We speculate that the otherwise densely cross-linked network is interrupted by the addition of non-cross-linking monomer **8**, the diene tail of which will only polymerize within the hydrophobic domains of the formed gyroid phase. This implies that around the hydrophilic domains (i.e., water nanopores) where the spiropyran moiety is likely situated, there is greater free volume since the spiropyran headgroup is not covalently linked to the walls of the hydrophilic domains. Due to the increased free volume near the hydrophilic pores, this system shows promise for functional behavior depending on the chemical state that the spiropyran monomer is in (i.e., **8SP** vs. **8M-HBr**) in response to an external stimulus (e.g., acid).

5.3.1 Effect of Spiropyran Acidochromism on the Gyroid Unit Cell of Cross-linked (**6** + **8**)

External stimuli can effectively mediate the chromic switching of the spiropyran-based monomer but are expected to have little impact on the overall integrity of the cross-linked material. Since the **8M-HBr** form has a positive charge and may possess various open-form states (the

general mechanism for conversion of **8SP** to **8M-HBr** and its *cis/trans* forms are provided in Section 5.5, Scheme 5.1),[20,26,27] it was expected that the environment of the aqueous domains of the nanoporous gyroid material would change upon exposure to acid. An excess of 0.422 M aq. HBr was used to promote the acidochromic shift of **8SP** to **8M-HBr** in a cross-linked gyroid-phase film suspended in solution. SAXS analysis revealed that the cross-linked films not only maintained the gyroid structure upon acidification but also exhibited a fully reversible change in their unit cell dimensions upon neutralization of the solution pH (Figure 5.3). Furthermore, the cross-linked films exhibited reversible color changes upon acidification and neutralization of their external solution pH (i.e., from pale yellow to vibrant red and the reverse, respectively).

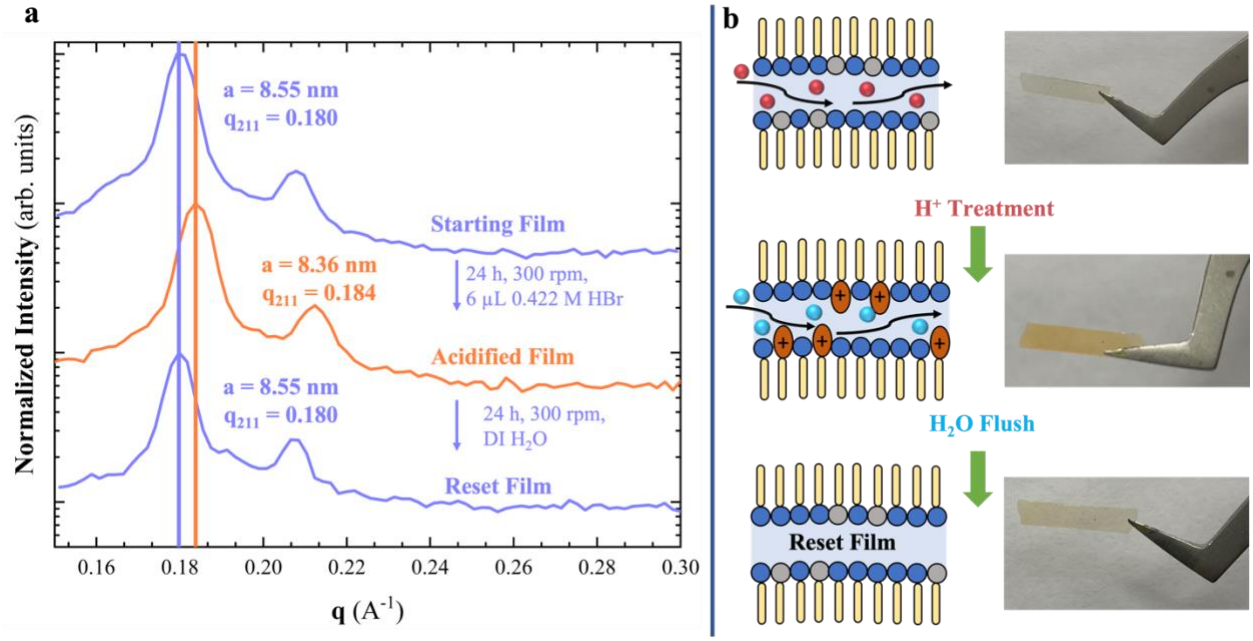

Figure 5.3 (a) SAXS spectra depicting the stimulus response of gyroid-phase polymer films of (**6** + **8**) to external aqueous solution pH with retention of the overall gyroid phase. Interestingly, a reversible shift in *a* was observed between gyroid-phase films soaked in neutral pH vs. acidic pH. (b) schematic representation and photos of a cross-linked gyroid film pre-acidification, post-acidification, and neutralization (red spheres = H^+ ions, light-blue spheres = water molecules, curved black arrows = direction of solvent/ion flow).

After confirming the stability of the gyroid phase during repeated acid exposure, the overall effect of calculated external solution acid concentration on the calculated relative pore diameter of the gyroid network was explored. Different pieces of the same original polymer film were exposed to various concentrations of acid and then analyzed by SAXS and photographed. Figure 5.4 shows that there is a clear dependence of the calculated pore diameter on the acidity of the solution. For gyroid polymer films made with 0.8 wt% or 1.2 wt% of monomer **8**, at the most acidic pH studied the calculated relative pore diameter change was approximately 5.0% smaller than the original calculated pore diameter. The rate of change of pore diameter with pH is dependent on the amount of **8** present in the system. In the absence of **8**, the pore size is insensitive to pH. However, for films with 0.8 and 1.2 wt% loading of **8**, the pore size shows a slope of 0.85 and 1.2 per pH unit increase, respectively. The differences in these coefficients are statistically meaningful (see Section 5.5 for full analysis). To our knowledge, a cross-linked Q-phase material that reversibly responds to external stimuli with unit cell dimensional changes has not been observed before.

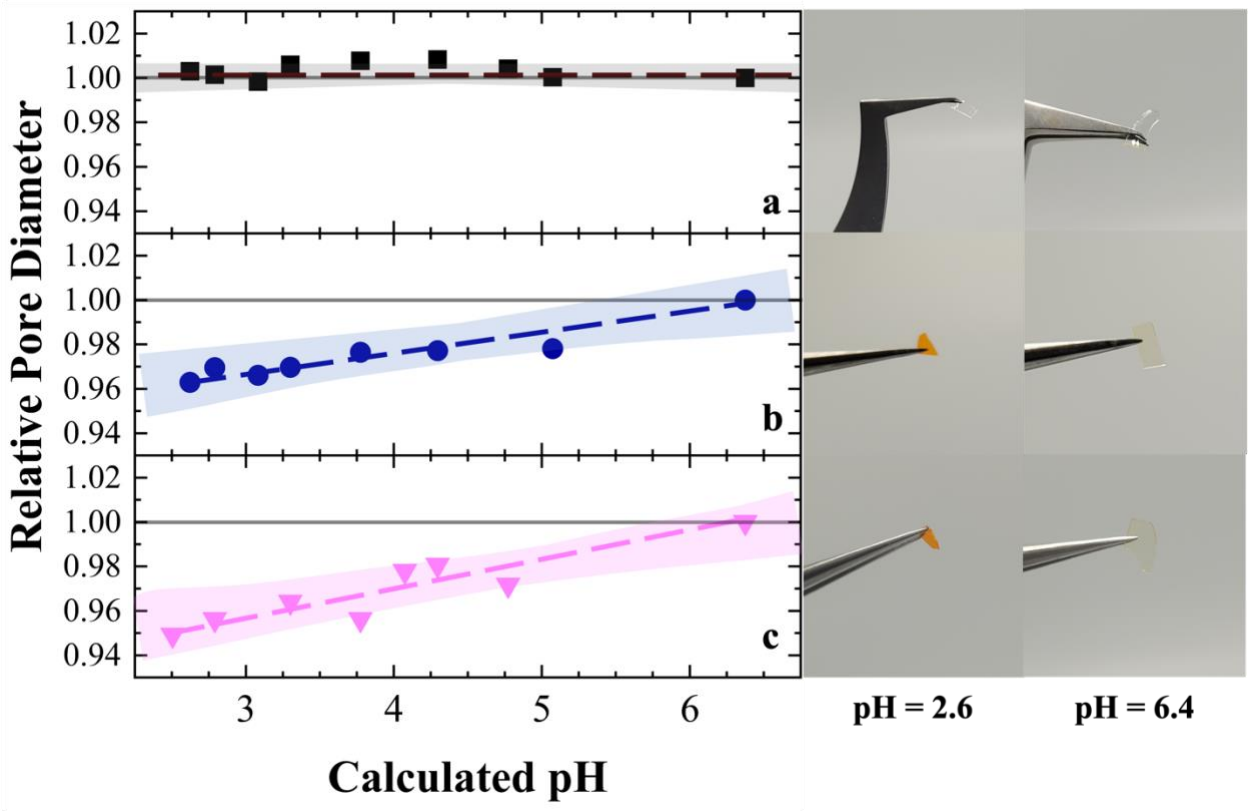

Figure 5.4 Response plot depicting the change in calculated relative pore diameter (based on observed unit cell lattice parameter changes) as a function of calculated pH, and corresponding photos of films exposed to low pH (ca. 2.6) and neutral pH (ca. 6.4) for: (a) an undoped gyroid polymer film of **6**; (b) a gyroid polymer film with 0.8 wt% **8**; and (c) a gyroid polymer film with 1.2 wt% **8**. Shaded areas in the plot represent the 95% confidence band. pH was calculated through volumetric addition of 0.422 M aq. HBr, with an instrumental random error of ± 0.05 μL. Pore diameter calculations are available in Section 5.5. Note: Photos are of different pieces of the same original film exposed to various concentrations of acid.

5.3.2 Changes in Vapor Transport through Bulk Films

The reversible response of the cross-linked gyroid unit cell under acidic conditions, coupled with an estimated shrinkage of 4.5–5.5% in calculated relative pore diameter, suggested that water vapor transport rates could be meaningfully affected by varying solution pH. Similar transitions have been observed in the construction of devices for acid vapor pH identification, although none have been embedded within a nanoporous gyroid LLC network.[29]

Pieces of a gyroid film containing 0.8 wt% **8** were sealed over the top of a glass-vial cell above a solution containing varying concentrations of aq. HCl. The rate of water vapor transport through the bulk films was then measured by observing the mass loss in the liquid reservoir over a period of two weeks at room temperature (22 °C). Each film was also checked to ensure the absence of pinhole defects; see the Section 5.5 for full experimental details. Pure de-ionized (DI) water (0 M HCl) and two aq. HCl solutions (1 M, and 2 M HCl) were chosen to indicate the most significant color changes in the films, which signified reaching a steady state by the films changing to a deep red color in the case of acidified samples. Figure 5.5 shows that for the aq. acidic solutions studied, the open-vial (no membrane film) water vapor loss rates were all similar (within statistical significance). However as the acid concentration increased, the steady-state vapor mass loss rate through the cells capped with spiropyran-doped films decreased: Specifically, non-acidic water vapor was lost at 83.0% of the rate for an open vial; 1 M aq. HCl vapor was lost at 76.1% of that for an open vial; and 2 M aq. HCl vapor was lost at 54.3% of that for an open vial. These water mass loss rates are competitive with commercially available, microporous supported membranes, such as polyacrylonitrile (Figure 5.19). The decrease in evaporation rate with respect to acid concentration is larger than expected for an approximate 4–5% decrease in calculated pore diameter for an *Ia3d* gyroid space group.[14,28,30] Upon exposure to low-pH water vapor, all the **8SP** groups in the film will have reacted to their **8M-HBr** form. We believe that further electrostatic interactions may also be taking place between the **8M-HBr** groups in the films and the HCl in the water vapor, further slowing diffusion once a steady state is reached. In summary, these spiropyran-doped gyroid networks can effectively transport water vapor; act as a color indicator for acid in the permeating water vapor; and alter the vapor transport rate as a function of the water vapor acidity.

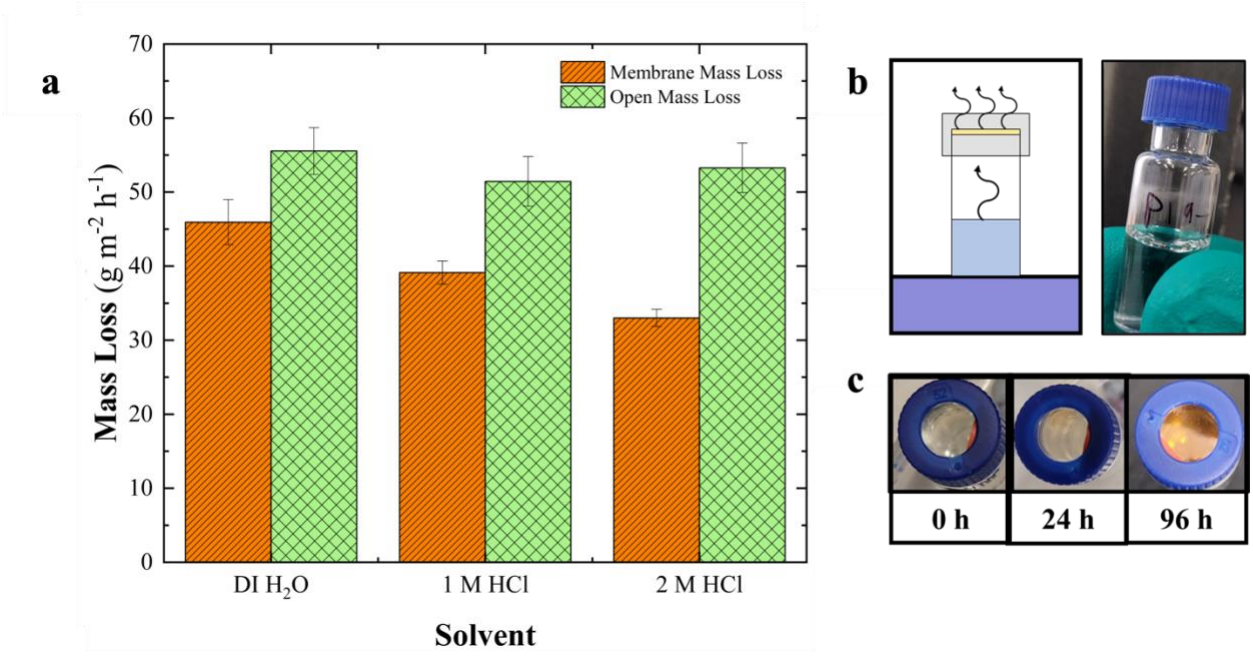

Figure 5.5 (a) Instantaneous mass flow rates (N = 10–14) at room temperature (22 °C) for film vapor cells in a desiccator filled with Drierite®, compared to cells that were left open (i.e., open vials). Thicknesses of the bulk gyroid polymer films of (**6** + **8**) tested in each experiment: DI H_2O: 0.135 μm; 1 M aq. HCl: 0.140 μm; 2 M aq. HCl: 0.138 μm. Error bars represent ± 1 standard deviation; (b) schematic representation of the experimental setup for vapor transport experiments; (c) color of film for at start of experiment with 2 M aq. HCl (0 h), first observation of significant color change in film (24 h), and at steady state (96 h).

5.3.3 Preliminary Studies of UV-light-mediated Pb^{2+} Ion Uptake in Bulk Gyroid Films of Cross-linked (**6** + **8**)

Spiropyran groups are also known to undergo UV-light-induced isomerization to the zwitterionic, non-protonated merocyanine form (i.e., **8M** for monomer **8**), without need for added acid.[18,20,24] The colored merocyanine form can also isomerize back to the uncharged spiropyran form upon irradiation with visible light (see Section 5.5, Scheme 5.2 and Figure 5.20 for structural details).[18,20,24] The zwitterionic merocyanine isomer has been incorporated onto a range of materials and used for metal ion chelation,[32-35] amino acid transport,[36] or simple logic gate operations.[37] Based on these prior studies, we designed an initial study to probe for a chromic

response of the gyroid polymer films of (**6** + **8**) upon exposure to aq. Pb^{2+} ions and UV light. Figure 5.6 depicts the overall results of this experiment. The merocyanine coloration was only observed when a piece of the spiropyran-doped gyroid polymer was soaked in water, exposed to aq. Pb^{2+} ions, and subjected to 365-nm light for 5 h at 22 °C. Pb^{2+} ions were chosen because literature studies have shown that Pb^{2+} ions have the highest binding affinity to the phenolate unit on the merocyanine isomer.[33,34] Control experiments revealed that UV light exposure or aq. Pb^{2+} ions alone were not enough to trigger an observable chromic response in the gyroid films of (**6** + **8**). Furthermore, Figure 5.6d shows that the gyroid phase of the films was retained in each case. Despite prolonged exposure of these films to DI H_2O and intense visible light irradiation, the merocyanine coloration was not observed to revert to the colorless spiropyran form. These results indicate that upon UV irradiation, this spiropyran-based nanoporous material acts as an effective trap for Pb^{2+}ions and the tightly bound Pb^{2+} ions stabilize the generated merocyanine form within the bulk polymer.

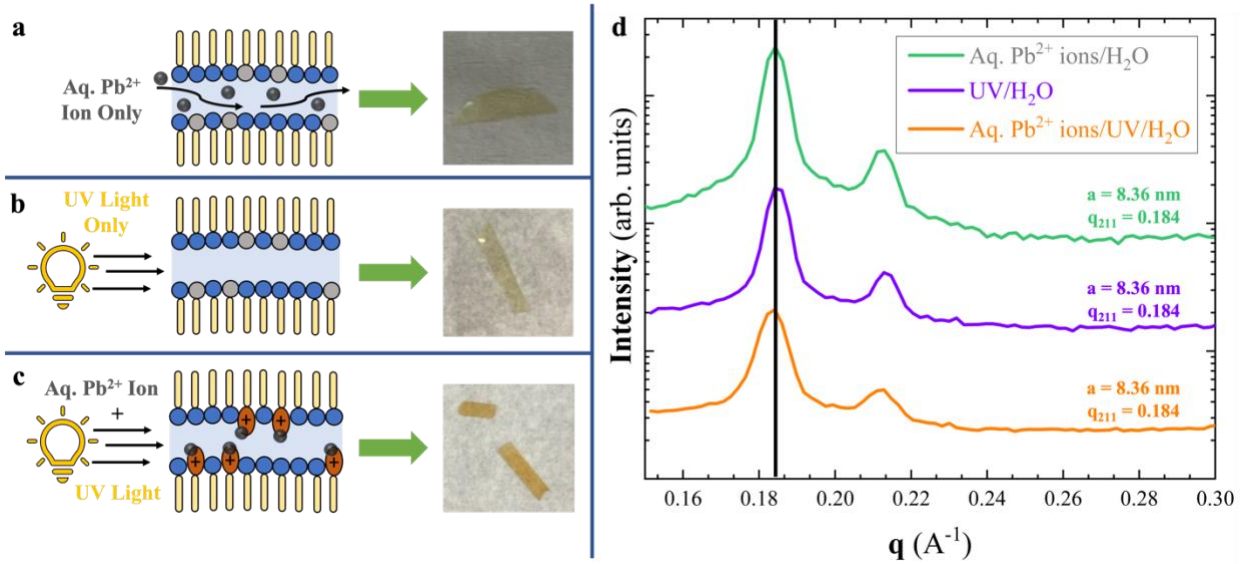

Figure 5.6 Schematics and photos of gyroid polymer films of (**6** + **8**) depicting: (a) lack of merocyanine formation upon exposure to aq. Pb^{2+} ions and water only; (b) lack of merocyanine formation upon exposure to UV light and water only; (c) merocyanine formation upon exposure to aq. Pb^{2+} ions, UV light, and water (black spheres = Pb^{2+} ions); and (d) SAXS spectra confirming retention of the gyroid phase in the polymer films upon exposure to the combinations of stimuli listed above.

5.4 Conclusion

In summary, we have synthesized a functional bicontinuous gyroid polymer network material that responds to multiple external stimuli with retention of the porous nanostructure. This system consists of a small amount of a novel spiropyran-containing dopant monomer (**8**) that upon blending and cross-linking with a previously reported gyroid-phase-forming LLC monomer (**6**) yields a stimuli-responsive gyroid-type Q_I network. Bulk films of this nanoporous polymer retain the gyroid structure while reversibly responding to changes in external solution and vapor pH via changes in color and unit cell dimensions as the spiropyran groups near the nanopores interconvert to their protonated-merocyanine form. This behavior allows the material to self-modulate its transport properties in situations such as diffusion and detection of HCl vapor. Upon UV irradiation, the spiropyran groups can also photo-isomerize to the colored unprotonated-

merocyanine form and irreversibly bind with aq. Pb^{2+} ions, thereby allowing the polymer to act as a colorimetric sorbent for this metal ion.

We are currently exploring ways to fabricate this unique material into supported thin films and investigating methods to expand the range of its responsive capabilities for applications. For example, we believe that by altering the monomer composition and/or temperature to access other LLC mesophases of membrane interest (e.g., the H_I phase)[38-40] or by reducing the thickness of the original gyroid films, new molecular-size-selective film materials can be developed that have the intrinsic ability to visually detect and restrict the flow of hazardous vapors of interest for breathable chemical vapor barrier applications.[4,5] Further work will also include probing the phase space of the (**6** + **8**) system to increase the loading of the spiropyran monomer dopant tolerated within the gyroid phase and possibly enhance the unit cell constriction properties of the Q networks. Finally, we plan to investigate the selectivity, uptake capacity, and reversibility of the UV-induced merocyanine form of this material to bind with different metal cations, in addition to Pb^{2+}. Chemical modification and tuning of this system may allow future development of a reversible ion-uptake system in which cations of interest can be reversibly complexed within the network upon external light exposure.

5.5 Supporting Information

5.5.1 Instrumentation

NMR spectra were obtained using a Bruker Avance-III 300 NMR spectrometer (300 MHz for ^1H, 75 MHz for ^{13}C). Chemical shifts are reported in parts per million relative to the solvent residual signal ($CDCl_3$, δ_H = 7.26 ppm, δ_C = 77.16 ppm). FTIR spectra (neat) were recorded using an Agilent Cary 630 FTIR instrument single-reflection horizontal ATR accessory with a diamond

crystal. The high-resolution mass spectra were obtained on a Waters SYNAPT G2 High-Definition Mass Spectrometry System at the University of Colorado Boulder Central Analytical Mass Spectrometry Facility. Lyotropic liquid-crystalline (LLC) mixtures were homogenized, as needed, using an IEC Centra-CL2 centrifuge. Elemental analysis was performed by Galbraith Laboratories, Inc. High-resolution SAXS spectra obtained on samples in vacuo were measured using a Xenocs Xeuss 2.0 system in the Dual Source and Environmental X-ray Scattering (DEXS) Facility at the University of Pennsylvania. For this Xenocs Xeuss 2.0 system, a GeniX3D Cu source with a wavelength of $\lambda = 1.54$ Å was used, with a sample-to-detector distances of 363 mm and 1210 mm. Samples were measured independently to ensure equivalent exposure to vacuum. Silver behenate was used as a standard for calibrating the SAXS sample-to-detector distance, and film samples were packed between Kapton windows. Foxtrot software was used for azimuthal integration of scattering patterns into 1-D plots of scattering intensity (I) vs. q, where $q = 4\pi\sin(\theta)/\lambda$ and the scattering angle is 2θ. Lower-resolution SAXS spectra for samples under ambient conditions were measured using a Rigaku S-Max-3000 instrument configured with Cu K_α radiation source with a wavelength of $\lambda = 1.54$ Å and an accessible range of scattering vectors (q) from 0.015 to 0.25 $Å^{-1}$ in the Osuji group at the University of Pennsylvania. Polarized light microscopy (PLM) studies were performed at the University of Colorado Boulder using a Leica DMRXP polarizing light microscope equipped with a Q-Imaging MicroPublisher 3.3 RTV digital camera, a Linkam LTS 350 thermal stage, and a Linkam CI 94 temperature controller. Automatic temperature profiles and image captures were performed using Linkam Linksys32 software. Radical photopolymerizations at the University of Colorado Boulder were conducted using a Spectroline XX-15A 365 nm UV lamp (8.5 mW cm^{-2} at the sample surface). UV light fluxes at the sample surface were measured using a Spectroline DCR-100X digital radiometer equipped

with a DIX-365 UV-A sensor. Radical photopolymerizations at the University of Pennsylvania were conducted using a 100-W Sunspot SM system. The lamp emission spectrum was distributed in the wavelength range between 250–450 nm, with peak intensity at 365 nm. Light irradiation of samples for the **8SP** to **8M** photo-isomerization studies were performed using an OmniCure® Series 1000 mercury arc lamp with a 250–450 nm filter option (100 W output). SEM images for porous supports were captured using a FEI Quanta 600 Mark II Environmental Scanning Electron Microscope, with access provided by the Singh Center at the University of Pennsylvania. UV-visible absorption spectra were taken using a HP8452A diode array UV-Vis Spectrometer (equipped with a 1 cm quartz cuvette for solution phase measurements and a 1 cm custom-made quartz film holder for polymer film measurements) in the Damrauer research group in the Dept. of Chemistry at the University of Colorado Boulder.

5.5.2 Materials and General Procedures

Chromium(VI) oxide, pyridine, *tert*-butyllithium (1.6 M in pentane), hydrogen bromide (48 wt. % in H_2O), borane-tetrahydrofuran complex solution (1.0 M in THF), ω-pentadecalactone (98%), 2,2-dimethoxy-2-phenylacetophenone (99%), sulfuric acid, triethanolamine (98%), anhydrous *N*,*N*-dimethylformamide (99.8%), and Florisil® (<200 mesh) were purchased from Sigma-Aldrich and used as received unless otherwise specified. *N,N,N',N',*-Tetramethylethylenediamine (98%), allyltrimethylsilane (98%), and 2-isopropoxy-4,4,5,5-tetramethyl-1,3,2-dioxaborolane (98%) were purchased from TCI America and used as received unless otherwise specified. 1',3',3'-Trimethyl-6-hydroxyspiro(2*H*-1-benzopyran-2,2'-indoline) (99%) was purchased from VWR and used as received unless otherwise specified. Aluminum oxide (neutral, act. I, 50-200 μm) and silica gel (normal-phase, 200 x 400 mesh) were purchased

from Sorbent Technologies. Celite™ 545, hydrochloric acid, anhydrous magnesium sulfate, anhydrous potassium carbonate, sodium chloride, and sodium hydroxide (all ACS Reagents) were purchased from Fisher Scientific and used as received. All reaction solvents were obtained from Sigma-Aldrich and were purified/dehydrated via vacuum distillation and then de-gassed by repeated freeze-pump-thaw cycles and stored under Ar. All chemical syntheses were carried out under a dry Ar atmosphere using standard Schlenk line techniques unless otherwise noted. Polyacrylonitrile (PAN) membrane supported on porous PET was purchased from Sterlitech.

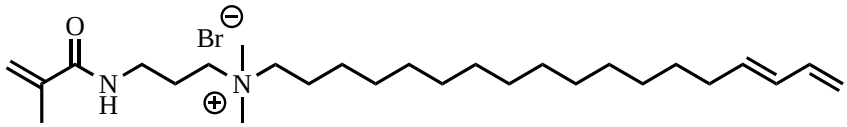

6

Figure 5.7 Structure of previously reported, intrinsically cross-linkable Q-phase-forming LLC monomer **6**.

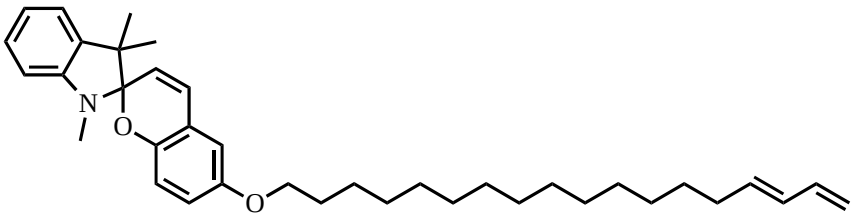

8SP

(*E*)-1',3',3'-Trimethyl-6-(octadeca-15,17-dien-1-yloxy)spiro[chromene-2,2'-indoline] (8SP). 18-Bromooctadeca-1,3-diene (0.6175 g, 1.875 mmol, 1.100 equiv.), K_2CO_3 (1.178 g, 8.523 mmol, 5.002 equiv.) and 1',3',3'-trimethyl-6-hydroxyspiro(2*H*-1-benzopyran-2,2'-indoline) (0.5000 g, 1.704 mmol, 1.000 equiv.) were suspended in DMF (40 mL) in a 125-mL Schlenk flask equipped with a stir bar. The solution was stirred at 80 °C for 20 h in the dark. The contents of the Schlenk flask were cooled to RT and diluted in a mixture of EtOAc and deionized (DI) H_2O

(100 mL each). The organic phase was separated, and the aqueous phase was extracted with EtOAc (3 x 75 mL). The combined EtOAc extracts were extracted with DI H_2O (2 x 100 mL), saturated aq. NH_4Cl (2 x 100 mL), and brine (2 x 100 mL). The combined EtOAc extracts were dried over anhydrous $MgSO_4$, filtered through a pad of celite, and concentrated by rotary evaporation to afford the product as a light-brown solid (0.8342 g, 90%). ^1H NMR (300 MHz, $CDCl_3$): δ = 7.22 – 7.03 (m, 2H), 6.88 – 6.76 (m, 2H), 6.70 – 6.58 (m, 3H), 6.51 (dd, *J* = 0.87, 7.68 Hz, 1H), 6.40 – 6.23 (m, 1H), 6.11 – 5.97 (m, 1H), 5.81 – 5.61 (m, 2H), 5.14 – 4.90 (m, 2H), 3.88 (t, *J* = 6.57 Hz, 2H), 2.72 (s, 3H), 2.07 (q, *J* = 7.06 Hz, 2H), 1.73 (p, 2H), 1.52 – 1.21 (m, 29H), 1.16 (s, 3H). ^{13}C NMR (75 MHz, $CDCl_3$): δ = 137.52, 135.83, 130.96, 129.48, 127.68, 121.62, 120.30, 119.18, 119.12, 116.07, 115.58, 114.70, 112.37, 106.87, 77.36, 68.83, 51.74, 32.71, 29.81, 29.75, 29.65, 29.56, 29.34, 29.09, 26.22, 26.00, 20.39. FTIR (cm^{-1}, neat): 2915, 2848, 1610, 1487, 1461, 1252, 1185, 1021, 1001, 961, 741. UV-visible peak maxima (nm, in 1:1 (v/v) acetone/CH_2Cl_2): 300, 337. HRMS (m/z, ESI) $[M + H]^+$ calcd: 542.3998; found: 542.4001. Anal. calcd for $C_{37}H_{51}NO_2$: C, 82.02, H, 9.49; N, 2.59; found: C, 81.76; H, 9.80; N, 2.53.

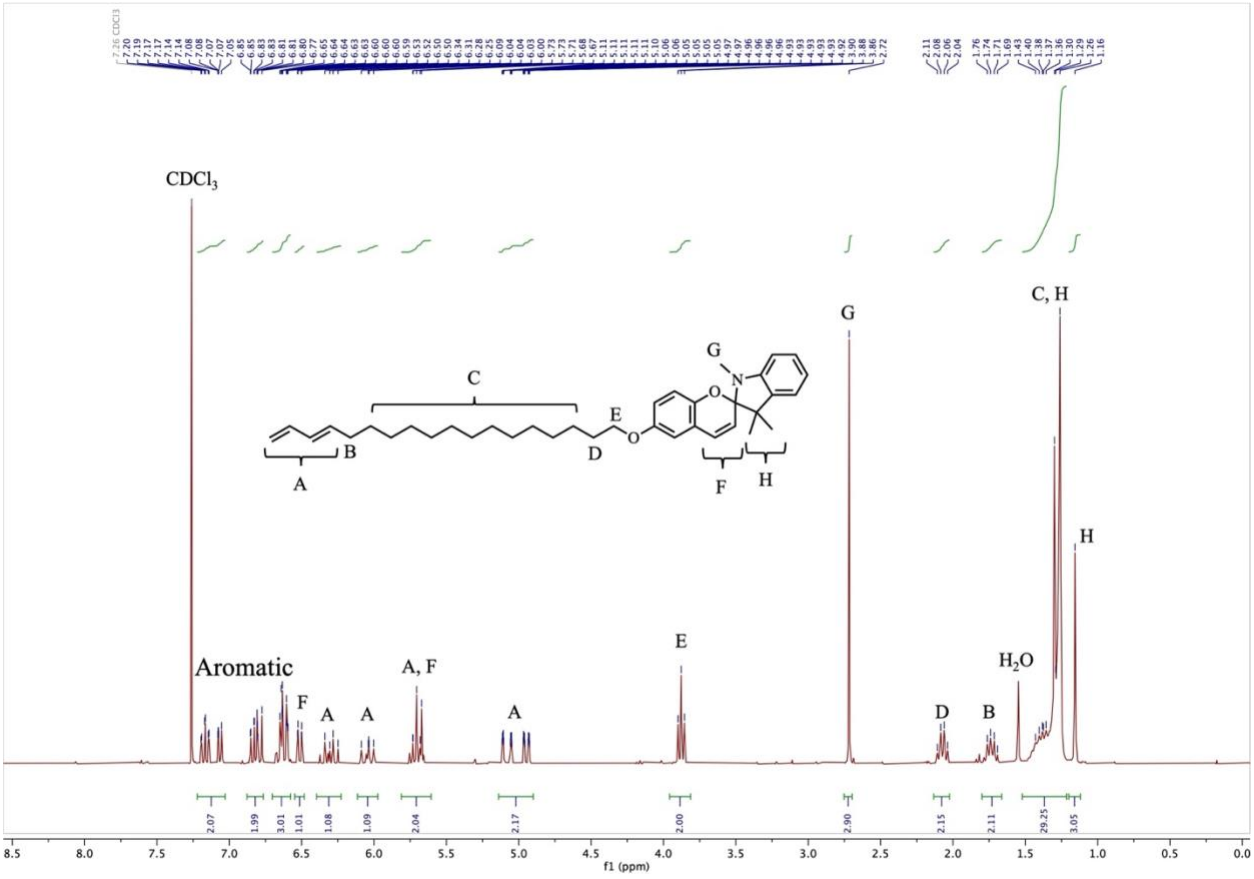

Figure 5.8 ^{1}H NMR spectrum of monomer **8SP** in $CDCl_3$.

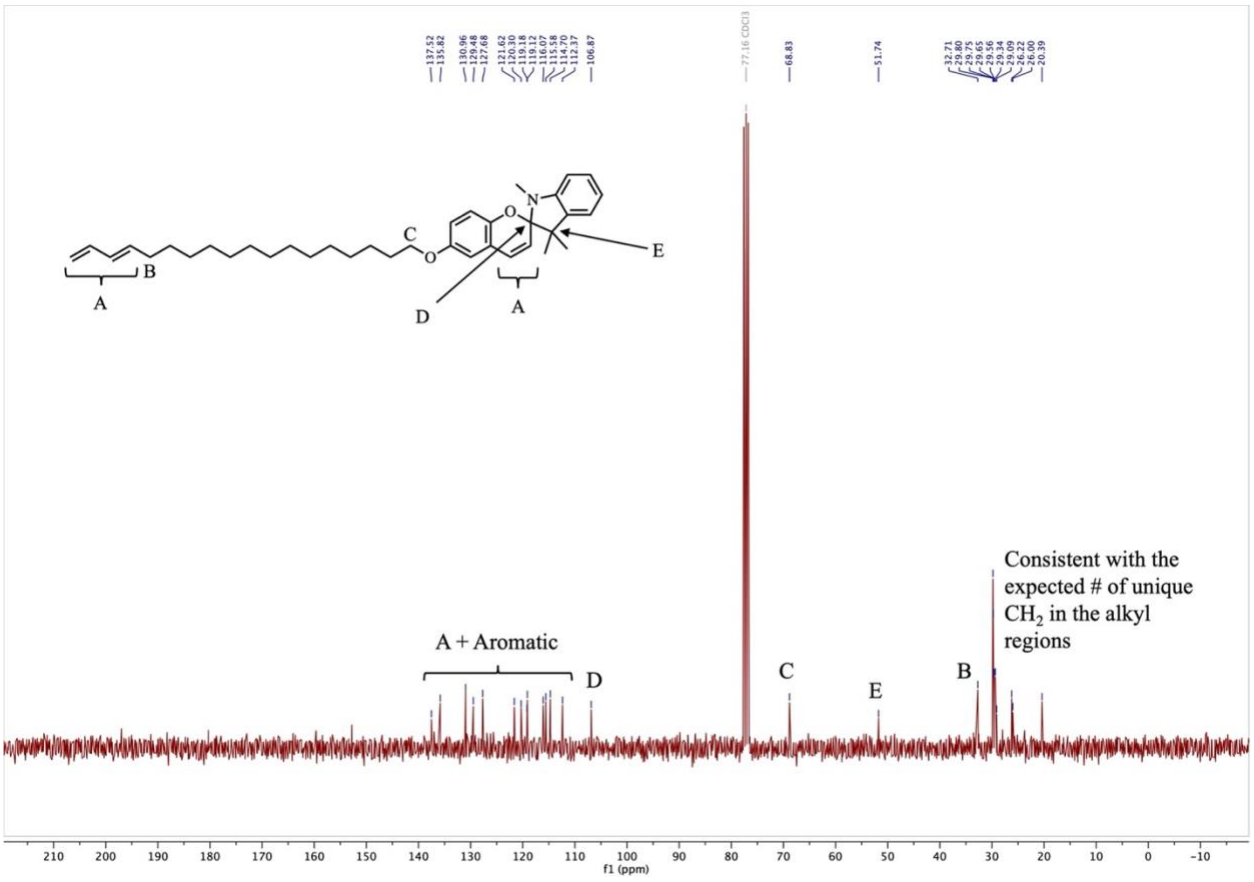

Figure 5.9 ^{13}C NMR spectrum of monomer **8SP** in $CDCl_3$.

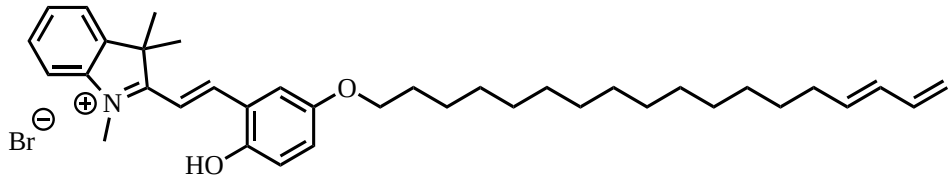

8M-HBr

2-((*Z*)-2-Hydroxy-5-(((*E*)-octadeca-15,17-dien-1-yl)oxy)styryl)-1,3,3-trimethyl-3*H*-indol-1-ium bromide (8M-HBr). *The following procedure was performed in air with materials used as purchased.* Monomer **8SP** (0.1072 g, 0.1979 mmol, 1.000 equiv.) was dissolved in a minimal amount of acetone. An equimolar amount of 0.422 M aq. HBr solution (0.4688 mL, 0.1978 mmol, 1.000 equiv.) was added. Upon addition of acid, the light brown solution changed to a vibrant orange-red and a precipitate was formed. CH_2Cl_2 was added until all solids were

dissolved yielding a clear red solution. The solution was allowed to evaporate overnight at RT. The residual powder was then dried in vacuo to give **8M-HBr** as a vibrant orange-red powder. Note: HBr was chosen as the strong acid used to promote the acidochromic switch of **8SP** to **8M-HBr** to ensure only bromide counterions were present in the samples (i.e., no anion mixtures) for the NMR and blending studies with **6**. ^{1}H NMR (300 MHz, DMSO-d_6): δ = 10.64 (s, 1H), 8.48 (d, J = 16.42 Hz, 1H), 7.99 – 7.77 (m, 2H), 7.79 – 7.54 (m, 4H), 7.12 (dd, J = 2.96, 9.02 Hz, 1H), 6.97 (d, J = 9.01 Hz, 1H), 6.44 – 6.20 (m, 1H), 6.12 – 5.93 (m, 1H), 5.81 – 5.63 (m, 1H), 5.18 – 4.85 (m, 2H), 4.10 (s, 3H), 3.99 (t, J = 6.35 Hz, 2H), 2.14 – 1.98 (m, 2H), 1.75 (s, 8H), 1.24 (s, 24H). ^{13}C NMR (75 MHz, DMSO-d_6): δ = 152.01, 137.24, 135.31, 130.88, 115.10, 68.20, 51.84, 34.30, 31.89, 29.03, 28.82, 28.60, 26.03, 25.60. IR (cm^{-1}, neat): 3034, 2919, 2851, 1580, 1524, 1498, 1476, 1308, 1162, 1002, 898, 776. UV-visible peak maxima (nm, in 1:1 (v/v) acetone/CH_2Cl_2): 378, 474. HRMS (m/z, ESI) $[M]^+$ calcd: 542.3998; found, 542.4001. Anal. calcd for $C_{37}H_{52}NO_2Br$: C, 71.36; H, 8.42; N, 2.25; found: C, 71.37; H, 8.53; N, 2.21.

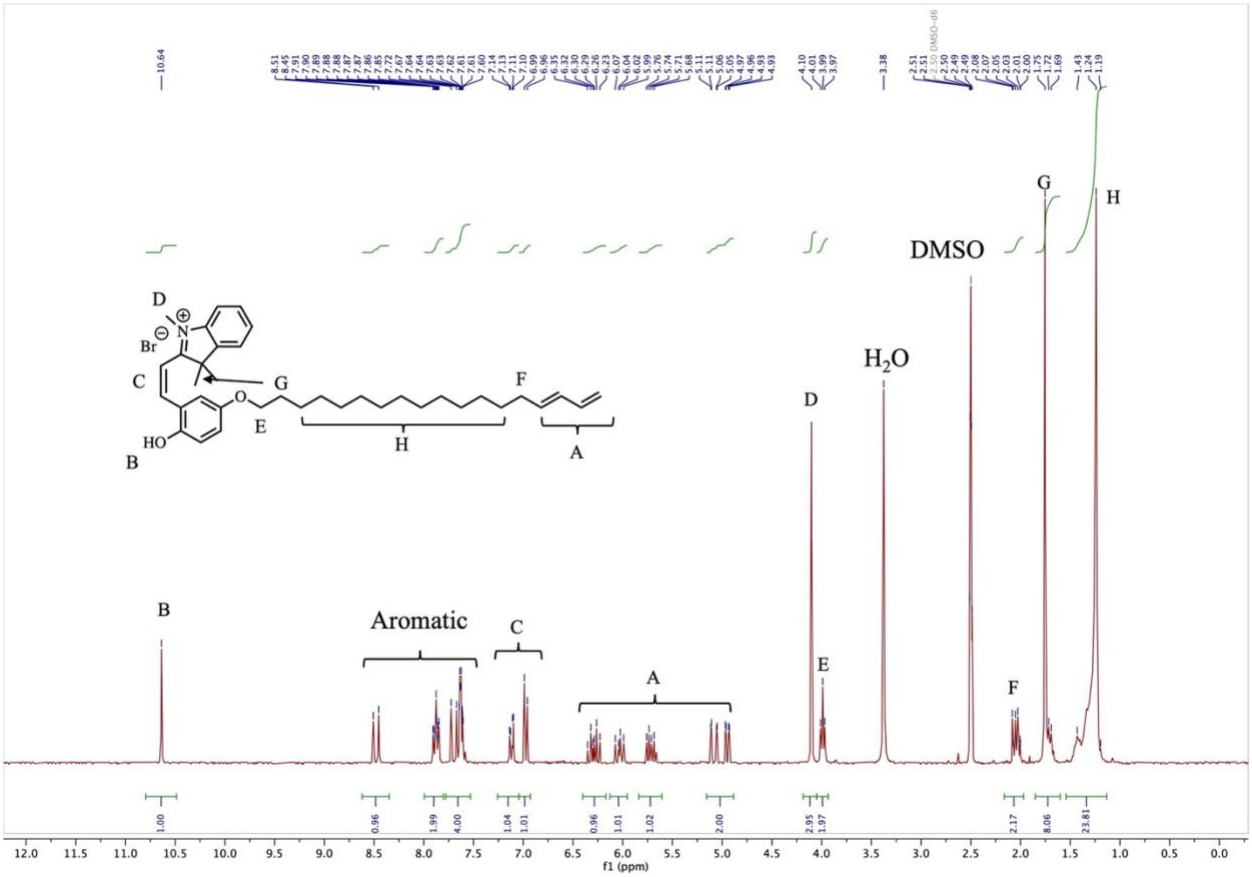

Figure 5.10 ^{1}H NMR spectrum of monomer **8M-HBr** in DMSO-d_6.

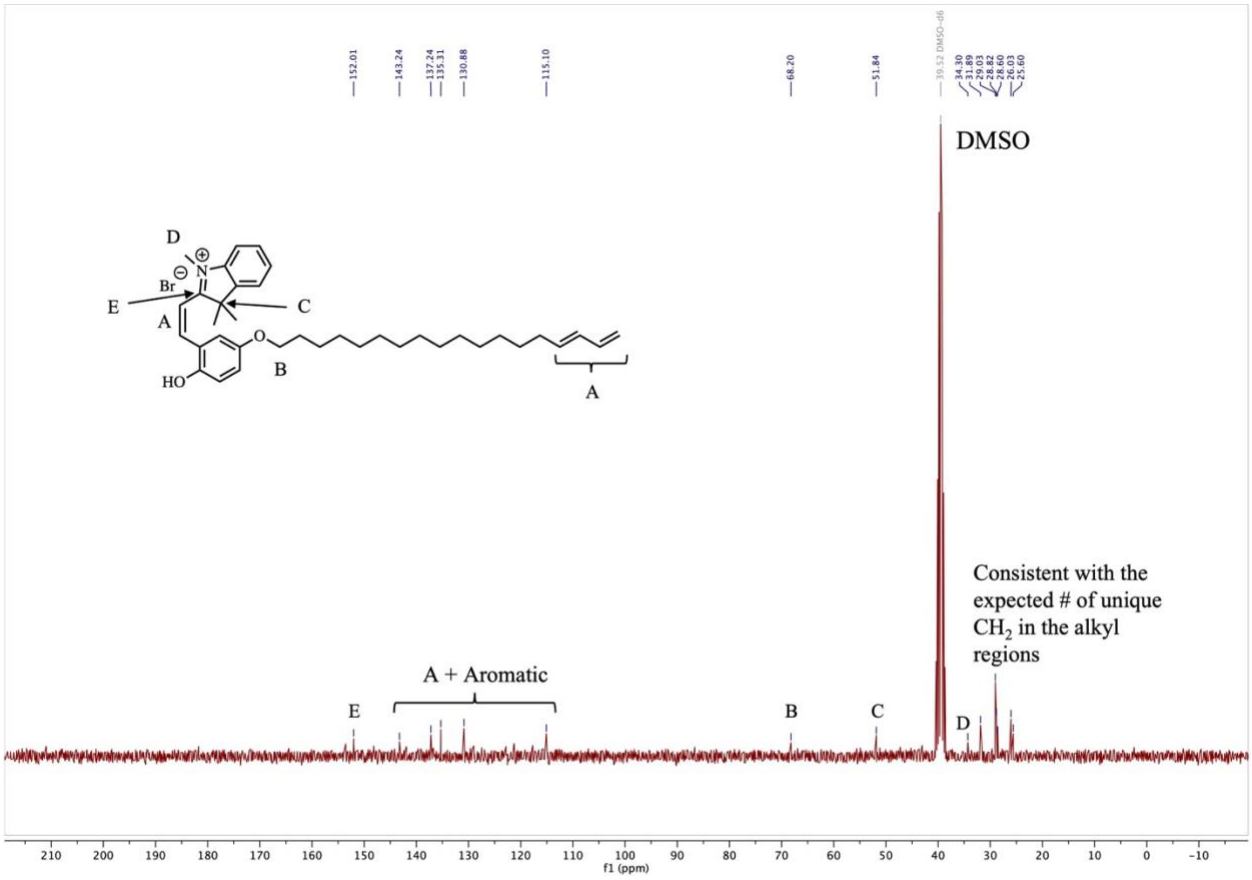

Figure 5.11 ^{13}C NMR spectrum of monomer **8M-HBr** in DMSO-*d*$_6$.

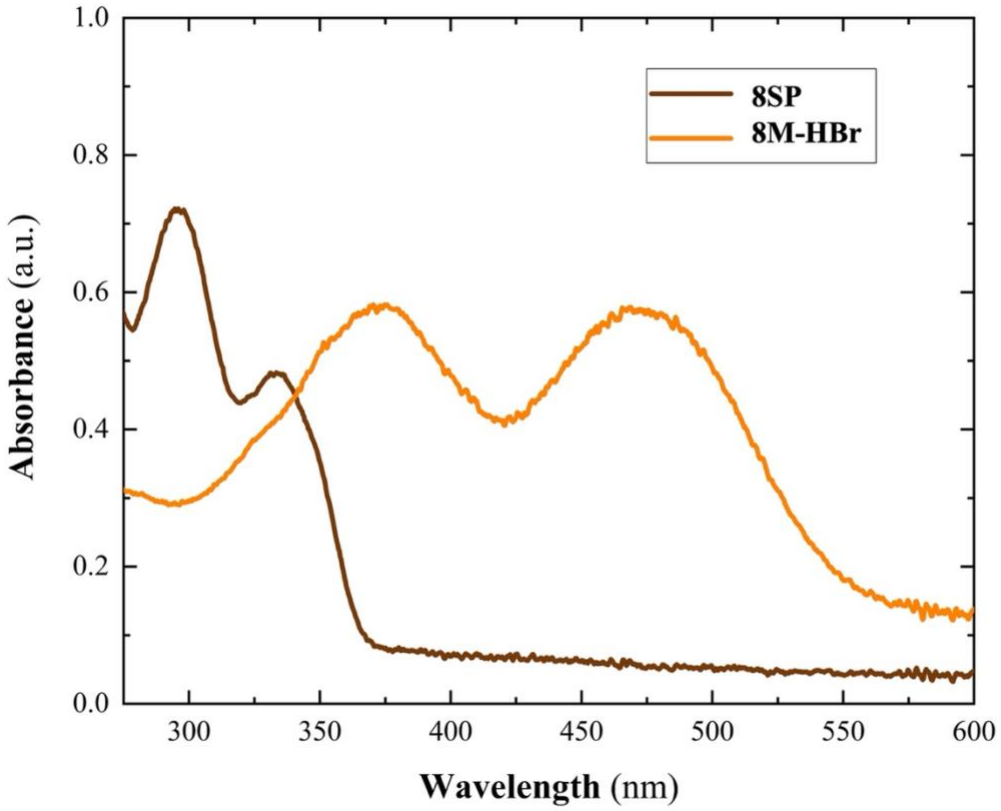

Figure 5.12 UV-visible absorption spectra of monomer **8SP** and separately monomer **8M-HBr** dissolved in 1:1 (v/v) acetone/CH_2Cl_2.

5.5.2.1 LLC Monomer Blending/Homogenization Prior to Q_I Monomer Mesophase Formation

Monomer **8** (in either the **8SP** or **8M-HBr** form) was added to a pre-tared 1.5-dram vial. The actual mass of **8** was recorded, and the vial containing **8** was tared. The required amount of **6** was calculated and then added to the vial. The mass of **6** was recorded, and the final weight percentages were calculated for **6** and **8**. The vial was then sealed and centrifuged at 4000 rpm for 10 min or until most of the solids were on the bottom of the vial. The resulting powder was then hand-mixed in air with a microspatula until homogeneous. The vial was sealed under an inert Ar atmosphere and allowed to equilibrate in the refrigerator (12 °C) overnight prior to use.

5.5.2.2 Preparation and Phase Identification of Gyroid-type Q_I-phase Blends of Monomers **6** + **8**

Radical photo-initiator 2,2-dimethoxy-2-phenylacetophenone (DMPA) (0.50 mg) was added to a pre-tared Eppendorf tube. A 10-μL gastight syringe was conditioned/cleaned first with acetone, then with DI water. DI water (5.75 mg) was then injected into the Eppendorf tube. The homogenized blend of monomers **6** + **8** (in either the **8SP** or **8M-HBr** form) (43.71 mg, prepared as described above) was carefully added to the tared Eppendorf tube, and the final mass of the monomer blend was recorded. The final weight percents were calculated to confirm that approximately a 1.0 DMPA / 11.5 DI H_2O / 87.5 monomers (**6** +1.0 wt% **8**) blend (w/w/w) was achieved. The Eppendorf tube was sealed and centrifuged at 4000 rpm for 30 min, and the mixture was then hand-mixed with a blunt needle making sure to not scrape the sides of the tube. The Eppendorf tube was then sealed and centrifuged at 4000 rpm for 1 h or until homogeneous.

Formation of a Q phase by the resulting (**6** + **8**) / water / DMPA mixture at RT (22 °C) was identified qualitatively via PLM analysis (i.e., observance of a black optical texture under cross polarizers) and quantitatively via SAXS analysis (i.e., observance of principal diffraction peaks in the ratio $1/\sqrt{6} : 1/\sqrt{8}$ indicative of Q and/or gyroid LLC phases).[1,4] In addition, the formed monomer mesophase was very viscous and completely optically transparent under normal light, both of which are also characteristic of Q LLC phases.[1,4] Since the major monomer in this mixture (**6**) was found to form a gyroid-type Q_I phase with added water and DMPA under similar conditions via partial phase diagram elucidation / structure characterization,[14] it can be assumed that the same type of Q phase is formed upon blending-in a small amount of monomer **8** (i.e., 0.5–1.2 wt% of **8** relative to **6**). Unfortunately, preliminary phase diagram elucidation of this (**6** + **8**) / water / DMPA system did not show the formation of a L phase. The presence of a central L phase would be needed to directly assign a Type I (normal) or II (inverted) phase configuration to the

observed gyroid-type Q phase, depending on whether the Q phase appears on the water-excessive or water-deficient side of the L phase.[1,14]

5.5.2.3 Fabrication of Bulk Gyroid Films of Cross-linked (**6** + **8**)

The gyroid-type Q_I-phase monomer mixture (prepared as described above) was sandwiched between two pieces of clean Mylar film, placed between two clamped fused silica plates. The sample was then placed in a chamber with nitrogen purge and then irradiated with 365 nm light for 3 h at RT (22 °C). After irradiation, a clean razor blade was then used to carefully remove the bulk film from the sandwiched Mylar sheets. FT-IR spectroscopy confirmed the near-complete conversion of the polymerizable groups (Figure 5.13). Retention of the Q_I phase in the resulting cross-linked polymer film was confirmed qualitatively via PLM and quantitatively via SAXS analysis as described in the previous section. (Note: Although both **8SP** or **8M-HBr** could be blended with **6** to form a stable gyroid phase, the coloration of the resulting cross-linked Q_I film indicated that the dominant dopant form was **8SP** instead of **8M-HBr**. The shift of **8M-HBr** to **8SP** during the film fabrication process was likely a result of the water used for mesophase formation diluting the acid previously used to promote the **8M-HBr** state.)

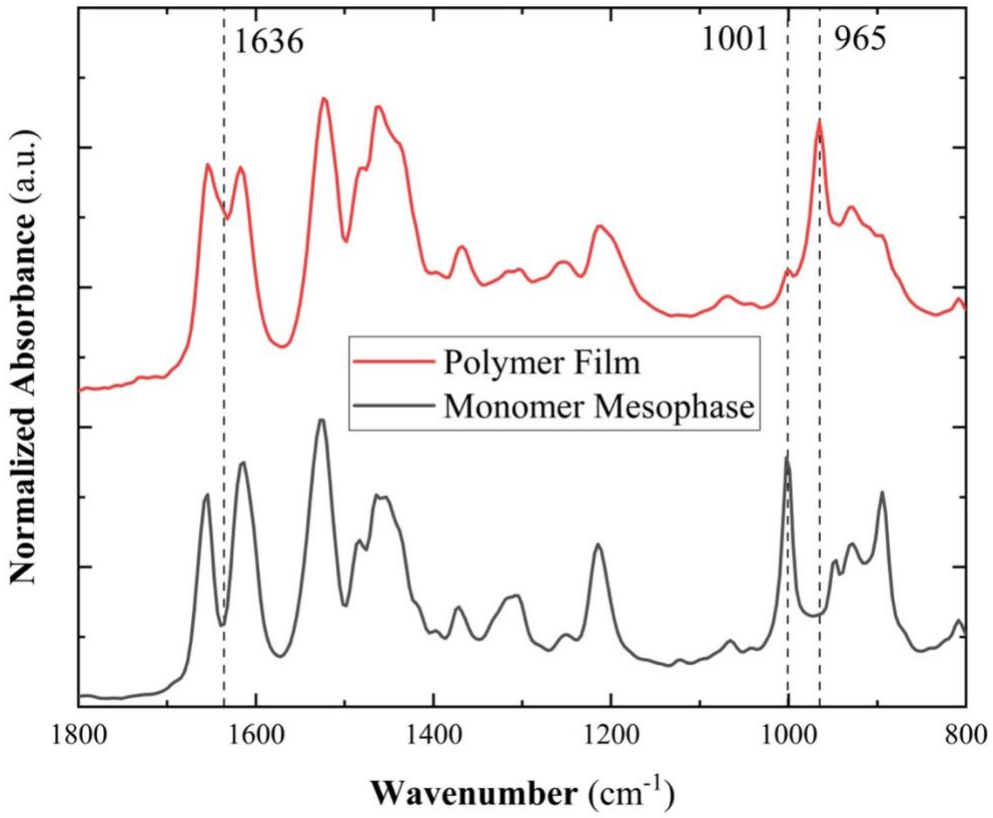

Figure 5.13 Representative FT-IR spectra showing that the polymerizable 1,3-diene tails on **6** and **8** exhibit near-quantitative conversion (disappearance of band at 1001 cm^{-1} and appearance of a new band at 965 cm^{-1}) and UV photo-initiated radical polymerization.[7] The relative increase in intensity of the 1636 cm^{-1} band indicates good conversion of the methacrylamide polymerizable group on **6**.

5.5.2.4 Probing the Thermal Stability of Bulk Gyroid Films of Cross-linked (**6** + **8**)

For temperature-dependent SAXS measurements, a cross-linked bulk gyroid film of (**6** + **8**) were prepared as described above and then placed on a Linkam heating stage (Model Number L-HFSX350). The stage was heated from 30 °C to 120 °C with a heating scan rate of 3 °C /min, 15 min equilibration / annealing time upon reaching the set temperature, followed by a 15-min SAXS capture time. SAXS spectra were obtained of the film sample at every 15 °C within the

temperature range. Figure 5.14 below shows the SAXS spectra of these heat-treated films, indicating that the gyroid structure is effectively unchanged and stable up to 120 °C. The slight shift in *a* value at higher temperatures is attributed to slight dehydration of the polymer film.

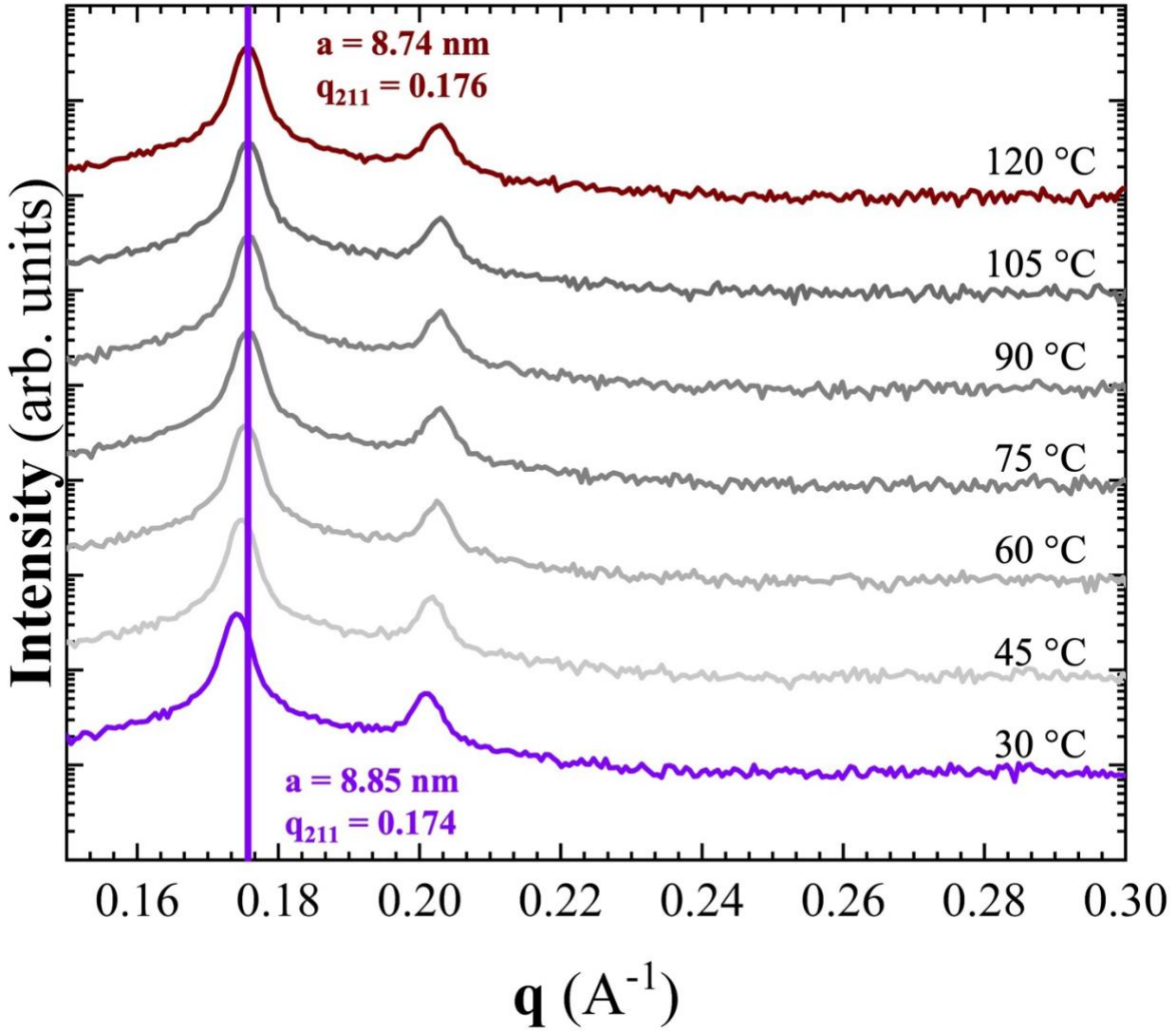

Figure 5.14 SAXS plots showing the stability of the gyroid nanostructure in a piece of bulk gyroid film of cross-linked (**6** + **8**) at elevated temperatures. The slight shift in *a* at higher temperatures is attributed to dehydration of the polymer film.

5.5.2.5 Probing the Acid Sensitivity and Response of Bulk Gyroid Films of Cross-linked (**6** + **8**)

Bulk cross-linked gyroid Q_I films of (**6** + **8**) (previously prepared as described above) were cut into ca. 1.0 mg strips and placed into 2.5 mL of DI water with 0.5–200 µL of 0.422 M aq. HBr added to the solution. The samples were then vortexed at 300 rpm for 12–24 h. The polymer film was gently removed from the vial and dried with a KimWipe for SAXS analysis.

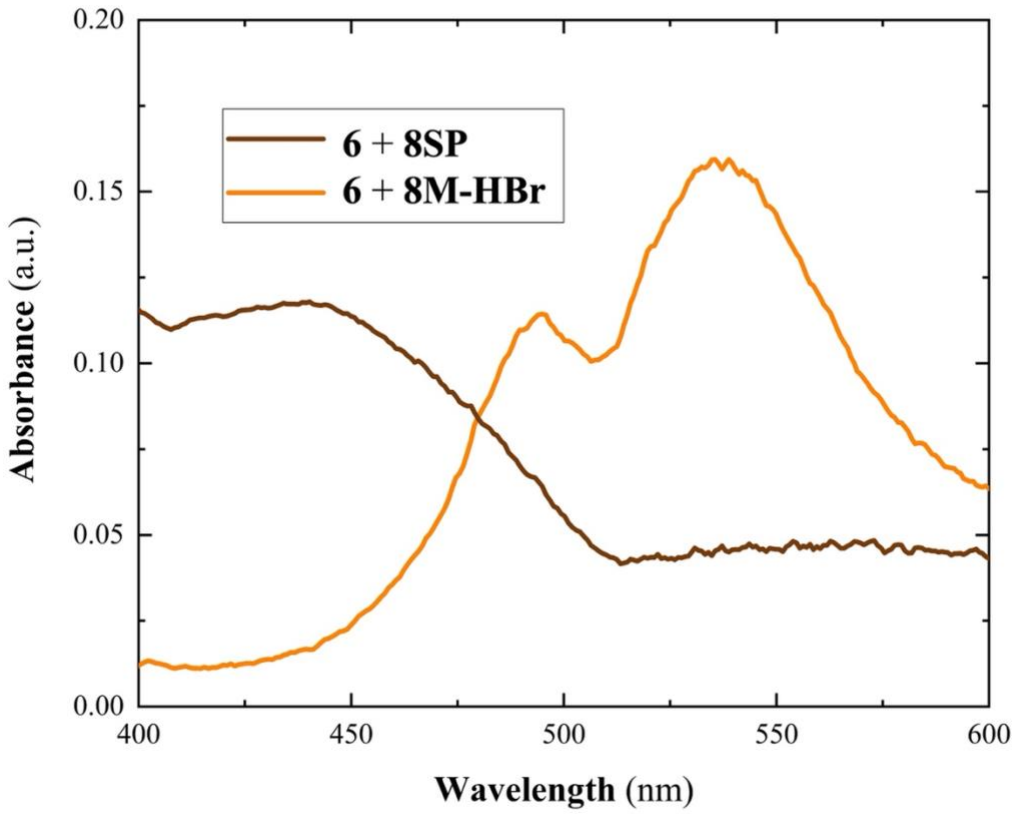

Figure 5.15 Typical UV-visible absorption spectra of a cross-linked bulk gyroid-phase film of (**6** + **8**) before and after exposure to aq. HBr solution. The full conversion of the spiropyran group (**8SP**) to the protonated-merocyanine form (**8M-HBr**) occurs after treatment with aqueous HBr.

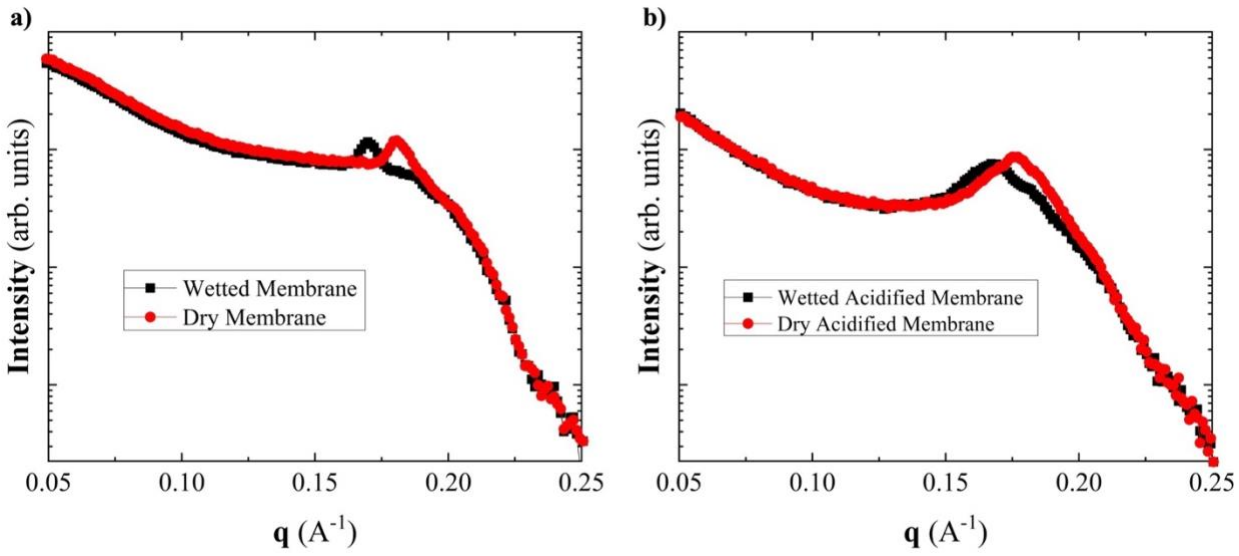

Figure 5.16 SAXS spectra of (a) a cross-linked gyroid-type Q_I film of (**6** + **8**) with no 0.422 M aq. HBr treatment, and (b) the same film after being treated with 0.422 M aq. HBr (all spectra taken under non-vacuum, ambient conditions).

5.5.2.6 Procedure for Determining Lack of Monomer Leaching and Reversibility of Spiropyran to Protonated-Merocyanine Conversion in Bulk Gyroid Films of Cross-linked (**6** + **8**)

To determine that no monomer **8** was leaching from the polymerized film, a previously acid-treated Q_I polymer film was suspended in deuterated water (pH = ca. 5) and vortexed at 150 rpm for 24 h. An aliquot of the solution was taken and ^{1}H NMR analysis of it suggested no leaching of either unreacted **6** or **8** from the polymer film had occurred (Figure 5.17).

Interestingly, after removing the Q_I polymer film from the D_2O, its appearance had reverted to its pre-acid-treated state (i.e., the uncharged spiropyran (**SP**) form). The same film was then suspended in water, the solution was acidified to pH ca. 0 with 0.422 M aq. HBr, and vortexed at 150 rpm for 24 h. The aqueous solution was decanted, and the film was removed and dried with a KimWipe. The appearance of the film had once again returned to its vibrant-orange HBr-

protonated-merocyanine state (**8M-HBr**), indicating that the spiropyran-merocyanine conversion is reversible when the films are suspended in solution.

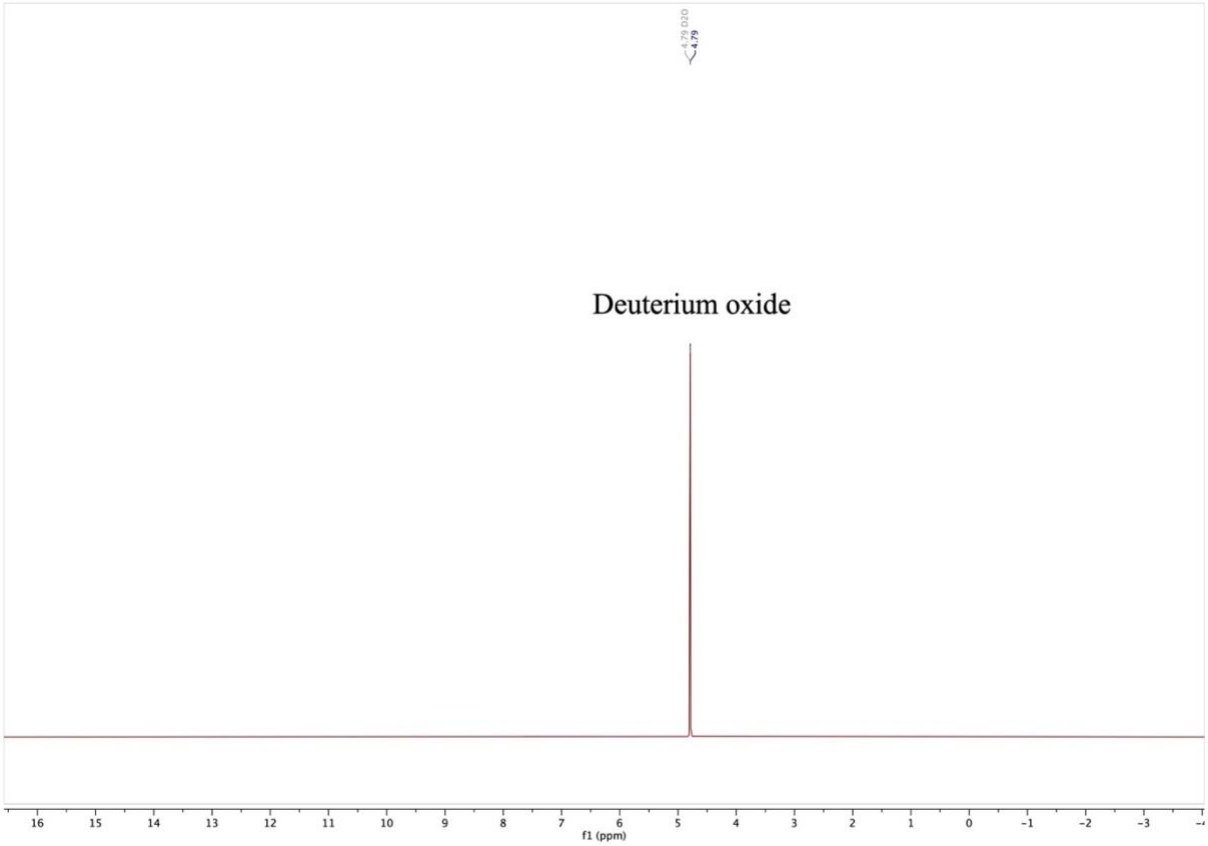

Figure 5.17 ^{1}H NMR spectrum of the D_2O supernatant after a cross-linked Q_I blend of (**6** + 1.0 wt% **8SP**) that was soaked in D_2O for 24 h at RT to probe for any leaching of unreacted **6** or **8SP** from the film.

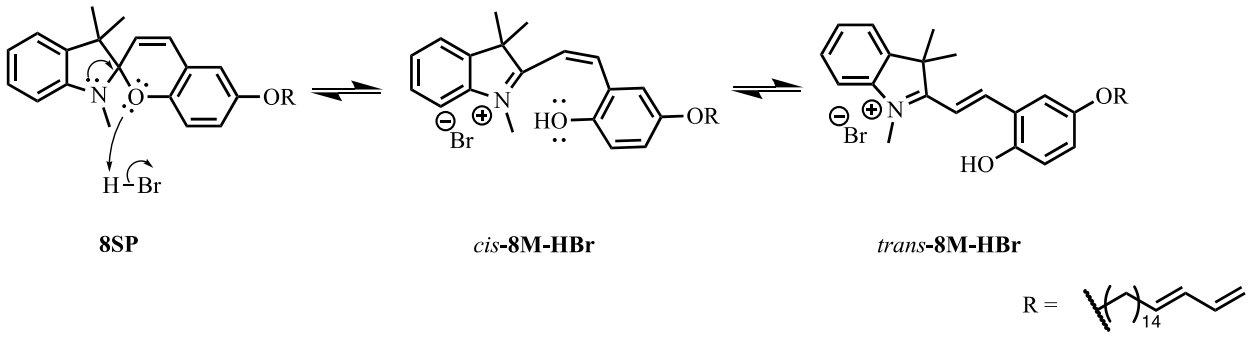

8SP *cis*-**8M-HBr** *trans*-**8M-HBr**

Scheme S1. General mechanism of the acid-promoted shift from **8SP** to **8M-HBr** with aq. HBr solution. Note that the double bond isomer formed in the *cis*-**8M-HBr** state can exist in a number of isomerization states but will eventually take on the most stable *trans*-**8M-HBr** form.[20,26,27]

5.5.2.7 Gyroid-phase Network Pore Diameter Calculations[14,28]

Due to the monomer leaching experiments showing no loss of material upon swelling, the spiropyran-based monomer dopant was assumed to be part of the cross-linked film and was counted as part of the occupied volume fraction of the unit cell. The gyroid pore diameter calculations that follow are derived from previously published procedures.[14,28] Hexagonal and lamellar phase boundaries of monomer blends of (**6** + **8**) are assumed to be identical to neat monomer **6**. An additional assumption of note is that the gyroid is of a consistent shape regardless of small deviations in mass from sample-to-sample. Mass percentages used in samples observed in the study (N = 12) were shown as (87.5 ± 0.5) wt% monomer blend.

To calculate the pore size of the double gyroid network, we first calculate the molecular volume of the material using the molecular weight of the organic portion of the cross-linkable surfactant, the density of the material, and Avogadro's number.

$$Acidified \rightarrow v = \frac{MW}{\rho N_{Avo}} = \frac{\big(0.01(542.83) + 0.99(419.72)\big)}{\rho N_{Avo}} = 0.777nm^3 \qquad \text{(Eq. 5.1)}$$

$$Neutral \rightarrow v = \frac{MW}{\rho N_{Avo}} = \frac{\left(0.01(541.83) + 0.99(419.72)\right)}{\rho N_{Avo}} = \ 0.777nm^3 \qquad \text{(Eq. 5.2)}$$

Note that this is a 0.3% change from the case of pure monomer **6**, which is 0.77 nm^3. From this point on, all lattice parameters are considered constants unless otherwise noted.

After the calculation of the volume fraction, the value of the cross-section area of the molecule is calculated from the lamellar phase lattice parameter and the volume fraction of that lamellar phase. (a = 3.31 nm, ϕ = 0.9045)

$$A_n = \frac{2v}{a_{lamellar}\emptyset_{mem}} = 0.5191 \text{ nm}^2 \qquad \text{(Eq. 5.3)}$$

The radius of the hexagonal cylinders was calculated by the lattice parameter (a = 4.87 nm, ϕ = 0.6785).

$$r = \sqrt{\frac{\sqrt{3}\emptyset_{mem}a_{hex}^2}{2\pi}} = 2.106 \text{ nm} \qquad \text{(Eq. 5.4)}$$

The estimation of the surfactant-water interface is predicted as the ratio of the molecular volume and the radius of the hexagonal cylinders.

$$A_{interface} = \frac{2v}{r} = 0.7379 \text{ nm}^2 \qquad \text{(Eq. 5.5)}$$

After this, we assume a constant molecular volume within the area neutral surface. This corresponds to the lipid bilayer, otherwise seen as the diene tails of the three blend materials. It is estimated as the ratio of the lamellar and hexagonal cross-sectional areas multiplied by the molecular volume.

$$v_n = v\left(\frac{A_n}{A_{interface}}\right)^2 = 0.3845\ \text{nm}^3 \qquad \text{(Eq. 5.6)}$$

We then minimize for the pore size of the *Ia3d* gyroid structure, which is consistent with the space group observed in the main manuscript gels. The constants of the *Ia3d* space group are (A_0 = 3.091, χ = -8). A minimization operation is then performed to find the radius of the pore channel, and we double this to obtain the pore diameter. The calculated diameter is then compared across the acidification conditions to yield the plots shown in Figure 5.4 in the main manuscript.

$$\frac{2A_0 a_{gyroid}^2}{A_n}\left(1 + \frac{2\pi\chi}{A_0 a_{gyroid}^2} z^2\right) = \left[\frac{a_{gyroid}^3 - 2A_0 a_{gyroid}^2 z\left(1 + \frac{2\pi\chi}{3A_0 a_{gyroid}^2} z^2\right)}{v_n}\right] \qquad \text{Eq. (5.7)}$$

The standard error of the slope was then calculated for each plot shown in Figure for in the main manuscript. For undoped gyroid films, the standard error of the slope was: 1.07 x 10^{-3}; for films with 0.8 wt% **2**, the standard error of the slope was: 1.15 x 10^{-3}; for films with 1.2 wt% **2**, the standard error of the slope was: 2.15 x 10^{-3}.

5.5.2.8 Procedure for Measuring Water Vapor Transport Rate through a Bulk Gyroid Film of Cross-linked (**6** + **8**) as a Function of Liquid Water Reservoir pH

Film samples were pinned to the cap of a 2.5-mL scintillation vial with the cap inset removed. The cap was screwed back on, with cutout of the inset serving to seal the film without damaging the film. If a good seal was not obtained by this pinning method, epoxy was used to further fill in the gaps of the vial. The vials were placed in a desiccator with Drierite® and sealed for a period of approximately 2 weeks at room temperature (RT) (22 °C), with mass measurements

occurring every 24 h. Colorimetric and mass-loss changes were on the order of 24–96 h to reach steady-state. Each day, the instantaneous mass loss was recorded through the vials, and the desiccator was sealed again. Each film thickness was measured using a digital micrometer, and the instantaneous mass transport rates were calculated and compared against the rate for an open vial of the same solvent. The setup is shown in Figure 5.18 below. Films were checked using PLM through 45° polarized light for excess birefringence indicative of a pinhole leak. Leaking samples, when corrected for area of vapor diffusion, showed vapor diffusion rates statistically similar to those of open cells.

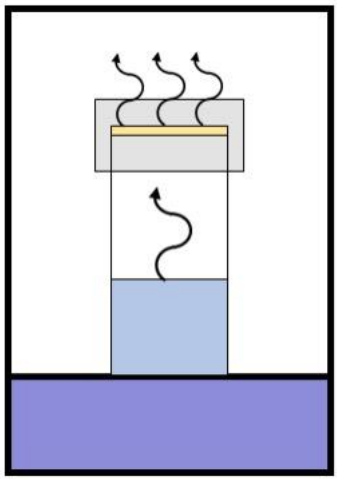

Figure 5.18 Schematic representation of the apparatus used for measuring the vapor transport rate of cross-linked gyroid bulk films of (**6** + **8**) as a function of feed water pH. The LLC polymer film is represented by the thin yellow line within the vial's cap. The solution (represented in light blue) was either pure DI H_2O (pH = ca. 6.4, 0 M HCl), 1 M aq. HCl, or 2 M aq. HCl. The entire vial was sealed within a desiccator (the desiccant is represented by blue shading).

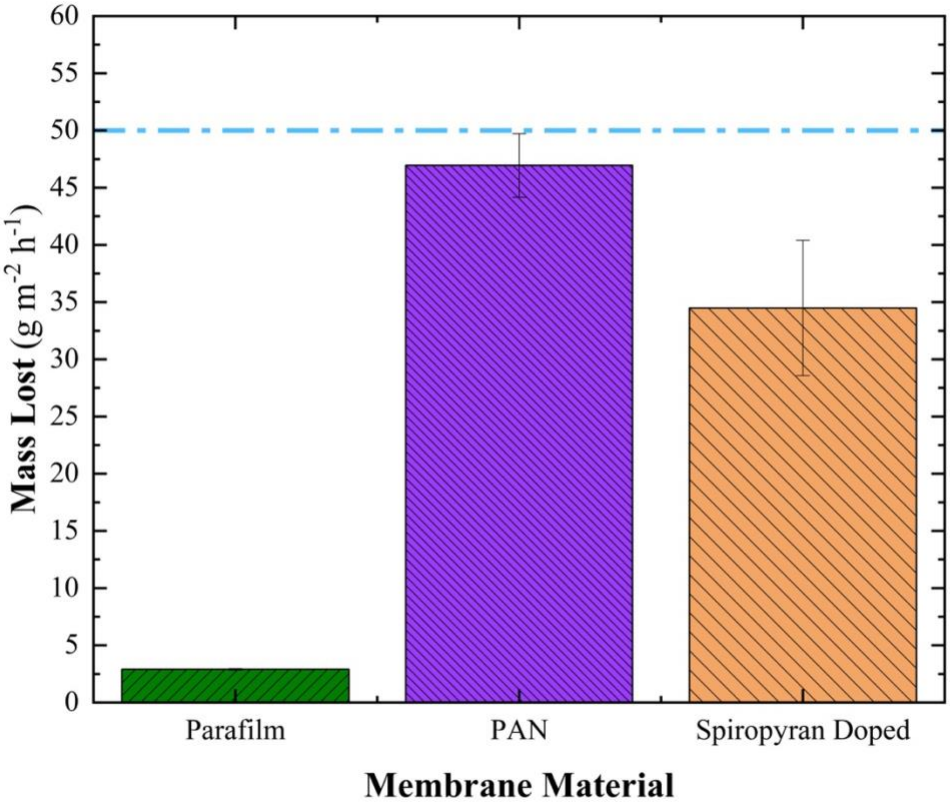

Figure 5.19 Room-temperature water mass-loss rates for film vapor cells in a desiccator filled with Drierite® comparing spiropyran-doped films against commercial membranes. The dashed blue line indicates the open-cell rate of ca. 50 g m^{-2} h^{-1} under these test conditions. Thicknesses of each film material were: bulk hydrophobic Parafilm™ = 22 μm; PAN supported on porous PET = 177 μm composite membrane total thickness, 94 μm for the PAN active top layer (Sterlitech); and bulk spiropyran-doped gyroid film = 99 μm. Error bars represent ± 1 standard deviation.

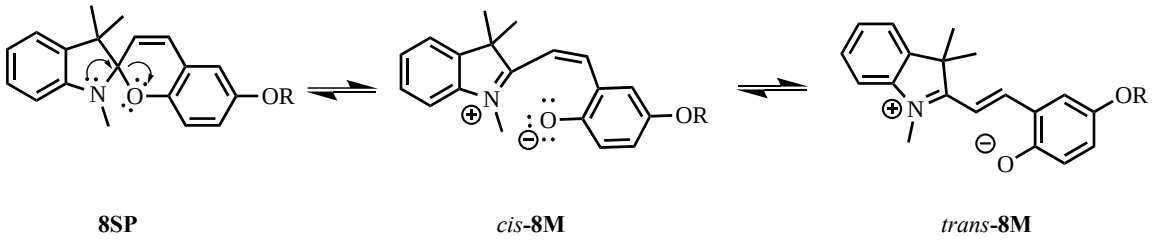

8SP *cis*-**8M** *trans*-**8M**

R = cross-linked alkyl tail region

Scheme 5.2 General mechanism of the reversible photo-isomerization of **8SP** to **8M**.[20,26] Note that in our studies, the diene tail region is already previously cross-linked during the bulk film fabrication process.

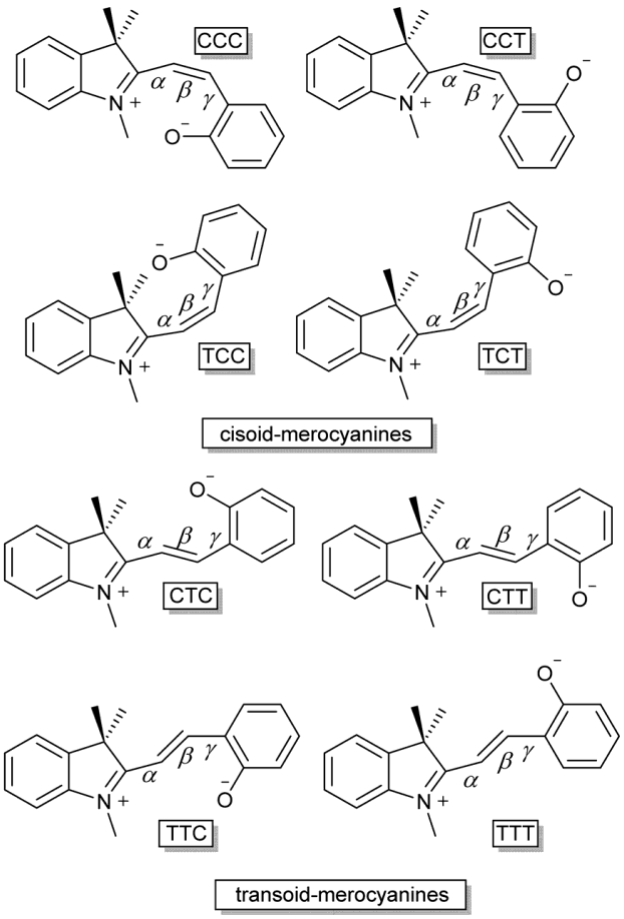

Figure 5.20 Eight possible isomers of the open zwitterionic (i.e., non-protonated) merocyanine (**M**) form. Figure reproduced from Ref. 24. Copyright Royal Society of Chemistry, 2019.

5.5.3 Acknowledgments

P. L., S. S. D., and D. L. G. thank the Joint Science and Technology Office for Chemical Biological Defense (JSTO CBD) for funding under CB10872. C.O.O. and C. J. acknowledge NSF support through DMR-1945966. The authors acknowledge use of the DEXS facility at the Univ. of Pennsylvania (NSF MRSEC 1720530), the purchase of which was made possible by NSF MRI 1725969, ARO DURIP W911NF-17-1-0282, and the Univ. of Pennsylvania. The authors also thank Alexander T. Gilligan in Prof. N. H. Damrauer's group at the Univ. of Colorado Boulder for performing UV-visible absorption characterization with their instrument.

5.6 References

1. For reviews of cross-linked LLC polymer materials for advanced applications, see: (a) Gin, D. L.; Gu, W.; Pindzola, B. A.; Zhou, W. J. Polymerized Lyotropic Liquid Crystal Assemblies for Materials Applications. *Acc. Chem. Res.* **2001**, *34*, 973–980. (b) Mueller, A.; O'Brien, D. F. Supramolecular Materials via Polymerization of Mesophases of Hydrated Amphiphiles. *Chem. Rev.* **2002**, *102*, 727–758. (c) Gin, D. L.; Lu, X.; Nemade, P. R.; Pecinovsky, C. S.; Xu, Y.; Zhou, M. Recent Advances in the Design of Polymerizable Lyotropic Liquid-Crystal Assemblies for Heterogeneous Catalysis and Selective Separations. *Adv. Funct. Mater.* **2006**, *16*, 865–878. (d) Saadat, Y.; Imran O. Q.; Osuji, C. O.; Foudazi, R. Lyotropic liquid crystals as templates for advanced materials. *J. Mater. Chem. A* **2021**, *9*, 21607–21658.
2. For general reviews of LLC phases, see: (a) Tate, M. W.; Eikenberry, E. F.; Turner, D. C.; Shyamsunder, E.; Gruner, S. M. Nonbilayer phases of membrane lipids. *Chem. Phys. Lipids* **1991**, *57*, 147–164. (b) Seddon, J. M. Structure of the inverted hexagonal (H_{II}) phase, and non-

lamellar phase transitions of lipids. *Biochim. Biophys. Acta*, **1990**, *1031*, 1–69. (c) Tiddy, G. J. T. Surfactant-water liquid crystal phases. *Phys. Rep.* **1980**, *57*, 1–46.

3. Israelachivili, J. N. Intermolecular and Surface Forces with Applications to Colloidal and Biological Systems. Academic: London; **1985**, 249.
4. For a review of cross-linked Q-phase LLC materials and their applications, see: Wiesenauer, B. R.; Gin, D. L. Nanoporous Polymer Materials Based on Self-Organized, Bicontinuous Cubic Lyotropic Liquid Crystal Assemblies and Their Applications. *Polym. J.* **2012**, *44*, 461–468.
5. Lu, X.; Nguyen, V.; Zhou, M.; Zeng, X.; Jin, J.; Elliott, B. J.; Gin, D. L. Cross-linked Bicontinuous Cubic Lyotropic Liquid Crystal-Butyl Rubber Composites: Highly Selective, Breathable Barrier Materials for Chemical Agent Protection. *Adv. Mater.* **2006**, *18*, 3294–3298.
6. Dwulet, G. E.; Dischinger, S. M.; McGrath, M. J.; Basalla, A. J.; Malecha, J. J.; Noble, R. D.; Gin, D. L. Breathable, Polydopamine-Coated Nanoporous Membranes That Selectively Reject Nerve and Blister Agent Simulant Vapors. *Ind. Eng. Chem. Res.* **2019**, *58*, 21890–21893.
7. Zhou, M.; Nemade, P. R.; Lu, X.; Zeng, X.; Hatakeyama, E. S.; Noble, R. D.; Gin, D. L. New Type of Membrane Material for Water Desalination Based on a Cross-linked Bicontinuous Cubic Lyotropic Liquid Crystal Assembly. *J. Am. Chem. Soc.* **2007**, *129*, 9574–9575.
8. Carter, B. M.; Wiesenauer, B. R.; Hatakeyama, E. S.; Barton, J. L.; Noble, R. D.; Gin, D.L. Glycerol-based Bicontinuous Cubic Lyotropic Liquid Crystal Monomer System for the Fabrication of Thin-film Membranes with Uniform Nanopores. *Chem. Mater*. **2012**, *24*, 4005–4007.

9. Kerr, R. L.; Miller, S. A.; Shoemaker, R. K.; Elliott, B. J.; Gin, D. L. New Type of Li Ion Conductor with 3D Interconnected Nanochannels via Polymerization of a Liquid Organic Electrolyte-Filled Lyotropic Liquid-Crystal Assembly. *J. Am. Chem. Soc*. **2009**, *131*, 15972–15973.
10. Pindzola, B. A.; Jin, J.; Gin, D. L. Cross-Linked Normal Hexagonal and Bicontinuous Cubic Assemblies via Polymerizable Gemini Amphiphiles. *J. Am. Chem. Soc.* **2003**, *125*, 2940–2949.
11. Hatakeyama, E. S.; Wiesenauer, B. R.; Gabriel, C. J.; Noble, R. D.; Gin, D. L. Nanoporous, bicontinuous Cubic Lyotropic Liquid Crystal Networks via Polymerizable Gemini Ammonium Surfactants. *Chem. Mater*. **2010**, *22*, 4525–4527.
12. Kobayashi, T.; Li, Y.-X.; Ono, A.; Zeng, X.-B.; Ichikawa, T. Gyroid structured aqua-sheets with sub-nanometer thickness enabling 3D fast proton relay conduction. *Chem. Sci.* **2019**, *10*, 6245–6253.
13. Lee, Y. S.; Yang, J. Z.; Sisson, T. M.; Frankel, D. A.; Gleeson, J. T.; Aksay, E.; Keller, S. L.; Gruner, S. M.; O'Brien, D. F. Polymerization of nonlamellar lipid assemblies. *J. Am. Chem. Soc.* **1995**, *117*, 5573–5578.
14. Imran, O. Q.; Li, P.; Kim, N. K.; Gin, D. L.; Osuji, C. O. Stable cross-linked lyotropic gyroid mesophases from single-head/single-tail cross-linkable monomers. *Chem. Commun.* **2021**, *57*, 10931–10934.
15. Dwulet, G. E.; Gin, D. L. Ordered nanoporous lyotropic liquid crystal polymer resin for heterogenous catalytic aerobic oxidation of alcohols. *Chem. Commun.* **2018**, 54, 12053–12056.
16. Pecinovsky, C. S.; Hatakeyama, E. S.; Gin, D. L. Polymerizable Photochromic Macrocyclic Metallomesogens: Design of Supramolecular Polymers with Responsive Nanopores. *Adv. Mater*. **2008**, *20*, 174–178.

17. Minkin, V. I. Photo-, Thermo-, Solvato-, and Electrochromic Spiroheterocyclic Compounds. *Chem. Rev.* **2004**, *104*, 2751–2776.
18. Russew, M.-M.; Hect, S. Photoswitches: From Molecules to Materials. *Adv. Mater.* **2010**, *22*, 3348–3360.
19. Grinthal, A.; Aizenberg, J. Adaptive all the way down: Building responsive materials from hierarchies of chemomechanical feedback. *Chem. Soc. Rev.* **2013**, *42*, 7072–7085.
20. Klajn, R. Spiropyran-based dynamic materials. *Chem. Soc. Rev.* **2014**, *43*, 148–184.
21. Tan, B.-H.; Yoshio, M.; Ichikawa, T.; Mukai, T.; Ohno, H.; Kato, T. Spiropyran-based liquid crystals: the formation of columnar phases *via* acid-induced spiro-merocyanine isomerisation. *Chem. Commun*. **2006**, 4703–4705.
22. Tan, B.-H.; Yoshio, M.; Kato, T. Induction of Columnar and Smectic Phases for Spiropyran Derivatives: Effects of Acidochromism and Photochromism. *Chem. Asian J.* **2008**, *3*, 534–541.
23. Tan, B.-H.; Yoshio, M.; Watanabe, K.; Hamasaki, A.; Ohno, H.; Kato, T. Columnar liquid-crystalline assemblies composed of spiropyran derivatives and sulfonic acids. *Polym. Adv. Technol.* **2008**, *19*, 1362–1368.
24. Kortekaas, L.; Browne, W. R. The evolution of spiropyran: fundamentals and progress of an extraordinarily versatile photochrome. *Chem. Soc. Rev.* **2019**, *48*, 3406–3424.
25. Bhattacharyya, D.; Schäfer, T.; Wickramasinghe, S. R.; Daunert, S. Responsive Membranes and Materials. Chichester, West Sussex, UK, **2013**.
26. Keum, S-R.; Lee, K-B.; Kazmaier, P. M.; Buncel, E. A novel method for measurement of the merocyanine-spiropyran interconversion in non-activated 1,3,3-trimethylspiro-(2H-1-benzopyran-2,2'-indoline) derivatives. *Tetrahedron Lett.* **1994**, *35*, 1015–1018.

27. Wojtyk, J. T. C.; Wasey, A.; Xian, N-N.; Kazmaier, P. M.; Hoz, S.; Yu, C.; Lemieux, R. P.; Buncel, E. Elucidating the Mechanisms of Acidochromic Spiropyran-Merocyanine Interconversion. *J. Phys. Chem. A.* **2007**, *111*, 2511–2516.

28. Asghar, K. A.; Rowlands, D. A.; Elliott, J. M.; Squires, A. M. Predicting Sizes of Hexagonal and Gyroid Metal Nanostructures from Liquid Crystal Templating. *ACS Nano* **2015**, *9*, 10970–10978.

29. Guo, J.; Wei, X.; Fang, X.; Shan, R.; Zhang, X. A rapid acid-vapor detector based on spiropyran-polymer composite. *Sens. Actuators B: Chem.* **2021**, *347*, 130623.

30. Garstecki, P.; Holyst, R. Periodic surfaces of simple and complex topology: Comparison of scattering patterns. *Phys. Rev. E.* **2001**, *64*, 021501.

31. Wohlgemuth, M.; Yufa, N.; Hoffman, J.; Thomas, E. L. Triply Periodic Bicontinuous Cubic Microdomain Morphologies by Symmetries. *Macromolecules* **2001**, *34*, 6083.

32. Winkler, J. D.; Deshayes, K.; Shao, B. Photodynamic Transport of Metal Ions. *J. Am. Chem. Soc.* **1989**, *111*, 769–770.

33. Görner, H.; Chibisov, A. K. Complexes of spiropyran-derived merocyanines with metal ions: Thermally activated and light-induced processes. *J. Chem. Soc., Faraday Trans.* **1998**, *94*, 2557–2564.

34. Suzuki, T.; Kato, T.; Shinozaki, H. Photo-reversible Pb^{2+}-complexation of thermoselective poly(*N*-isopropyl acrylamide-*co*-spiropyran acrylate) in water. *Chem. Commun.* **2004**, 2036–2037.

35. Radu, A.; Byrne, R.; Alhashimy, N.; Fusaro, M.; Scarmagnani, S.; Diamond, D. Spiropyran-based reversible, light-modulated sensing with reduced photofatigue. *J. Photochem. Photobiol. A.* **2009**, *206*, 109.

36. Ipe, B. I.; Mahima, S.; Thomas, K. G. Light-Induced Modulation of Self-Assembly on Spiropyran-Capped Gold Nanoparticles: A Potential System for the Controlled Release of Amino Acid Derivatives. *J. Am. Chem. Soc.* **2003**, *125*, 7174– 7175.
37. Berkovic, G.; Krongauz, V.; Weiss, V. Spiropyrans and Spirooxazines for Memories and Switches. *Chem. Rev.* **200**, *100*, 1741–1753.
38. Feng, X.; Imran. Q.; Zhang, Y.; Sixdenier, L.; Lu, X.; Kaufman, G.; Gabinet, U.; Kawabata, K.; Elimelech, M.; Osuji, C. O. Precise nanofiltration in a fouling-resistant self-assembled membrane with water-continuous transport pathways. *Sci. Adv.* **2019**, *5*, eaav9308.
39. Imran, O. Q.; Kim, N. K.; Bodkin, L. N.; Dwulet, G. E.; Feng, X.; Kawabata, K.; Elimelech, M.; Gin, D. L.; Osuji, C. O. Nanoscale Thickness Control of Nanoporous Films Derived from Directionally Photopolymerized Mesophases. *Adv. Mater. Interfaces* **2020**, *8*, 2001977.
40. Zhang, Y.; Dong, R.; Gabinet, U. R.; Poling-Skutvik, R.; Kim, N. K.; Lee, C.; Imran, O. Q.; Feng, X.; Osuji, C. O. Rapid Fabrication by Lyotropic Self-Assembly of Thin Nanofiltration Membranes with Uniform 1 Nanometer Pores. *ACS Nano* **2021**, *15*, 8192–8203.
41. Wu, C.-H.; Meng, W.; Yoshio, M. Low-Voltage-Driven Actuators Using Photo-Cross-Linked Ionic Columnar Liquid-Crystalline Polymer Films. *ACS Mater. Lett.* **2022**, *4*, 153–158.

Chapter 6: Summary and Future Work

6.1 Summary of Dissertation Work

This thesis focused on the study, design, and application of intrinsically cross-linkable bicontinuous cubic (Q) lyotropic liquid crystal (LLC) monomers. First, seven homologs of monomer **4a** were synthesized and examined for their ability to form a stable Q phase. Although several of these homologs could also form the Q phase, compared to the parent monomer the phase diagrams of each of these homologs did not suggest a significant improvement in the Q-phase window. Coupled with the disadvantage that monomer **4a** (as well as other previously reported intrinsically cross-linkable Q-phase LLC monomer systems) possessed moderate-to-difficult syntheses, high synthetic cost, and limited processability, it was clear to us that a novel Q-phase-forming LLC platform needed to be designed.

I was then able to help design and develop a single-head/single-tail Q-phase-forming monomer motif (monomer **6**) in collaboration with researchers at the University of Pennsylvania. Besides its novel Q-phase LLC motif, monomer **6** was less expensive and simpler to synthesize compared to the previous intrinsically cross-linkable Q-phase-forming amphiphiles. We were able to demonstrate that cross-linked Q-phase networks of **6** were exceptionally stable at elevated temperatures, upon exposure to organic solvents of interest, and upon exposure to aqueous acid and base solutions. The remarkable stability of cross-linked Q-phase films of **6** encouraged us to explore its tolerance to added functional groups or co-monomers while hopefully preserving its ability to form a cross-linked Q-phase network.

These results led to the final part of this thesis, which described the design and development of a novel stimuli-responsive Q-phase polymer network material. This new system consisted of a

small amount of a novel spiropyran-containing dopant monomer (**8**) that upon blending with monomer **6**, yielded a gyroid polymer network material that responded to multiple external stimuli with retention of the gyroid nanostructure. In collaboration with researchers at the University of Pennsylvania, initial studies of this new cross-linked Q-phase monomer blend system indicated reversible color changes when the polymer network was exposed to acidic aqueous solution or vapor. SAXS analysis revealed that the color changes were coupled with reversible changes of the Q-phase unit cell dimensions in the polymer network. These results led us to examine the effect of pH on vapor transport through our polymer networks. We found that as the concentration of acid in the external solution increased, vapor transport through the spiropyran-doped polymer films decreased. Furthermore, a color change was observed in the polymer films indicating that they could also act as colorimetric vapor indicators. Finally, Pb^{2+} ion uptake studies demonstrated that this novel spiropyran-containing system could irreversibly bind Pb^{2+} ions and permanently preserve the colorimetric response thereby allowing the material to act as a colorimetric sorbent for aq. Pb^{2+} ions.

6.2 Recommendations for Future Research Directions

The Q-phase monomer platforms designed and studied in Chapters 3, 4, and 5 of this thesis were all studied in their bulk polymer film state. Thin-film composite (TFC) membranes of these systems have yet to be achieved. The homologs discussed in Chapter 3 may be able to be cast into thin-film membranes due to their similar processable properties to their parent monomer **4a**, which has been extensively studied for membrane applications. Although the Q-phase window of the bis(imidazolium bromide) monomer platform was not significantly broadened through these homologs, transport properties of thin-film membranes of each homolog are still worth exploring

because each homolog may exhibit different pore sizes which may result in modified or improved transport.

The recent discovery of structurally simpler monomer **6** and its ability to form a Q phase means that many studies of **6** have yet to be done. First, a full phase diagram analysis of **6** with water has yet to be performed. Although a stable cross-linked Q phase was achieved for **6**, other LLC phases like the normal hexagonal (H_I) phase (which is also interesting for making LLC-polymer-based nanofiltration membranes) may also be exhibited for this system. Fabrication of TFC Q membranes of **6** is thus an immediate area of interest. If the high-stability of cross-liked Q-phase films of **6** could be translated to TFC membranes, these membranes would likely exhibit improved lifetimes and would reduce overall fabrication costs.

Fabrication of the stimuli-responsive system of (**6** + **8**) into supported thin films and expanding the material's responsive capabilities is also another immediate area of interest. Because of the difficult nature of preserving the Q phase during the fabrication of TFC membranes, exploring other LLC mesophases of membrane interest (e.g., the H_I phase) may yield new molecular-size-selective membrane materials with the intrinsic ability to visually detect and restrict the flow of acidic water vapor or other hazardous vapors of interest.[1-3] This system also demonstrated potential as an stimulus-gated sorbent for metal ions. Further work on this spiropyran-based co-monomer system should also include chemical modification and tuning of the system to allow for the possible development of a colorimetric, nanoporous, reversible ion-uptake material.

The tolerant nature of **6** to additives and its ability to maintain a Q phase despite added co-monomers suggests that besides stimuli responsive membranes, other functionalized Q-phase systems could be designed. Mechanophores, fluorophores, or even catalytically active groups may

be able to be blended-in via co-monomers with preservation of the Q phase. Despite these exciting possibilities for Q-phase functionality, TFC Q polymer membranes based on monomer **6** and its functional co-monomers must be demonstrated to pursue practical membrane applications.

6.3 References

1. Feng, X.; Imran, Q.; Zhang, Y.; Sixdenier, L.; Lu, X.; Kaufman, G.; Gabinet, U.; Kawabata, K.; Elimelech, M.; Osuji, C. O. Precise nanofiltration in a fouling-resistant self-assembled membrane with water-continuous transport pathways. *Sci. Adv.* **2019**, *5*, eaav9308.
2. Imran, O. Q.; Kim, N. K.; Bodkin, L. N.; Dwulet, G. E.; Feng, X.; Kawabata, K.; Elimelech, M.; Gin, D. L.; Osuji, C. O. Nanoscale Thickness Control of Nanoporous Films Derived from Directionally Photopolymerized Mesophases. *Adv. Mater. Interfaces* **2020**, *8*, 2001977.
3. Zhang, Y.; Dong, R.; Gabinet, U. R.; Poling-Skutvik, R.; Kim, N. K.; Lee, C.; Imran, O. Q.; Feng, X.; Osuji, C. O. Rapid Fabrication by Lyotropic Self-Assembly of Thin Film Nanofiltration Membranes with Uniform 1 Nanometer Pores. *ACS Nano* **2021**, *15*, 8192–8203.

Bibliography

1. For general reviews on LLC phases, see: (a) Tate, M. W.; Eikenberry, E. F.; Turner, D. C.; Shyamsunder, E.; Gruner, S. M. Nonbilayer phases of membrane lipids. *Chem. Phys. Lipids* **1991**, *57*, 147–164. (b) Seddon, J. M. Structure of the inverted hexagonal (H_{II}) phase, and non-lamellar phase transitions of lipids. *Biochim. Biophys. Acta* **1990**, *1031*, 1–69. (c) Tiddy, G. J. T. Surfactant-water liquid crystal phases. *Phys. Rep.* **1980**, *57*, 1–46.
2. For a thorough review of LLC materials as templates for advanced applications, see: Saadat, Y.; Imran, O. Q.; Osuji, C. O.; Foudazi, R. Lyotropic liquid crystals as templates for advanced materials. *J. Mater. Chem. A* **2021**, *9*, 21607–21658.
3. Israelachivili, J. N. Intermolecular and Surface Forces with Applications to Colloidal and Biological Systems. Academic: London; **1985**, 249.
4. Wiesenauer, B. R.; Gin, D. L. Nanoporous Polymer Materials Based on Self-Organized, Bicontinuous Cubic Lyotropic Liquid Crystal Assemblies and Their Applications. *Polym. J.* **2012**, *44*, 461–468.
5. Kerr, R. L.; Miller, S. A.; Shoemaker, R. K.; Elliott, B. J.; Gin, D. L. New Type of Li Ion Conductor with 3D Interconnected Nanochannels via Polymerization of a Liquid Organic Electrolyte-Filled Lyotropic Liquid-Crystal Assembly. *J. Am. Chem. Soc*. **2009**, *131*, 15972–15973.
6. Carter, B. M.; Wiesenauer, B. R.; Hatakeyama, E. S.; Barton, J. L.; Noble, R. D.; Gin, D.L. Glycerol-based Bicontinuous Cubic Lyotropic Liquid Crystal Monomer System for the Fabrication of Thin-film Membranes with Uniform Nanopores. *Chem. Mater*. **2012**, *24*, 4005–4007.

7. Gin, D. L.; Pecinovsky, C. S.; Bara, J. E.; Kerr, R. L. Functional Lyotropic Liquid Crystal Materials. *Struct. Bonding* **2007**, *128*, 181–222.
8. Gin, D. L.; Gu, W.; Pindzola, B. A.; Zhou, W. J. Polymerized Lyotropic Liquid Crystal Assemblies for Materials Applications. *Acc. Chem. Res*. **2001**, *34*, 973–980.
9. Gin, D. L.; Lu, X.; Nemade, P. R.; Pecinovsky, C. S.; Xu, Y.; Zhou, M. Recent Advances in the Design of Polymerizable Lyotropic Liquid-Crystal Assemblies for Heterogeneous Catalysis and Selective Separations. *Adv. Funct. Mater*. **2006**, *16*, 865–878.
10. Mueller, A.; O'Brien, D. F. Supramolecular Materials via Polymerization of Mesophases of Hydrated Amphiphiles. *Chem. Rev*. **2002**, *102*, 727–758.
11. Kato, T.; Yoshio, M.; Ichikawa, T.; Soberats, B.; Ohno, H.; Funahashi, M. Transport of ions and electrons in nanostructured liquid crystals. *Nat. Rev. Mater.* **2017**, *2*, 1–20.
12. Lu, X.; Nguyen, V.; Zhou, M.; Zeng, X.; Jin, J.; Elliott, B. J.; Gin, D. L. Cross-linked Bicontinuous Cubic Lyotropic Liquid Crystal-Butyl Rubber Composites: Highly Selective, Breathable Barrier Materials for Chemical Agent Protection. *Adv. Mater*. **2006**, *18*, 3294–3298.
13. Maekawa, A.; Kobayashi, T.; Ichikawa, T. Gyroid nanostructured soft membranes formed by controlling the degree of crosslinking polymerization of bicontinuous cubic liquid-crystalline monomers. *Polym. J.* **2021**, *53*, 463–470.
14. Kobayashi, T.; Li, Y.-X.; Hirota, Y.; Maekawa, A.; Nishiyama, N.; Zeng, X.-B.; Ichikawa, T. Gyroid-Nanostructured All-Solid Polymer Films Combining High H^+ Conductivity with Low H_2 Permeability. *Macromol. Rapid. Commun.* **2021**, 2100115.

15. Jennings, J.; Green, B.; Mann, T. J.; Guymon, C. A.; Mahanthappa, M. K. Nanoporous Polymer Networks Templated by Gemini Surfactant Lyotropic Liquid Crystals. *Chem. Mater.* **2018**, *30*, 185–196.
16. Takeuchi, H.; Ichikawa, Y.; Yoshio, M.; Kato, T.; Ohno, H. Induction of bicontinuous cubic liquid-crystalline assemblies for polymerizable amphiphiles via tailor-made design of ionic liquids. *Chem. Commun.* **2016**, *52*, 13861–13864.
17. Fontell, K. Cubic phases in surfactant and surfactant-like lipid systems. *Colloid Polym. Sci.* **1990**, *268*, 264–285.
18. Pindzola, B. A.; Jin, J.; Gin, D. L. Cross-Linked Normal Hexagonal and Bicontinuous Cubic Assemblies via Polymerizable Gemini Amphiphiles. *J. Am. Chem. Soc.* **2003**, *125*, 2940–2949.
19. Zhou, M.; Nemade, P. R.; Lu, X.; Zeng, X.; Hatakeyama, E. S.; Noble, R. D.; Gin, D. L. New Type of Membrane Material for Water Desalination Based on a Cross-linked Bicontinuous Cubic Lyotropic Liquid Crystal Assembly. *J. Am. Chem. Soc.* **2007**, *129*, 9574–9575.
20. Hatakeyama, E. S.; Wiesenauer, B. R.; Gabriel, C. J.; Noble, R. D.; Gin, D. L. Nanoporous, bicontinuous Cubic Lyotropic Liquid Crystal Networks via Polymerizable Gemini Ammonium Surfactants. *Chem. Mater.* **2010**, *22*, 4525–4527.
21. Kobayashi, T.; Li, Y.-X.; Ono, A.; Zeng, X.-B.; Ichikawa, T. Gyroid structured aqua-sheets with sub-nanometer thickness enabling 3D fast proton relay conduction. *Chem. Sci.* **2019**, *10*, 6245–6253.
22. Lee, Y. S.; Yang, J. Z.; Sisson, T. M.; Frankel, D. A.; Gleeson, J. T.; Aksay, E.; Keller, S. L.; Gruner, S. M.; O'Brien, D. F. Polymerization of nonlamellar lipid assemblies. *J. Am. Chem. Soc.* **1995**, *117*, 5573–5578.

23. Srisiri, W.; Benedicto, A.; O'Brien, D. F. Stabilization of a bicontinuous cubic phase from polymerizable monoacylglycerol and diacylglycerol. *Langmuir* **1998**, *14*, 1921–1926.
24. McGrath, K. M.; Drummond, C. J. Polymerisation of liquid crystalline phases in binary surfactant/water systems. Part 1. Allyldodecyldimethylammonium bromide and allyldidodecylmethylammonium bromide. *Colloid Polym. Sci.* **1996**, 274, 316–333.
25. Yang, D.; O'Brien, D. F.; Marder, S. R. Polymerized bicontinuous cubic nanoparticles (cubosome) from a reactive monoacylglycerol. *J. Am. Chem. Soc.* **2002**, *124*, 13388–13389.
26. Gao, X.; Lu, F.; Liu, Y.; Sun, N.; Zheng, L. The facile construction of an anion exchange membrane with 3D interconnected ionic nano-channels. *Chem. Commun.* **2017**, *53*, 767–770.
27. Feng, X.; Imran. Q.; Zhang, Y.; Sixdenier, L.; Lu, X.; Kaufman, G.; Gabinet, U.; Kawabata, K.; Elimelech, M.; Osuji, C. O. Precise nanofiltration in a fouling-resistant self-assembled membrane with water-continuous transport pathways. *Sci. Adv.* **2019**, *5*, eaav9308.
28. Wu, H.; Xu, F.; Gao, G.; Feng, X. Highly Ordered Interconnected 1 nm Pores in Polymers Fabricated from Easily Accessible Gyroid Liquid Crystals. *Macromolecules* **2021**, *54*, 5856–5865.
29. Imran, O. Q.; Li, P.; Kim, N. K.; Gin, D. L.; Osuji, C. O. Stable cross-linked lyotropic gyroid mesophases from single-head/single-tail cross-linkable monomers. *Chem. Commun.* **2021**, *57*, 10931–10934.
30. Dischinger, S. M.; McGrath, M. J.; Bourland, K. R.; Noble, R. D.; Gin, D. L. Effect of Post-Polymerization Anion-Exchange on the Rejection of Uncharged Aqueous Solutes in Nanoporous, Ionic, Lyotropic Liquid Crystal Polymer Membranes. *J. Membr. Sci.* **2017**, *529*, 72–79.

31. Dwulet, G. E.; Dischinger, S. M.; McGrath, M. J.; Basalla, A. J.; Malecha, J. J.; Noble, R. D.; Gin, D. L. Breathable, Polydopamine-Coated Nanoporous Membranes That Selectively Reject Nerve and Blister Agent Simulant Vapors. *Ind. Eng. Chem. Res.* **2019**, *58*, 21890–21893.
32. Dwulet, G. E.; Gin, D. L. Ordered nanoporous lyotropic liquid crystal polymer resin for heterogenous catalytic aerobic oxidation of alcohols. *Chem. Commun.* **2018**, 54, 12053–12056.
33. Perroni, D. V.; Baez-Cotto, C. M.; Sorenson, G. P.; Mahanthappa, M. K. Linker Length-Dependent Control of Gemini Surfactant Aqueous Lyotropic Gyroid Phase Stability. *J. Phys. Chem. Lett.* **2015**, *6*, 993–998.
34. Mantha, S.; McDaniel, J. G.; Perroni, D. V.; Mahanthappa, M. K.; Yethiraj, A. Electrostatic Interactions Govern "Odd/Even" Effects in Water-Induced Gemini Surfactant Self-Assembly. *J. Phys. Chem. B* **2017**, *121*, 565–576.
35. Hoag, B. P.; Gin, D. L. Cross-Linkable Liquid Crystal Monomers Containing Hydrocarbon 1,3-Diene Tail Systems. *Macromolecules* **2000**, *33*, 8549–8558.
36. Pindzola, B. A.; Hoag, B. P.; Gin, D. L. Polymerization of a Phosphonium Diene Amphiphile in the Regular Hexagonal Phase with Retention of Mesostructure. *J. Am. Chem. Soc.* **2001**, *123*, 4617–4618.
37. Sharma, S.; Tandon, M.; Lown, J. W. Design and Synthesis of Novel Thiazole-Containing Cross-Linked Polyamides Related to the Antiviral Antibiotic Distamycin. *J. Org. Chem.* **2000**, *65*, 1102–1107.
38. Bara, J. E.; Hatakeyama, E. S.; Wiesenauer, B. R.; Zeng, X.; Noble, R. D.; Gin, D. L. Thermotropic Liquid Crystal Behavior of Gemini Imidazolium-based Ionic Amphiphiles. *Liq. Cryst.* **2010**, *37*, 1587–1599.

39. Merino, I.; Thompson, J. D.; Millard, C. B.; Schmidt, J. J.; Pang, Y.-P. Bis-imidazole as molecular probes for peripheral sites of the zinc endopeptidase of botulinum neurotoxin serotype A. *Bioorg. Med. Chem.* **2006**, *14*, 3583–3591.
40. Seddon, J. M.; Robins, J.; Gulik-Krzywicki, T.; Delacroix, H. Inverse micellar phases of phospholipids and glycolipids. *Phys. Chem. Chem. Phys.* **2000**, *2*, 4485–4493.
41. Huang, Y.; Gui, S. Factors affecting the structure of lyotropic liquid crystals and the correlation between structure and drug diffusion. *RSC Adv.* **2018**, *8*, 6978 – 6987.
42. Blanton, T. N.; Huang, T. C.; Toraya, H.; Hubbard, C. R.; Robie, S. B.; Louër, D.; Göbel, H. E.; Will, G.; Gilles, R.; Raftery, T. JCPDS–International Centre for Diffraction Data round robin study of silver behenate. A possible low-angle X-ray diffraction calibration standard. *Powd. Diffract.* **1995**, *10*, 91–95.
43. Piancatelli, G. *Encyclopedia of Reagents for Organic Synthesis*, **2001**, 1, John Wiley & Son Ltd., United Kingdom.
44. Zhang, H.; Li, L.; Möller, M.; Zhu, X.; Rueda, J. J. H.; Rosenthal, M.; Ivanov, D. A. From channel-forming ionic liquid crystals exhibiting humidity-induced phase transitions to nanostructured ion-conducting polymer membranes. *Adv. Mater*. **2013**, *25*, 3543–3548.
45. Sisson, T. M.; Srisiri, W.; O'Brien, D. F. Novel Polymer Architectures via the Selective Polymerization of Lyotropic Liquid Crystals of Heterobifunctional Amphiphiles. *J. Am. Chem. Soc.* **1998**, *120*, 2322–2329.
46. Liu, S.; O'Brien, D. F. Cross-Linking Polymerization in Two-Dimensional Assemblies: Effect of the Reactive Group Site. *Macromolecules* **1999**, *32*, 5519– 5524.
47. Liu, S.; Sisson, T. M.; O'Brien, D. F. Synthesis and Polymerization of Heterobifunctional Amphiphiles to Cross-Link Supramolecular Assemblies. *Macromolecules* **2001**, *34*, 465–473.

48. Zhang, Y.; Dong, R.; Gabinet, U. R.; Poling-Skutvik, R.; Kim, N. K.; Lee, C.; Imran, O. Q.; Feng, X.; Osuji, C. O. Rapid Fabrication by Lyotropic Self-Assembly of Thin Nanofiltration Membranes with Uniform 1 Nanometer Pores. *ACS Nano* **2021**, *15*, 8192–8203.

49. Asghar, K. A.; Rowlands, D. A.; Elliott, J. M.; Squires, A. M. Predicting Sizes of Hexagonal and Gyroid Metal Nanostructures from Liquid Crystal Templating. *ACS Nano* **2015**, *9*, 10970–10978.

50. Dischinger, S. M.; Rosenblum, J.; Noble, R. D.; Gin, D. L.; Linden, K. G. Application of a lyotropic liquid crystal nanofiltration membrane for hydraulic fracturing flowback water: Selectivity and implications for treatment. *J. Membr. Sci.* **2017**, *543*, 319–327.

51. Detsi, E.; De Jong, E.; Zinchenko, A.; Vukovic, Z.; Vukovic, I.; Punzhin, S.; Loos, K.; ten Brinke, G.; De Raedt, H. A.; Onck, P. R.; De Hosson, J. T. M. On the specific surface area of nanoporous materials. *Acta Mater.* **2011**, *59*, 7488–7497.

52. Ravikovitch, P. I.; Neimark, A. V. Relations between Structural Parameters and Adsorption Characterization of Templated Nanoporous Materials with Cubic Symmetry. *Langmuir* **2000**, *16*, 2419–2423.

53. Pecinovsky, C. S.; Hatakeyama, E. S.; Gin, D. L. Polymerizable Photochromic Macrocyclic Metallomesogens: Design of Supramolecular Polymers with Responsive Nanopores. *Adv. Mater.* **2008**, *20*, 174–178.

54. Minkin, V. I. Photo-, Thermo-, Solvato-, and Electrochromic Spiroheterocyclic Compounds. *Chem. Rev.* **2004**, *104*, 2751–2776.

55. Russew, M.-M.; Hect, S. Photoswitches: From Molecules to Materials. *Adv. Mater.* **2010**, *22*, 3348–3360.

56. Grinthal, A.; Aizenberg, J. Adaptive all the way down: Building responsive materials from hierarchies of chemomechanical feedback. *Chem. Soc. Rev.* **2013**, *42*, 7072–7085.
57. Klajn, R. Spiropyran-based dynamic materials. *Chem. Soc. Rev.* **2014**, *43*, 148–184.
58. Tan, B.-H.; Yoshio, M.; Ichikawa, T.; Mukai, T.; Ohno, H.; Kato, T. Spiropyran-based liquid crystals: the formation of columnar phases *via* acid-induced spiro-merocyanine isomerisation. *Chem. Commun*. **2006**, 4703–4705.
59. Tan, B.-H.; Yoshio, M.; Kato, T. Induction of Columnar and Smectic Phases for Spiropyran Derivatives: Effects of Acidochromism and Photochromism. *Chem. Asian J.* **2008**, *3*, 534–541.
60. Tan, B.-H.; Yoshio, M.; Watanabe, K.; Hamasaki, A.; Ohno, H.; Kato, T. Columnar liquid-crystalline assemblies composed of spiropyran derivatives and sulfonic acids. *Polym. Adv. Technol.* **2008**, *19*, 1362–1368.
61. Kortekaas, L.; Browne, W. R. The evolution of spiropyran: fundamentals and progress of an extraordinarily versatile photochrome. *Chem. Soc. Rev.* **2019**, *48*, 3406–3424.
62. Bhattacharyya, D.; Schäfer, T.; Wickramasinghe, S. R.; Daunert, S. Responsive Membranes and Materials. Chichester, West Sussex, UK, **2013**.
63. Keum, S.-R.; Lee, K.-B.; Kazmaier, P. M.; Buncel, E. A novel method for measurement of the merocyanine-spiropyran interconversion in non-activated 1,3,3-trimethylspiro-(2H-1-benzopyran-2,2'-indoline) derivatives. *Tetrahedron Lett.* **1994**, *35*, 1015–1018.
64. Wojtyk, J. T. C.; Wasey, A.; Xian, N.-N.; Kazmaier, P. M.; Hoz, S.; Yu, C.; Lemieux, R. P.; Buncel, E. Elucidating the Mechanisms of Acidochromic Spiropyran-Merocyanine Interconversion. *J. Phys. Chem. A* **2007**, *111*, 2511–2516.
65. Guo, J.; Wei, X.; Fang, X.; Shan, R.; Zhang, X. A rapid acid-vapor detector based on spiropyran-polymer composite. *Sens. Actuators B: Chem.* **2021**, *347*, 130623.

66. Garstecki, P.; Holyst, R. Periodic surfaces of simple and complex topology: Comparison of scattering patterns. *Phys. Rev. E* **2001**, *64*, 021501.

67. Wohlgemuth, M.; Yufa, N.; Hoffman, J.; Thomas, E. L. Triply Periodic Bicontinuous Cubic Microdomain Morphologies by Symmetries. *Macromolecules* **2001**, *34*, 6083.

68. Winkler, J. D.; Deshayes, K.; Shao, B. Photodynamic Transport of Metal Ions. *J. Am. Chem. Soc.* **1989**, *111*, 769–770.

69. J. D. Winkler, K. Deshayes, B. Shao, *J. Am. Chem. Soc.* **1989**, *111*, 769-770.

70. Görner, H.; Chibisov, A. K. Complexes of spiropyran-derived merocyanines with metal ions: Thermally activated and light-induced processes. *J. Chem. Soc., Faraday Trans.* **1998**, *94*, 2557–2564.

71. Suzuki, T.; Kato, T.; Shinozaki, H. Photo-reversible Pb^{2+}-complexation of thermoselective poly(*N*-isopropyl acrylamide-*co*-spiropyran acrylate) in water. *Chem. Commun.* **2004**, 2036–2037.

72. Radu, A.; Byrne, R.; Alhashimy, N.; Fusaro, M.; Scarmagnani, S.; Diamond, D. Spiropyran-based reversible, light-modulated sensing with reduced photofatigue. *J. Photochem. Photobiol. A* **2009**, *206*, 109.

73. Ipe, B. I.; Mahima, S.; Thomas, K. G. Light-Induced Modulation of Self-Assembly on Spiropyran-Capped Gold Nanoparticles: A Potential System for the Controlled Release of Amino Acid Derivatives. *J. Am. Chem. Soc.* **2003**, *125*, 7174– 7175.

74. Berkovic, G.; Krongauz, V.; Weiss, V. Spiropyrans and Spirooxazines for Memories and Switches. *Chem. Rev.* **200**, *100*, 1741–1753.

75. Imran, O. Q.; Kim, N. K.; Bodkin, L. N.; Dwulet, G. E.; Feng, X.; Kawabata, K.; Elimelech, M.; Gin, D. L.; Osuji, C. O. Nanoscale Thickness Control of Nanoporous Films Derived from Directionally Photopolymerized Mesophases. *Adv. Mater. Interfaces* **2020**, *8*, 2001977.
76. Wu, C.-H.; Meng, W.; Yoshio, M. Low-Voltage-Driven Actuators Using Photo-Cross-Linked Ionic Columnar Liquid-Crystalline Polymer Films. *ACS Mater. Lett.* **2022**, *4*, 153–158.